Measurement of the B_c Meson Lifetime with the Collider Detector at Fermilab

Masato AOKI

February 2006

Measurement of the B_c Meson Lifetime with the Collider Detector at Fermilab

Masato AOKI

(Doctoral Program in Physics)

Submitted to the Graduate School of
Pure and Applied Sciences
in Partial Fulfillment of the Requirements
for the Degree of Doctor of Philosophy in
Science

at the

University of Tsukuba

Abstract

The B_c^+ meson is the only meson containing two differently flavored heavy quarks, a bottom anti-quark and a charm quark. It was first observed in 1998 using 110 pb^{-1} of data collected at the Collider Detector at Fermilab (CDF) during Tevatron Run-I, in the semileptonic decay mode, $B_c^+ \to J/\psi \ell^+ \nu$, where $\ell^+ = e^+$ or μ^+, followed by $J/\psi \to \mu^+\mu^-$. With 360 pb^{-1} of $J/\psi \to \mu^+\mu^-$ triggered data collected by the CDF during Run-II (2001$\sim$), we measure the production cross section and the lifetime of the B_c^+ meson using $B_c^+ \to J/\psi e^+ \nu_e$ channel. The B_c^+ candidates are reconstructed from J/ψ-electron pairs with a displaced vertex and in the invariant mass range of $4 < M_{J/\psi e} < 6$ GeV/c^2. Background contributions from fake electrons, electrons from photon conversion and $b\bar{b}$ contamination are estimated using hadron tracks and conversion electron tracks in real data with help of Monte Carlo simulations. The production cross section times branching fraction for $B_c^+ \to J/\psi e^+ \nu_e$ relative to that for $B^+ \to J/\psi K^+$ in the kinematic range of $p_{T_B} > 4$ GeV/c and rapidity $\mid y_B \mid< 1$ is found to be

$$\frac{\sigma(B_c^+) \cdot \mathcal{B}(B_c^+ \to J/\psi e^+ \nu_e)}{\sigma_(B^+) \cdot \mathcal{B}(B^+ \to J/\psi K^+)} = 0.282 \pm 0.038 \pm 0.035 \pm 0.065,$$

where the first uncertainty is statistical, the second uncertainty is systematic from the B_c^+ yield and the third uncertainty is systematic in the acceptance calculation. The B_c^+ meson lifetime is measured as

$$\tau_{B_c} = 0.474 \ ^{+0.073}_{-0.066} \pm 0.033 \text{ ps},$$

where the first uncertainty is statistical and the second is systematic.

Acknowledgments

I want to thank everybody who was around me for the last few years for a constant support and help. This thesis could not have been completed without the support and encouragement of countless people.

I would like to thank my adviser Prof. Shinhong Kim for his guidance and supports throughout my graduate years. He gave me the opportunity to join the CDF collaboration and the support in working on CDF. I am so grateful for his careful reading of the text and his many criticisms to the point.

I wish to express my deepest appreciation for Ting Miao with his invaluable supports and encouragements. I learned a great deal from his precise way of thinking. I could not have finished this thesis without his great helps. I also want to thank Ilsung Cho who worked on this analysis together with me. He gave me a lot of helps.

Many thanks go to the CDF B group people, Matthew Herndon, Stefano Giagu, Christoph Paus, Marjorie Shapiro, Kevin Pitts, Steve Nahn, Dmitri Litvinsev, Cheng-Ju Lin, Tom LeCompte, Masashi Tanaka, Ilya Kravchenko, Vaia Papadimitriou who frequently gave me useful advices and opinions about the analysis.

I would like to thank all members of the Run-IIb Silicon group and all members of the Secondary Vertex Trigger (SVT) upgrade group.

I would like to thank staffs of my home institution. I would like to appreciate Prof. Koji Takikawa, Prof. Fumihiko Ukegawa, Dr. Kazuhiko Hara, Dr. Takasumi Maruyama, Dr. Yuji Takeuchi, Dr. Hiroyuki Matsunaga, Dr. Tomonobu Tomura for giving me so many advices.

I want to express my great appreciation to Carol Picciolo, Kyoko Kunori and Kazuko Kumashiro for their help through their secretary works.

I thank the Fermilab staffs and the technical staffs of the participating institutions for their vital contributions. I thank many CDF collaborators who have developed the detector and other analysis environment.

Most of all, I want to thank my parents and my brothers for their constant supports and encouragements. My grandfather was looking forward to my graduation and I was also doing my best to meet his expectations, but, unfortunately he passed away during my staying at Fermilab. I would like to dedicate this thesis to my grandfather.

This work was supported by the U.S. Department of Energy and National Science Foundation; the Italian Istituto Nazionale di Fisica Nucleare; the Ministry of Education, Culture, Sports, Science and Technology of Japan; the Natural Sciences and Engineering Research Council of Canada; the National Science Council of the Republic of China, the Swiss National Science Foundation; the A.P. Sloan Foundation; the Bundesministerium für Bildung und Forschung, Germany; the Korean Science and Engineering Foundation and the Korean Research Foundation; the Particle Physics and Astronomy Research Council and the Royal Society, UK; the Russian Foundation for Basic Research; the Comision Interministerial de Ciencia y Tecnologia, Spain; and in part by the European Community's Human Potential Programme under contract HPRN-CT-20002, Probe for New Physics.

Contents

List of Figures

List of Tables

Chapter 1

Introduction

Particle physics is the study of the fundamental constituents of the universe, the basic building blocks of everything we experience in the world around us. This field of study is also referred to as high-energy physics because these fundamental constituents of matter only become manifest by studying interactions at energy scales much higher than those that define our everyday experience. To create these high-energy environments, particle physicists rely on huge particle accelerators that take the ordinary and easily accessible subatomic particles, namely protons and electrons, accelerate them nearly to the speed of light, and bring them into collision.

This course of accelerator-based experiments coupled with observations from other sources like cosmic ray physics has produced the following picture of what makes up our universe (or at least, the portion of our universe with which we're most familiar). Every matter seems to be composed of bound states of structureless, point-like, half-integer spin particles known as fermions. These fermions come in two types, leptons and quarks, depending on the interactions they experience, as discussed below. The fermions are also organized into three groups, or *generations*, of particles. Each generation contains a pair of leptons and a pair of quarks, where the individual elements of the pair differ in charge by one unit. The electron with charge $-e$ and neutral neutrino make up the first generation of leptons, while the first generation of quarks is composed of the "up" quark with charge $+2/3e$ and the "down" quark with charge $-1/3e$. (The symbol e is defined to be a unit of charge equivalent in magnitude to the charge of an electron or approximately 1.602×10^{-19} C.) The other two generations contain essentially heavier copies of the particles in the first generation. Table 1.1 lists some of the characteristics the twelve fundamental fermions that make up matter. In addition, it should be noted that for each particle in Table 1.1, there is a corresponding antiparticle, identical to the particle in every respect except with opposite charge and other quantum numbers. For example the antiparticle partner of the electron is the positron, which has the same mass as the electron but is charge

$+e$.

In addition to revealing the spectrum of fundamental fermions that compose matter, high-energy physics experiments have also enabled us to classify all interactions between matter in terms of four fundamental forces known as the gravitational, electromagnetic, weak, and strong force. Each of these forces is mediated by the exchange of one or more types of integral-spin bosons between quarks and leptons. The mediator of the electromagnetic force is the familiar massless photon. A trio of massive gauge bosons known as W^+, W^-, and Z^0 mediate the weak force, while the exchange of eight massless gluons is responsible for the strong force. However, not all particles participate in the strong force, allowing a distinction between quarks, which couple to gluon, and leptons, which do not. Although not confirmed yet by experiment, it is believed that the carrier of the gravitational force is the massless, spin-2 graviton. Table 1.2 lists some properties of the four fundamental forces. Arguably, the greatest accomplishment to date in high-energy physics has been the creation of a general theoretical framework to describe the strong, weak, and electromagnetic interactions among quarks and leptons. This framework is known as the Standard Model, and together with the calculation technique of perturbation theory, it dominates most of the ongoing research in particle physics.

	Leptons			Quarks		
Generation	Flavor	Mass	Charge	Flavor	Mass	Charge
1st	ν_e	< 3 eV/c^2	0	u	$1.5 \sim 4$ MeV/c^2	$+2/3e$
	e	0.511 MeV/c^2	$-e$	d	$4 \sim 8$ MeV/c^2	$-1/3e$
2nd	ν_μ	< 0.19 MeV/c^2	0	c	$1.15 \sim 1.35$ GeV/c^2	$+2/3e$
	μ	105.7 MeV/c^2	$-e$	s	$80 \sim 130$ MeV/c^2	$-1/3e$
3rd	ν_τ	< 18.2 MeV/c^2	0	t	174 GeV/c^2	$+2/3e$
	τ	1.777 GeV/c^2	$-e$	d	$4.1 \sim 4.9$ GeV/c^2	$-1/3e$

Table 1.1: The fundamental fermions that make up matter. For each particle listed in this table, there is also an antiparticle with opposite quantum numbers, like charge.

Force	Boson	Boson Mass	Fermions Affected
Gravitational	Graviton	0	Quarks and leptons
Electromagnetic	Photon (γ)	0	Quarks and leptons
Weak	W^+, W^-,	80.4 GeV/c^2,	Quarks and leptons
	Z^0	91.2 GeV/c^2	Quarks and leptons
Strong	Gluon (g)	0	Quarks

Table 1.2: The four fundamental forces.

1.1 Standard Model

The Standard Model uses quantum field theory, which combines quantum mechanics and special relativity, to describe the dynamics of the fundamental fermions and their interactions under the strong, weak and electromagnetic forces. Each kind of quark and lepton is described by a separate, four-component Dirac spinor field, and the dynamics of the particles are encapsulated in a Lagrangian containing terms involving the fermion fields and their derivatives [1]. Symmetries observed in nature are imposed on the Standard Model Lagrangian to constrain its form. For example, relativity requires the Lagrangian to be Lorentz invariant. A particularly powerful set of symmetries for dictating the form of the Standard Model Lagrangian are local gauge symmetries. A gauge transformation is a continuous transformation applied to the fields in a quantum field theory. It is usually characterized according to the symmetry groups, such as U(1) or SO(10), from group theory. The gauge symmetry is considered local if a different transformation can be applied at every point in space without ruining the symmetry. However, to keep the Lagrangian invariant under local gauge transformations, it is necessary to introduce additional integral-spin fields, known as gauge fields, that also obey certain transformation laws and couple to the fermion fields. If the correct gauge symmetries are imposed on the Lagrangian, the necessary fields introduced can be identified with the fundamental forces of the Standard Model [2]. For this reason, the bosons that mediate the different fundamental interactions are often referred to as *gauge bosons*. For example, requiring the Lagrangian to be invariant under U(1) phase shifts of the fermion fields necessitates the introduction of a vector field A_μ that couples to the charged fermions. Working through the consequences of the local U(1) gauge invariance allows one to identify the vector field with the massless photon, the gauge boson of electromagnetism, and yields quantum electrodynamics(QED), the theory of relativistic charge particles interacting electromagnetically [3].

The full gauge structure of the modern-day Standard Model is said to be $\mathrm{SU(3)_{color}} \otimes \mathrm{SU(2)_L} \otimes \mathrm{U(1)_Y}$ [4]. The $\mathrm{SU(2)_L} \otimes \mathrm{U(1)_Y}$ component of the Standard Model gauge symmetry generates a unified version of the weak and electromagnetic interactions, known as electroweak theory [5]. Under this theory, negative helicity or left-handed particles are grouped into SU(2) doublets of weak isospin, as shown in Table 1.3, while positive helicity or right-handed particles are left as singlets. In addition, the theory has a symmetry under U(1) hyper-charge transformations, where hyper-charge is defined as a linear combination of electric charge and the third component of the weak isospin, $Y = I_3 + Q$. Taken by itself, the $\mathrm{SU(2)_L} \otimes \mathrm{U(1)_Y}$ gauge structure produces four massless gauge bosons, three for the $\mathrm{SU(2)_L}$ component of the gauge symmetry and one for the $\mathrm{U(1)_Y}$ part. This does not match with experimental observation of the electroweak interaction which involves three massive bosons(W^+, W^-, and Z^0) and one massless one(γ). In addition, the $\mathrm{SU(2)_L}$ symmetry would be spoiled by mass terms for the quarks and leptons. However, both deficiencies in this theory may be remedied by the introduction of an SU(2) doublet of scalar fields, known as the Higgs field, that couple to both the massless $\mathrm{SU(2)_L} \otimes \mathrm{U(1)_Y}$ gauge bosons

	Left-Handed Helicity	Right-Handed Helicity
Leptons	$\begin{pmatrix} \nu_e \\ e^- \end{pmatrix}, \begin{pmatrix} \nu_\mu \\ \mu^- \end{pmatrix}, \begin{pmatrix} \nu_\tau \\ \tau^- \end{pmatrix}$	ν_e, e, ν_μ, μ, ν_τ, τ
Quarks	$\begin{pmatrix} u \\ d \end{pmatrix}, \begin{pmatrix} c \\ s \end{pmatrix}, \begin{pmatrix} t \\ b \end{pmatrix}$	u, d, c, s, t, b

Table 1.3: The weak force groups fermions with left-handed helicity into SU(2) doublets of weak isospin, while right-handed particles form singlets under the weak SU(2).

as well as the massless quarks and leptons [6]. If the appropriate potential is chosen for the Higgs field in the Standard Model Lagrangian, it obtains a non-zero vacuum expectation value that spontaneously breaks the SU(2) symmetry. As a consequence, the massless $\mathrm{SU(2)_L \otimes U(1)_Y}$ gauge bosons obtain masses, although the linear combination of weak isospin and hyper-charge corresponding to the electric charge remains a massless state. Thus, with the addition of the Higgs field, the familiar one massless electromagnetic boson and three massive weak bosons emerge, as well as a new massive scalar Higgs boson. In addition, the terms generated by the coupling of the Higgs field to the quarks and leptons have the same structure as mass terms in the Lagrangian, allowing massive quarks and leptons to appear in the theory.

The $\mathrm{SU(2)_L \otimes U(1)_Y}$ gauge symmetry of the electroweak theory, coupled with the spontaneous symmetry breaking caused by the Higgs field leads to a rich phenomenology. As a consequence of the non-Abelian nature of the $\mathrm{SU(2)_L}$ symmetry, the electroweak gauge bosons couple to one another, unlike Abelian gauge theories, like QED, in which the photon has no self-coupling. In addition, because the weak interaction eigenstates are not identical to the mass eigenstates generated by the Higgs boson coupling, the weak interaction mixes the quarks and leptons from different generations, allowing interactions that covert quarks and leptons from one generation into quarks and leptons from a different generation. The matrix that describes this mixing is known as the Cabibbo-Kobayashi-Maskawa(CKM) matrix [7]. The CKM matrix can contain one complex phase and therefore allows for charge-parity violation in weak interactions, leading to such interesting phenomena as mixing among neutral K and B mesons and parity violating decay of K and B mesons [8]. Many of the features of the electroweak sector of the Standard Model, with the notable exception of the Higgs boson, have been supported and confirmed by experimental results [9], making it one of the most successful theories in all physics.

The remaining $\mathrm{SU(3)_{color}}$ gauge symmetry of the Standard Model is only relevant for quarks. Quarks are postulated to have an internal quantum degree of freedom labeled *color* consisting of three state: *red, blue* and *green.* All other fermions in the Standard Model are assumed to be colorless. The quantum field theory that results from requiring the Standard Model Lagrangian to be invariant under $\mathrm{SU(3)_{color}}$ transformations is known as quantum chromodynamics(QCD) [10]. In order to maintain invariance under local $\mathrm{SU(3)_{color}}$ transformations, it is necessary to introduce eight bi-colored massless gauge bosons, known as gluons. Because of the non-Abelian characteristic of the SU(3) gauge symmetry of QCD, these gluons interact with one another and hence carry color charge. Just as in electroweak theory, this non-Abelian self-coupling leads to a richer and more complex phenomenology than is exhibited by Abelian gauge theories such as QED.

That gluons can interact with one another leads to an interesting consequence for the strength of the QCD coupling constant, α_s. In quantum field theories, the coupling "constant" that determines the strength of a force's interaction is not really constant. Rather, the strength of the coupling constant changes as the energy, and hence the distance scale, of the interaction changes. For Abelian gauge fields like the electromagnetic field in QED, the coupling increases in strength for shorter distances(higher energies) and decreases at longer distances(lower energies). Qualitatively, this happens because virtual pairs of charged particles that are created and annihilated in the vacuum of the quantum field theory act like tiny dipoles, shielding the strength of charges at long distances, much like a charge is shielded in a dielectric material. A similar effect occurs in QCD except that in addition to virtual quark-antiquark pairs, there are also virtual gluon pairs. The effect of these gluon pairs is to cause the strength of the QCD coupling constant to increase for longer distances(lower energy) and decrease at shorter distances(higher energy). This behavior leads to two phenomenological features of QCD that make it quite different from other quantum field theories like QED: confinement and asymptotic freedom.

Confinement refers to the fact that quarks and gluons are never found as free particles. Another way to say this is that no free color charges exist. Instead, all quarks exist in either quark-antiquark bound states (known as mesons) or three-quark bound states (known as baryons). Collectively, meson and baryon bound states are referred to as hadrons. In mesons, the color of the quark is canceled out by the "anti-color" of the antiquark. For baryons, the equal mixture of colors from the three quarks adds up to give a "white" or "colorless" state. Another way to say this is that mesons and baryons must be in a color singlet state, much in the same way that two spin-1/2 particles can form a bound state of spin-0. This behavior is a consequence of the long distance (low energy) behavior of the QCD coupling constant. Consider a quark and an antiquark bound in a meson. Suppose we try to separate the quark from the antiquark. Because the strength of the strong force coupling grows with distance, the further we separate the quark from the antiquark, the greater the force of attraction between them becomes. To pull the quark free (in other words to separate it by an infinite distance from the antiquark) would require an infinite amount of energy. Before that point is reached, there will be enough energy stored in the color field to create a quark-antiquark pair from the vacuum. Thus, after separating the original quark from the antiquark, instead of having two free quarks, we are left with two mesons formed from the original quark and antiquark and the newly created quark-antiquark pair.

One consequence of confinement is that although QCD deals with interactions between quarks and gluons, experiments can only observe meson and baryon bound states. For example, in making calculations, a collision between a proton and an antiproton is treated as a QCD interaction between a quark or gluon from the proton and a quark or gluon from the antiproton. The result of this QCD interaction is typically a set of two or more quarks, gluons, or a mixture of the two. However, in the lab, because of confinement, one does not observe quarks and gluons directly. Instead, as described above, the quarks and gluons hadronize and "dress" themselves into mesons and baryons. However, in a high-energy collision, with the quarks and gluons moving at high velocity, a large number of quark-antiquark pairs can be created during the hadronization process. Thus, the final result of a $p\bar{p}$ collision is a large collection of mesons and baryons, grouped into collimated collections called jets. Usually there is one jet of hadrons per quark or gluon created in the underlying QCD process and their angular distribution reflects that of the underlying quarks and gluons in the QCD interaction. The process of a single quark or gluon generating a jet of particles in a high-energy collision is referred to as fragmentation.

On the other hand, *asymptotic freedom* refers to the behavior of QCD in the opposite regime of short distances (high energies). Just as the QCD coupling constant grows strong when long distances are involved, it becomes weaker at short distances. At short enough distance scales, the quarks behave mostly like free particles, with the interactions of QCD manifesting themselves as small effects. In this regime, QCD can be treated with perturbation theory, as described below. Experimentally, the region of asymptotic freedom in QCD can be explored by observing the results of collisions between hadrons for example, protons colliding with antiprotons at high energies. Such collisions can be viewed as high momentum transfer interactions between the quarks and gluons contained in the proton and antiproton. Of course, because of confinement, the end result of such a collision must be a collection of hadrons.

1.2 Heavy flavor as a test of perturbative QCD

The Lagrangian describing the Standard Model, in principle, provides all the information about the dynamics of quarks and leptons interacting through the strong, electromagnetic, and weak forces necessary to calculate such experimental observables as scattering cross sections and decay rates. However, in practice, making such calculations is less than straightforward. One of the most powerful and commonly used tools for extracting quantitative results from the Standard Model is known as perturbation theory. Perturbation theory is a standard calculation technique in which the answer to a complicated problem is approximated from the known answer to a similar, simpler problem by treating the complicated parts of the problem as a small perturbation on the exact solution. Perturbation theory is applied to the Standard Model by treating the gauge interactions among the particles as a small perturbation on the free non-interacting theory. High energy physics has honed the technique of applying perturbation theory to quantum field theories to a fine art through the use of a tool known as Feynman diagrams. Feynman diagrams are pictorial representations of various terms in the perturbation series used to make calculations of the quantum mechanical amplitudes for processes of interest. The basic elements of a Feynman diagram include lines to indicate the space-time trajectories of fermions and bosons involved in the process, and vertices at which three or more lines intersect to represent interactions included in the quantum field theory. Standard techniques exist for determining what kinds of lines and vertices are required to describe the physics contained in a quantum field theory Lagrangian. Once the lines and vertices have been specified, prescriptions known as Feynman rules can be developed that allow one to translate the diagram into a term in the perturbative expansion of the theory. In general, the order of the term in the perturbative expansion can be determined by counting the number of vertices present in the diagram: each vertex contributes a factor of the coupling constant, α, for the interaction, which is assumed to be small if perturbation theory is to be a valid approach. So, a Feynman diagram containing two vertices represents a second-order or $\mathrm{O}(\alpha)$ term in the perturbative series. The strength of this approach is that the dynamics of a particular field theory can be codified as a general set of Feynman rule based on the Lagrangian of the theory once, and from then on the Feynman rules and Feynman diagrams can be applied to solve a wide variety of problems. The Feynman rules associated with the Standard Model for QED, electroweak theory, and QCD have been known for quite some time now. Most modern computations of Standard Model processes begin with writing down all allowed Feynman diagrams that link the initial state of the problem to the final state, to the order in the perturbation series necessary to achieve the desired accuracy. Once the contributions to the amplitude from the various diagrams have been calculated, a cross section or decay rate can be obtained from the square of the amplitude integrated over the relevant phase space with the necessary phase space and flux factors included. The application of perturbation theory to electroweak theory has been very successful in producing quantitative results. This is a natural consequence of the small coupling constants of the electromagnetic and weak interactions, which allow good convergence of their perturbative series. The success of perturbation theory in electroweak physics can be seen in the stunning accuracy of such calculations as the anomalous magnetic moment of the electron [11]. However, the situation for QCD is very different. Because of the features of QCD described before, namely confinement and the running QCD coupling constant, the coupling constant of QCD is not small enough in low-energy interactions to warrant a perturbative treatment. However, because of asymptotic freedom, at high energy scales the coupling constant of QCD becomes small and perturbation theory becomes a viable option. Although techniques have been developed to deal with the low-energy strong coupling limit of QCD, for example, lattice QCD calculations [12], the most developed tool in the high-energy physics remains perturbation theory, making it interesting to study QCD in the regime where perturbative approximations apply.

The energy regime in which perturbative techniques are applicable to QCD is described by the parameter Λ_{QCD}, which is defined to be the energy scale at which the QCD coupling constant α_s becomes of order unity. Λ_{QCD} can be measured experimentally and has a value of approximately 200 MeV [9]. Processes occurring at an energy scale significantly above Λ_{QCD} can be handled by perturbative means. One useful example of such a process is the pair production of heavy quarks through QCD interactions at hadron colliders, like the Tevatron and LHC. Three quarks "charm, bottom, and top" are sufficiently massive that QCD interactions that pair-produce them are guaranteed to be in the perturbatively calculable regime. On the other hand, lighter quarks can be produced at scales where the perturbative approach fails, making perturbative calculations of light quark production more challenging.

Charm quarks, with a mass near 1.5 GeV/c^2 [9], are the most easily produced heavy flavor quarks at the Tevatron and LHC. However, there are a few theoretical and experimental difficulties that prevent them from being ideal tests of QCD in the perturbative regime. On the theoretical side, the charm quark mass, although greater than Λ_{QCD}, is also small enough that non-perturbative corrections could play an important role. In addition, charm quark signatures can be difficult to isolate from the vast background of light quark production.

Top quarks, on the other hand, do not suffer from any of the drawbacks that plague charm quark measurements. The top quark mass, approximately 175 GeV/c^2 [9], is so large that non-perturbative effects may be neglected to a good approximation when calculating its production. In addition, the top quark decays so quickly that it does not hadronize, meaning theoretical uncertainties associated with that non-perturbative process are also completely absent. In addition, the large mass and distinctive decays of top quarks make it relatively easy to isolate a reasonably pure sample of top quark events. However, the top quark mass also makes it difficult to produce and detect top quarks in sufficient quantity to perform high-statistics tests of perturbative QCD calculations. Nonetheless, present indications are that, within statistical precision, the measured top quark cross section agrees well with perturbative QCD calculations [9].

Intermediate in mass between charm and top, the bottom quark, with a mass of approximately 4.5 GeV/c^2 [9], is a good compromise for making high statistics checks of perturbative QCD calculations. The b quark mass is sufficiently higher than Λ_{QCD} that non-perturbative effects should not be a serious consideration. At hadron colliders like the Tevatron, b quarks are primarily pair-produced through QCD processes like $q\bar{q} \to b\bar{b}$ or $gg \to b\bar{b}$. It is also possible to create b quarks either in pairs or singly through electroweak processes; however, the rates for such production are negligibly small compared to QCD production due to the much large coupling constant of QCD. Given reasonable assumptions about the size of the b quark production cross section, one expects on the order of hundreds of b quarks to be produced every second at a collider like the Tevatron. In addition, the weak decays of bottom hadrons (denoted B hadrons) have two key features that can be exploited to define efficient experimental signatures of b quark production. One feature of B decays useful for defining a b quark data sample is the relatively high semileptonic branching fraction. Roughly 20% of B decays involve an electron or muon [9]. In detectors like CDF, high momentum electrons and muons provide clean signals around which efficient triggers can be defined. The second feature of B decays useful for defining clean b quark samples is the long B lifetime. B hadron decays, much like charm hadron decays, proceed through the emission of a virtual W boson. Because the W is so much more massive than b or c quarks, the lifetime of this decay is fairly long, as opposed to the weak decay of the top quark, which is massive enough that it can decay through the emission of a real W boson with essential zero lifetime. The B lifetime is further enhanced over charm lifetimes because the dominant CKM matrix element relevant for the flavor-changing, weak decay of a B hadron, $\mid V_{cb} \mid \approx 0.04$, while the CKM matrix element that dominates the weak decay of charm, $\mid V_{cs} \mid \approx 0.97$ [9]. Therefore, B hadrons decay with a lifetime of approximately 1.5 ps [9] and can travel on the order of millimeters in the detector with the relativistic boosts typical of detected B hadrons. This distance is sufficiently long that the precise tracking detectors employed at CDF are capable of resolving the separation of the decay point of the B hadron from the point at which the $p\bar{p}$ interaction occurred. In addition, the presence of a long-lived B hadron can be detected by reconstructing particle trajectories, or tracks, from the B decay that have large impact parameters with respect to the $p\bar{p}$ interaction vertex. Using these two standard techniques, it is possible to identify large, relatively low-background $b\bar{b}$ samples at hadron colliders like the Tevatron. Given the advantages of testing perturbative QCD calculations using measurements of $b\bar{b}$ production at the Tevatron, it came as quite a surprise to the high-energy physics community when measurements of the b quark cross section from both the CDF and DØ detectors at the Tevatron were consistently higher than next-to-leading-order (NLO) QCD perturbative calculations.

One approach for improving the agreement between the theoretical calculation and the data is to improve the theoretical description of b fragmentation. Fragmentation refers to the processes by which bare quarks produced in the QCD interaction evolve into collimated collections or jets of hadrons. Fragmentation is a non-perturbative process that must be described using phenomenological models. The most commonly used model for b quark production is due to Peterson *et al.*[13]; however, recent experimental evidence from e^+e^- colliders suggests that the Peterson model of fragmentation is not the best model available [14]. Cacciari and Nason have explored the effect of including an improved model of B fragmentation in comparing the theoretical calculation of the B^+ meson cross section to a particular measurement at CDF [15]. In addition to using an improved parameterization of the b fragmentation, they also account for logarithmic enhancements to the cross section coming from multiple soft gluon emissions. Their resulting calculation, which they call fixed-order, next-to-leading-log (FONLL), reduces the discrepancy between the data and theory. Based on this improvement, further explorations of B fragmentation seem a promising route for better understanding the discrepancy in b production.

There are two proposed resolutions to the b quark production mystery represent opposite ends of the spectrum of resolutions. The first solution involving improved models of fragmentation suggests that the discrepancy comes simply from our inability to model certain non-perturbative effects that are part of the standard picture of b production. On the other hand, the second explanation involves a fundamental modification to the Standard Model. This broad range of possible explanations for the b production mystery is what fuels much of the interest in this subject.

Another possibility for understanding the b quark excess involves higher-order terms in the perturbative calculation of b quark production that are needed to describe the data accurately. On the surface, such a suggestion seems unlikely because in a typical perturbative series, if perturbation theory can be applied successfully, the leading terms will closely approximate the exact answer, and additional terms provide incremental improvements. However, despite the claim that bottom quark production can be calculated using perturbative QCD, it is not the case that the leading-order terms accurately represent the data and that higher-orders simply provide small corrections. In fact, the leading-order calculation of the b cross section lies another factor of two to three below the NLO prediction, which is itself a factor of two to three below the measured cross section [19]. This unexpected feature of the perturbative b production calculation can be explained by realizing that starting at next-to-leading order, two new mechanisms for $b\bar{b}$ pairs produced in association with a light quark or gluon appear. At leading order, the only QCD production mechanism for $b\bar{b}$ pairs includes processes like quark-antiquark annihilation and gluon-gluon fusion that yield a single $b\bar{b}$ pair with no other quarks or gluons in the final state, as shown in Figure 1.1. However, at higher-orders, it is possible to produce a $b\bar{b}$ pair in addition to a light quark or gluon by adding a $g \to b\bar{b}$ splitting to a lower-order QCD process involving only light quarks and gluons, as shown in Figure 1.2. If the gluon splits to a virtual $b\bar{b}$ pair in the initial state and one of the b quarks is scattered into the final state by interaction with a quark or gluon from the other beam, the process is called flavor excitation. On the other hand, if the $g \to b\bar{b}$ splitting occurs in the final state, the process is called gluon splitting. In addition, the term flavor creation is used to refer to the lowest-order $b\bar{b}$ production process, as well as higher-order corrections to the leading-order diagrams, as shown in Figure 1.3. It turns out that the higher-order flavor excitation and gluon splitting processes can contribute at approximately the same level as the leading-order diagrams. One way to understand this is to realize that the cross section for $gg \to gg$ is of order one hundred times larger than the cross section for $gg \to b\bar{b}$. Therefore, even after accounting for the extra $\mathrm{O}(\alpha_s)$ suppression of flavor excitation and gluon splitting over the leading-order term, these higher order production mechanisms are still numerically significant.

The perturbative calculations referenced above are performed with next-to-leading-order (NLO) accuracy because this is the lowest order that yields sensible results for b production. However it may be possible that higher orders make non-negligible corrections to the theoretical predictions that might help reduce the discrepancy with data. So far, the very difficult next-to-next-to-leading-order (NNLO) calculation of b production has not been successfully performed. However, there is an approximation, known as the parton shower model, that is not

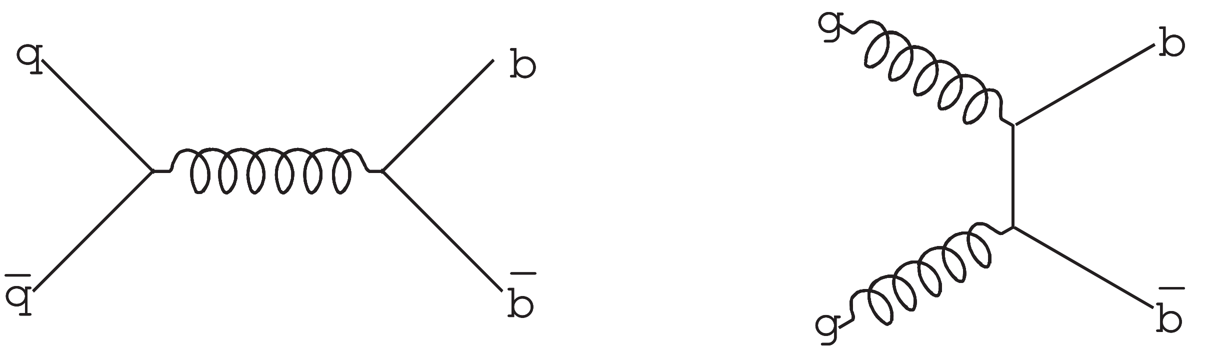

Figure 1.1: Leading-order Feynman diagrams for $b\bar{b}$ production.

exact to any particular order in perturbation theory, but captures the qualitative features of contributions from all orders. It is demonstrated in Ref. [16] that calculations using the parton shower approach are able to achieve reasonable agreement with measurements of the b quark cross section, suggesting that perhaps corrections from orders beyond NLO are significant. On the other hand, the parton shower approach neglects certain interferences between the various $b\bar{b}$ production mechanisms (flavor creation, flavor excitation, and gluon splitting), making it possible that the improved agreement between the parton shower calculation and the data is merely the result of overcounting. For this reason, it is interesting to further compare data and parton shower predictions to ascertain whether the contributions from higher-order processes predicted by the parton shower model seem supported by the data.

Figure 1.4 shows the b quark production cross section measured by CDF Run-II. This figure shows that the shape of the cross section distributions as a function of p_T is reasonably described by the theoretical calculation.

1.3 B Physics study at Hadron Collider

Hadron colliders as well as e^+e^- B-factories are good places to perform B physics. At a hadron collider, large numbers of b hadrons are produced due to a large integrated luminosity times cross section for b quark production. The production cross section is very large relative to that at e^+e^- experiments. The total cross section for $b\bar{b}$ production at the Tevatron is approximately 50 μb. This cross section in $p\bar{p}$ collisions can be compared to 1.1 nb cross section for an Υ(4S) decaying into B mesons in B-factories. At the Z^0 boson pole mass energy, the cross section for b quark production is 6.7 nb.

There are advantages and disadvantages of e^+e^- B-factories. The primary benefit is sitting at the Υ(4S), which provides a known initial state in terms of its mass and quantum numbers. In addition, the Υ(4S) decays into $B\bar{B}$ mesons with a branching ratio of nearly 100%. Finally,

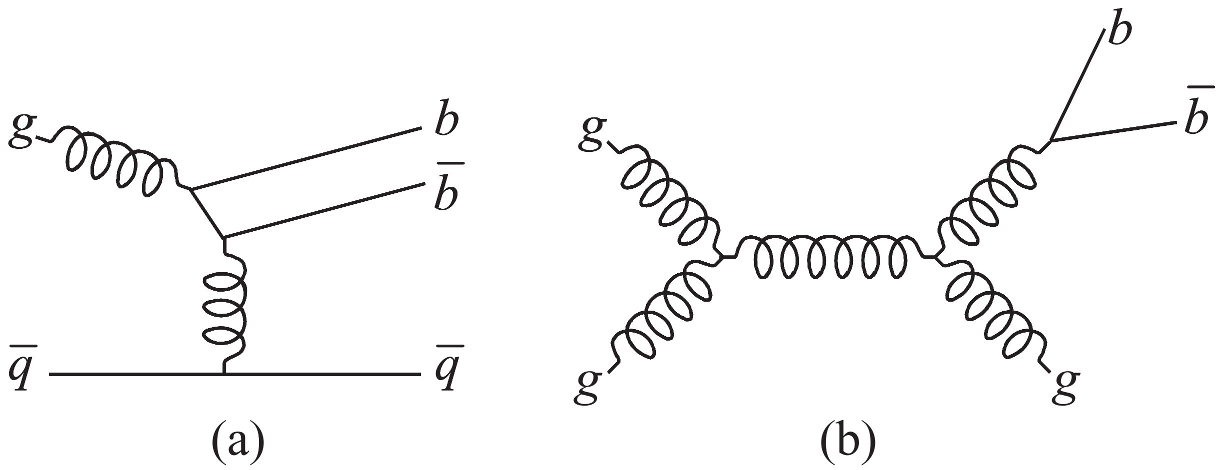

Figure 1.2: Higher-order $b\bar{b}$ created by adding a $g \to b\bar{b}$ splitting to a leading-order process containing only light quarks and gluons. The new production mechanisms are classified as to whether the $g \to b\bar{b}$ splitting occurs in the initial state, with one of the b quarks from the splitting scattering against a quark or gluon from the other beam ((a) : flavor excitation), or whether the $g \to b\bar{b}$ occurs in the final state ((b) : gluon splitting).

the ratio of the cross section for $b\bar{b}$ to the total cross section (which includes the continuum e^+e^- spectrum) is approximately 1:3, which is quite large. However, because the B mesons are produced from a $J^{PC} = 1^{--}$ state, the resultant B mesons are restricted in terms of what states are allowed. The b hadrons have very little momentum since the decay is very near at the threshold. Thus, direct measurements of a particular B meson lifetime cannot be easily made (This problem has been conquested by employing un-equal e^+ and e^- energies so that produced Υ(4S) has finite boost.). Also, only B^+ and B^0 mesons are able to be produced since these decays are below the threshold, and the production of more massive B hadrons like B_s^0, B_c^+, Λ_b is not possible. At e^+e^- collider with much higher energy like LEP, the initial state is also known and $\sigma_{b\bar{b}}/\sigma_{\text{total}}$ is rather large, 15%. The b hadrons are boosted as the Z^0 mass is much larger than any B hadron mass. At LEP, production of all species of b hadrons is theoretically possible. The main disadvantage is the relatively low b production cross section which must be combined with the low branching ratio($\sim 10^{-4}$) for exclusive b hadron decays. Thus, LEP recorded roughly 100 fully reconstructed b hadron decays in a year.

The hadron collider also has advantages and disadvantages. While the cross section for $b\bar{b}$ is large compared to that at e^+e^- experiments, the cross section is small compared with the total cross section in $p\bar{p}$ collisions: $\sigma_{b\bar{b}}/\sigma_{\text{total}} \sim 6 \times 10^{-4}$. The challenge of performing B physics at a hadron collider is to efficiently trigger on events with a high B content. Practically this is accomplished by triggering on high-p_T leptons arising from the semileptonic decay of the B hadron, or by triggering on dimuons from $J/\psi \to \mu^+\mu^-$ decays. Backgrounds of very high-p_T

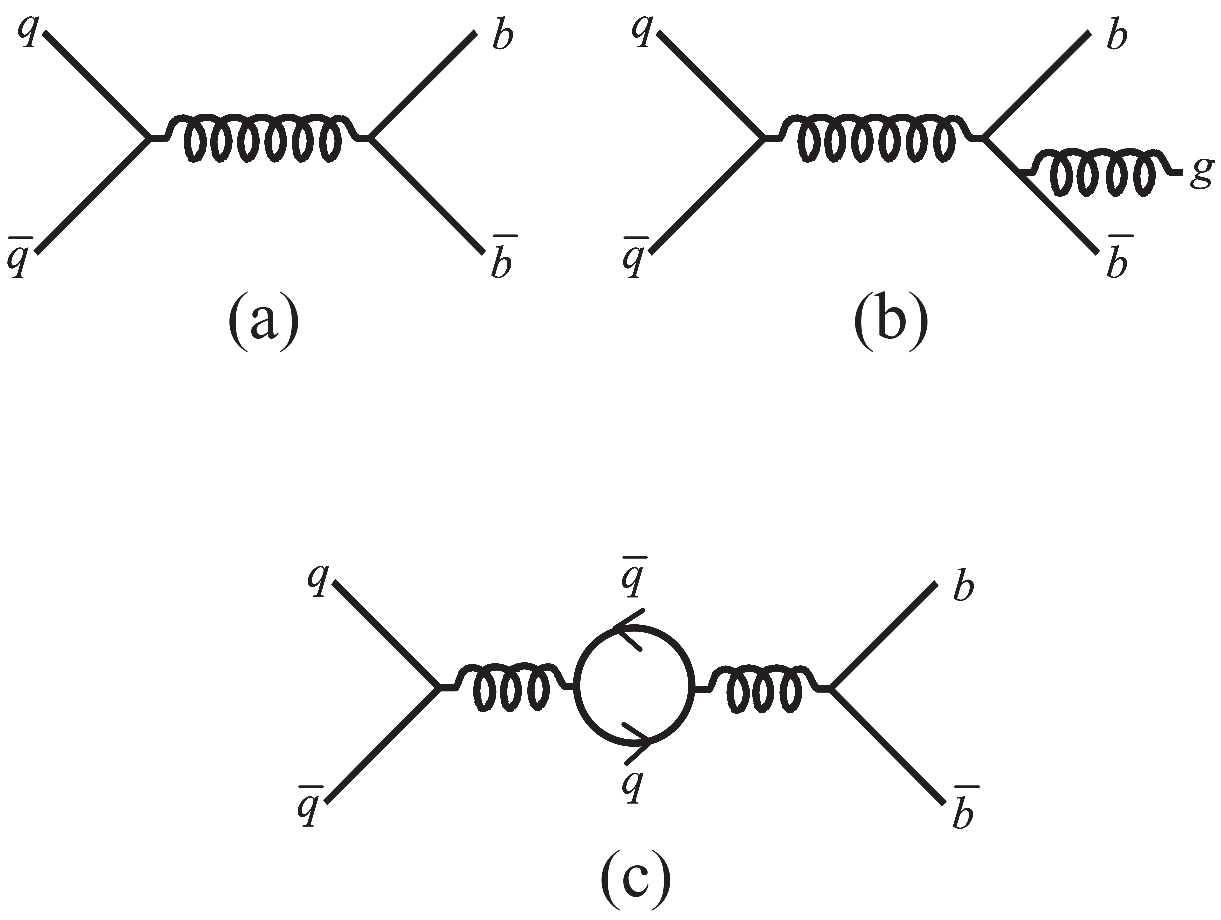

Figure 1.3: Diagrams contributing to flavor creation. (a):Leading-order, (b):Radiative corrections, (c):Higher-order loop diagrams (interfere with leading-order diagrams).

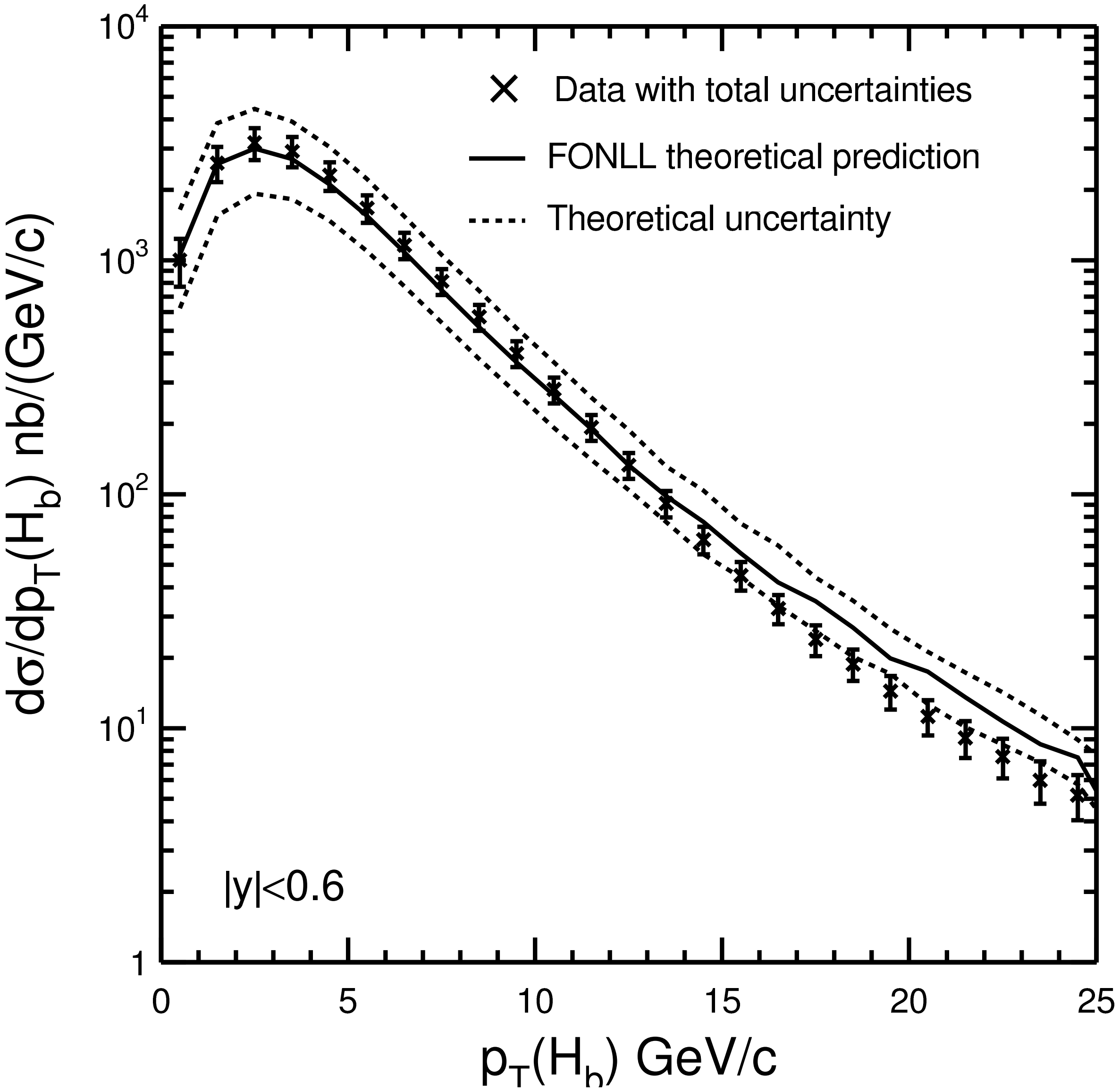

Figure 1.4: Differential cross-section distribution of b-hadron production as a function of b-hadron transverse momentum measured by CDF Run-II [17]. The crosses with error bars are the data with systematic and statistical uncertainties added, including correlated uncertainties. The solid line is the central theoretical value using the FONLL calculations outlined in [18], the dashed line is the theoretical uncertainty.

leptons from $W^\pm$ and Z^0 decays are easily removed. Backgrounds of lower-p_T come mainly from semileptonic decays of charmed hadrons, photon conversions, decays-in-flight, and other fakes such as hadronic punch through, which are more difficult to remove. Nevertheless, semileptonic decays are a subject of B physics studies in hadron colliders. Measurements of the production cross section, mixing, and lifetimes are possible. However, since the neutrino from semileptonic decays is not identifiable, full reconstruction of b hadrons is not possible.

By triggering on dimuons from J/ψ decays, one is able to obtain a sample of events which is enriched in reconstructible B hadrons. b hadrons decay into J/ψ particles with a branching ratio of $\sim$1.16% [9]. Many of these decays involve only a couple of additional charged tracks which can be combined with the J/ψ for complete reconstruction.

1.4 The B_c^+ meson

The presence of the small parameter $\Lambda_{\rm QCD}/m_Q$, where $\Lambda_{\rm QCD}$ is the scale of the quark confinement and m_Q is the heavy quark mass, has allowed one to develop the powerful tools for the study of the QCD dynamics in the heavy quark interactions, such methods as the phenomenological potential models (PM) [19], the QCD sum rules (SR) [20] and Effective Heavy Quark Theory (EHQT) [21], that is successfully applied for the study of hadrons, containing a single heavy quark. Thus, the investigation of the processes with the heavy quarks allows one to extract and study non-perturbative QCD effects, causing the quark hadronization, by means of the use of the heavy quark as the "marked atoms". A successful realization of such program of studies becomes possible due to the progress in the experimental technique of detecting and identifying those particles (mainly, it is related with the invention and the improvement of the vertex detectors, allowing one to observe the heavy quark particles due to its running gap from the primary vertex of the interaction).

The ground state of $(c\bar{b})$ system, B_c^+ meson, was first observed by the CDF collaboration [22]. They observed approximately 20 B_c^+ events in the $B_c^+ \to J/\psi\ell^+\nu$ decay mode and demonstrated the possibility of the experimental study of the B_c^+ meson. (Charge conjugate modes are implied throughout this thesis unless otherwise specified.)

Among the heavy quarkonia $(Q\bar{Q}')$, the $(c\bar{b})$ system with the open charm and beauty takes a particular place. In contrast to the hidden charm $(c\bar{c})$ and beauty $(b\bar{b})$ families, studied in details experimentally [9] and being quite accurately described theoretically, the family of B_c^+ mesons has some specific production and decay mechanisms and the spectroscopy, whose study allows one to extend and to enforce the quantitative understanding of the QCD dynamic as well as to step forward in the study of the most important parameters of the electroweak theory.

From the spectroscopy viewpoint, the $(c\bar{b})$ system is the heavy quarkonium, whose spectrum can be quite reliably calculated in the framework of the QCD-motivated non-relativistic potential models as well as in the QCD sum rules. $(c\bar{b})$ system is the only system, composed of two heavy quarks, where the description of this system mass spectrum can test the self-consistency for the potential models and the QCD sum rules, whose parameters (the quark masses, for instance) have been fixed from the fitting of the spectroscopic data on the charmonium and bottomonium. Thus, the study of the B_c^+ family spectroscopy can serve for the essential improvement of the quantitative characteristics of the quark models and the QCD sum rules, which are intensively applied in other fields of the heavy quark physics (for example, when one extracts values of elements in the matrix of mixings of the heavy quark weak charged currents and when one estimates contributions, interfering with the effects of the CP invariance violation, in the heavy hadron decays).

Moreover, there is a problem of the precise description of the P-wave level splittings in the charmonium and bottomonium, when the experimental measurement has found an essential deviation from the values, which have been expected in some well-acknowledged quark models. The study of the B_c^+ meson family can help in a solution of this problem.

In addition, the $(c\bar{b})$ system is interesting due to that it allows one, in a new way, to use the phenomenological information, obtained from the detailed experimental study of the charmonium and bottomonium. So, for example, $(c\bar{b})$ takes an intermediate place between the charmonium and bottomonium in respect to both the system level masses and the values of averaged distances between the heavy quarks. As has been clarified, in the region of the average distances in the $(c\bar{c})$ and $(b\bar{b})$ systems, the heavy quark potential possesses the simple scaling properties, which states that the kinetic energy of the heavy quarks is practically a constant value, independent of the quark flavors and the excitation level in the heavy quarkonium system. Furthermore, this leads to that the heavy quarkonium level density does not depend on the flavors of quarks, composing the heavy quarkonium. This regularity is quite accurately valid empirically for the $(c\bar{c})$ and $(b\bar{b})$ systems and it can be used in the framework of the QCD sum rules, where a scaling relation, connecting the leptonic constants of the S-wave levels in the different quarkonia, is derived.

Further, having no strong and electromagnetic annihilation channels of decays, the excited $(c\bar{b})$ system levels, being below the threshold of the decay into the BD meson pair, will decay into the lightest basic pseudo-scalar state $B_c^+(J^P = 0^-)$ due to the radiative cascade transitions into the underlying levels. Therefore, the widths of the electromagnetic (γ) and hadronic ($\pi\pi$, η, ...) radiative decays of the given excitation into the other levels will compose its total width. As a result, the total widths of the excited levels in the $(c\bar{b})$ system turn out two orders of magnitude less than the total widths of the charmonium and bottomonium excited levels, for which the annihilation channels are essential. Moreover, maybe, the data on the radiative hadronic decays in the $(c\bar{b})$ family give a possibility for one to solve some problems on the theory of the hadronic transitions in the heavy quarkonia (for example, the problem on the anomalous distribution over the $\pi\pi$ pair invariant mass in the decay of $\Upsilon'' \to \Upsilon\pi\pi$ [23, 24]).

Thus, on the one hand, the methods, applied in the heavy quark physics, are able quite reliably to point out the spectroscopic characteristics of the $(c\bar{b})$ system for one to make a purposefully-directed experimental search of the given heavy quarkonium, and, on the other hand, the measurement of the spectroscopic data in the B_c^+ family would allow one to improve these methods, approaches for the extraction of the fundamental parameters of the Standard Model from both the B_c^+ meson physics and the other fields of the heavy quark physics.

Like the other mesons with the open flavor, the basic state of the B_c^+ meson family, the pseudo-scalar meson $B_c^+(0^-)$, is the long-living particle, decaying due to the weak interaction and having the lifetime, comparable with the lifetimes of B and D mesons, so this feature essentially distinguishes B_c^+ from the heavy quarkonia η_c and η_b. Therefore, the study of B_c^+ meson decays is the rich field of the heavy quark physics, where one extracts an important information about both the QCD dynamics and the weak interactions. The spectroscopic B_c^+ meson characteristics such as the leptonic constant, determining the width of the wave package of the $(c\bar{b})$ system in the basic state, essentially determine the description of the B_c^+ decay modes, in which some specific features and effects are observed.

First of all, the presence of the valence heavy quark-spectator leads to a large probability for the B_c^+ decay modes with the heavy mesons in the final state, i.e. in the decays $B_c^+ \to \psi(\eta_c)$ and $B_c^+ \to B_s^{(*)}$. The large ψ particle yield is interesting, in addition, by that the ψ particle has the perfect experimental signature in the leptonic decay mode.

Further, in the consideration of the semileptonic $B_c^+ \to \psi(\eta_c)\ell^+\nu$ decays, the non-relativistic heavy quark motion inside the quarkonia leads to an essential effect, caused by large Coulomb-like corrections, which notably change the calculation results for these decays in the framework of the QCD sum rules. Only the taking into the account these corrections makes the results of the QCD sum rules and the potential quark models to be consistent.

Note first of all, that the necessity of the two pair production of heavy quarks in the electromagnetic and strong processes for the B_c^+ yield leads to that the leading order of the perturbative QCD has an additional factor of the suppression $\sim \alpha_s^2$ in respect to the leading order of the perturbation theory for the production of the single flavor heavy quarks, for example, the $b\bar{b}$ pair, so $\sigma(B_c^+)/\sigma(b\bar{b}) \sim \alpha_s^2 \mid \Psi(0) \mid^2 /m_c^3$. This causes the low yield of the B_c^+ mesons in respect to the B meson production.

The analysis of the leading approximation in the perturbative QCD for the B_c^+ meson production allows one to derive a number of analytical expressions for the B_c^+ production cross section, where one has especially to stress the expressions for the functions of the heavy quark fragmentation into the heavy quarkonium in the scaling limit $M^2/s \to 0$, so these functions are determined by the values of α_s, the quark masses and the leptonic constant of the meson. Thus, the fragmentational B_c^+ production can be reliably described by the analytical expressions, so this opens new possibilities in the study of the QCD dynamics, essential in the complete picture of the heavy quark physics.

1.4.1 The mass spectrum of the $(c\bar{b})$ family

The B_c^+ and other $c\bar{b}$ system mass can be calculated using the framework of the phenomenological potential models for non-relativistic heavy quarks. The masses of the charmonium and the bottomonium systems have been studied experimentally in detail and are described quite accurately in the framework of the potential models. To describe the B_c^+ system, it would be advantageous to use the potentials whose parameters do not depend on the flavor of the constituent quarks of the system. This could be done by using a model which describes both the charmonium and the bottomonium systems accurately. This will not require the interpolation of the parameters of the model, which are obtained experimentally from the charmonium and the bottomonium systems to an intermediate region of the B_c^+ system.

In Ref. [25], the mass spectrum of the $c\bar{b}$ family is estimated by using the relativized quark model. In this model, mesons are approximated by the $q\bar{q}$ sector of Fock space, in effect integrating out the degrees of freedom below some distance scale, μ^{-1}. This results in an effective potential, $V(\vec{p},\vec{r})$, whose dynamics are governed by a Lorentz vector one-gluon-exchange interaction at short distance and a Lorentz scalar linear confining interaction. The basic equation of the model is the rest frame Schrödinger-type equation:

$$H|\psi\rangle = [H_0 + V_{q\bar{q}}(\vec{p},\vec{r})]|\psi\rangle = E|\psi\rangle, \tag{1.1}$$

where

$$H_0 = \sqrt{p^2 + m_q^2} + \sqrt{p^2 + m_{\bar{q}}^2}. \tag{1.2}$$

The effective quark-antiquark potential, $V_{q\bar{q}}(\vec{p},\vec{r})$, was found by equating the scattering amplitude of free quarks, using a scattering kernel with the desired Dirac structure, with the effects between bound quarks inside a hadron [26, 27]. Due to relativistic effects the potential is momentum dependent in addition to being co-ordinate dependent. To first order in $(v/c)^2$, $V_{q\bar{q}}(\vec{p},\vec{r})$ reduces to the standard non-relativistic result:

$$V_{q\bar{q}}(\vec{p},\vec{r}) \to V(\vec{r}) = H_{q\bar{q}}^{\mathrm{conf}} + H_{q\bar{q}}^{\mathrm{cont}} + H_{q\bar{q}}^{\mathrm{ten}} + H_{q\bar{q}}^{\mathrm{s.o.}}, \tag{1.3}$$

where

$$H_{q\bar{q}}^{\mathrm{conf}} = C + br - \frac{4}{3}\frac{\alpha_s(r)}{r} \tag{1.4}$$

includes the spin-independent linear confinement and Coulomb-like interaction,

$$H_{q\bar{q}}^{\mathrm{cont}} = \frac{32\pi}{9}\frac{\alpha_s(r)}{m_q m_{\bar{q}}} \cdot \vec{S}_q \cdot \vec{S}_{\bar{q}} \delta^3(\vec{r}) \tag{1.5}$$

is the color contact interaction,

$$H_{q\bar{q}}^{\mathrm{ten}} = \frac{4}{3}\frac{\alpha_s(r)}{m_q m_{\bar{q}}}\frac{1}{r^3}\left[\frac{3\vec{S}_q \cdot \vec{r} \vec{S}_{\bar{q}} \cdot \vec{r}}{r^2} - \vec{S}_q \cdot \vec{S}_{\bar{q}}\right] \tag{1.6}$$

is the color tensor interaction,

$$H_{q\bar{q}}^{\text{s.o.}} = H_{q\bar{q}}^{\text{s.o.(cm)}} + H_{q\bar{q}}^{\text{s.o.(tp)}} \tag{1.7}$$

is the spin-orbit interaction with

$$H_{q\bar{q}}^{\text{s.o.(cm)}} = \frac{4\alpha_s(r)}{3r^3}\left(\frac{\vec{S}_q}{m_q m_{\bar{q}}} + \frac{\vec{S}_q}{m_q m_{\bar{q}}} + \frac{\vec{S}_q}{m_q^2} + \frac{\vec{S}_{\bar{q}}}{m_{\bar{q}}^2}\right)\cdot\vec{L} \tag{1.8}$$

its color magnetic piece arising from one-gluon exchange and

$$H_{q\bar{q}}^{\text{s.o.(tp)}} = -\frac{1}{2r}\frac{\partial H_{q\bar{q}}^{\text{conf}}}{\partial r}\left(\frac{\vec{S}_q}{m_q^2} + \frac{\vec{S}_{\bar{q}}}{m_{\bar{q}}^2}\right)\cdot\vec{L} \tag{1.9}$$

the Thomas precession term. In these formulae $\alpha_s(r)$ is the running coupling constant of QCD.

To relativize the $q\bar{q}$ potential, the full Dirac scattering amplitude was used as a starting point which for on-shell $q\bar{q}$ scattering is exact. However for a strongly interacting system there will in general be off-shell behavior which was not considered in addition to other simplifications such as neglecting more complex components of Fock space. Therefore a semiquantitative model of relativistic effects was built by smearing the co-ordinate $\vec{r}$ over the distances of the order of the inverse quark mass by convoluting the potential with a Gaussian form factor and replacing factors of m_i^{-1} with, roughly speaking , factors of $(p^2+m_i^2)^{-1/2}$. The details of this relativization procedure and the method of solution can be found in reference [28]. It should be kept in mind that because coupled channel effects and the crudeness of the relativization procedure were neglected, the mass predictions are not expected to be accurate to better than $\sim 10-20$ MeV$/c^2$. For the case of a quark and antiquark of unequal mass charge conjugation parity is no longer a good quantum number so that states with different total spins but with the same total angular momentum, such as the ${}^3S_1 -{}^1P_1$ and ${}^3D_2 -{}^1D_2$ pairs, can mix via the spin orbit interaction or some other mechanism. Equation 1.8 and 1.9 can be rewritten to explicitly give the antisymmetric spin-orbit mixing term:

$$H_{\text{s.o.}}^{-} = +\frac{1}{4}\left(\frac{4}{3}\frac{\alpha_s}{r^3} - \frac{b}{r}\right)\left(\frac{1}{m_Q^2} - \frac{1}{m_{\bar{Q}}^2}\right)\vec{S}_-\cdot\vec{L}, \tag{1.10}$$

where $\vec{S}_- = \vec{S}_Q - \vec{S}_{\bar{Q}}$. Consequently, the physical $j=1$ P-wave states are linear combinations of ${}^3S_1$ and ${}^1P_1$:

$$\begin{aligned} P' &= {}^1P_1\cos\theta_{nP} + {}^3P_1\sin\theta_{nP} \\ P &= -{}^1P_1\sin\theta_{nP} + {}^3P_1\cos\theta_{nP} \end{aligned} \tag{1.11}$$

with analogous notation for the corresponding $L = D$, F, etc. pairs. In Equation 1.11, $P \equiv L = 1$ designates the relative angular momentum of the $Q\bar{Q}$ pair which is equal to L. This notation implicitly implies $L-S$ coupling between the quark spins and the relative orbital angular momentum. In the heavy quark limit in which the heavy quark mass $M_Q \to \infty$, the states can be described by the total angular momentum of the light quark, j which couples to the spin of the heavy quark and corresponds to $j-j$ coupling. This limit gives rise to two doublets, one with $j = 1/2$ and the other with $j = 3/2$ and corresponds to two physically independent mixing angle $\theta = -\tan^{-1}(\sqrt{2}) \simeq -54.7°$ and $\theta = \tan^{-1}(1/\sqrt{2}) \simeq 35.3°$ [29]. Since assuming $L-S$ eigenstates and then including LS mixing here, the notation of Equation 1.11 is used while some authors prefer to use the $j = j$ basis. It is straightforward to transform between the $L-S$ basis and the $j-j$ basis. It will turn out that radiative transitions are particularly sensitive to the ${}^3L_L -{}^1 L_L$ mixing angle with predictions from different models in some cases giving radically different results. Note that the definition of the mixing angles are fraught with ambiguities. For example, charge conjugating $c\bar{b}$ into $b\bar{c}$ flips the sign of the angle and the phase convention depends on the order of coupling $\vec{L}$, $\vec{S}_Q$ and $\vec{S}_{\bar{Q}}$ [29].

The Hamiltonian problem was solved using the following parameters: the slope of the linear confining potential is 0.18 GeV^2, $m_c = 1.628$ GeV$/c^2$, and $m_b = 4.977$ GeV$/c^2$. The predictions of this model are given in Figure 1.5 and are compared to the predictions of other calculations in Table 1.4. The experimental result of the B_c^+ mass measurement by the CDF Run-I [22], $6.40 \pm 0.39 \pm 0.13$ GeV$/c^2$, agrees with those predictions. Because the mixing angles defined in Equation 1.11 are important for predictions of radiative transitions those predictions are also given in Table 1.4. Although Table 1.4 has attempted to consistently give the masses and the mixing angles of the predicted eigenstates in the convention of Equation 1.11, because not all authors have unambiguously defined their phase conventions, Table 1.4 cannot guaranty that these results are free of inconsistencies.

The different models are in remarkable agreement with the differences, for the most part, within the expected accuracy of the models. This almost certainly indicates how the various models have converged using similar confining potentials and including a strong running coupling constant in the Coulomb piece of the potential. The only significant difference is the large spread (~ 70 MeV$/c^2$) for the $1D$ multiplet center of gravity predictions. The spin-dependent splittings are also in reasonable agreement. Potential models can therefore be used as a reliable guide in searching for the B_c^+ excited states. And important difference in the predictions is that in the Eichten-Quigg calculation [30] the $1P_1$ states are almost pure ${}^3P_1$ and ${}^1P_1$ with little mixing while in other models there is significant mixing. This arises from the much smaller expectation value of the off-diagonal mixing term in the Eichten-Quigg calculation [30] compared to the other models. Since, after rotating from the $j-j$ basis to the $L-S$ basis, the $L-S$ mixing term given by Eichten and Quigg is in agreement with Equation 1.10, the differences in expectation values can only be attributed to differences in the cancellations between the short and long distance pieces in Equation 1.10, i.e. between the $\frac{4}{3}\frac{\alpha_s}{r^3}$ and $\frac{b}{r}$ pieces. This reflects subtle differences in the $q\bar{q}$ potentials of different models. The study of B_c^+ spectroscopy will help test and refine the quark potential models but more importantly will test Lattice QCD, non-relativistic QCD

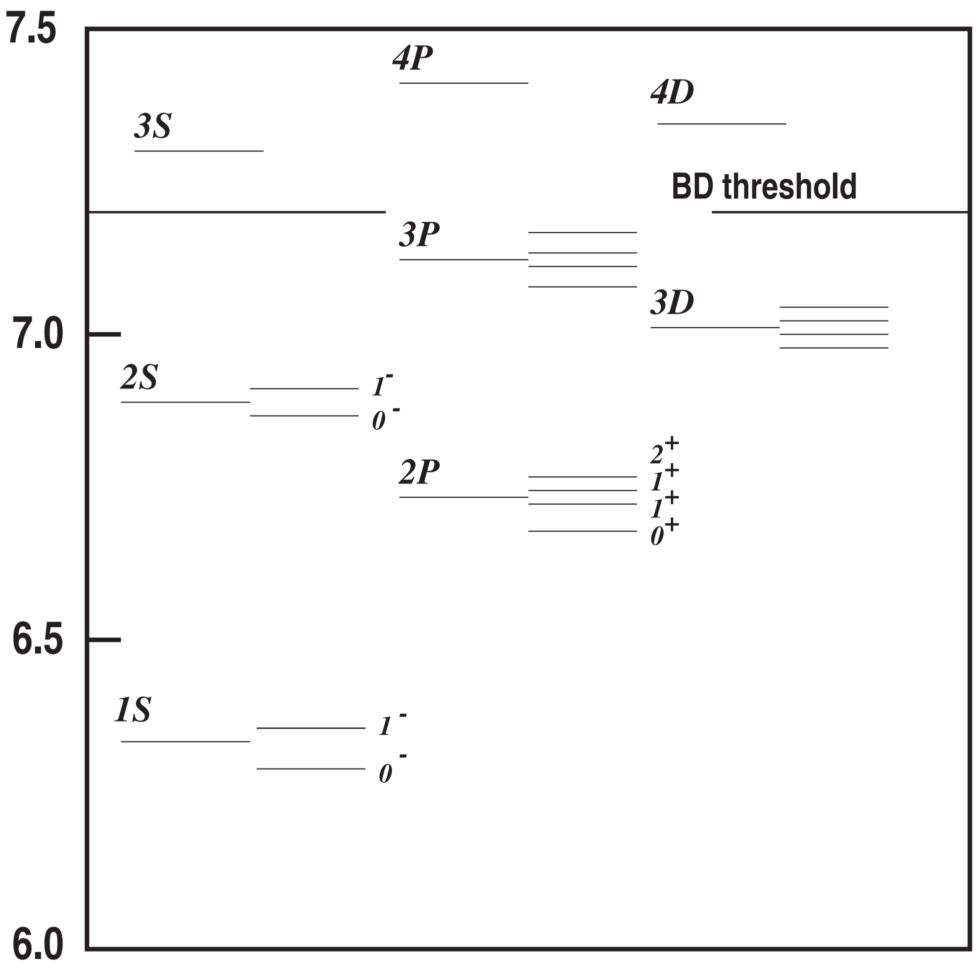

Figure 1.5: The mass spectrum of $(c\bar{b})$ with account for the spin-dependent splittings.

(NRQCD), and perturbative non-relativistic QCD (pNRQCD), etc., which are more directly connected to QCD.

1.4.2 B_c^+ meson lifetime

Recent calculation of the B_c^+ lifetime is performed using several tools. The first tool is the perturbative calculations of Wilson coefficients determined by the hard corrections with the use of renormalization group improvements. The second instrument is the Operator Product Expansion (OPE) related with the small virtuality of heavy quark in the bound state, which reveals itself in many faces such as the general expansion of operators in inverse powers of heavy quark mass and the QCD sum rules. A specific form of OPE is the application for the heavy quark Lagrangian itself, which results in the effective theories of heavy quarks. The effective theory is constructed under the choice of its leading term appropriate for the system under

State	GI [25]	EFG [31]	FUII [32]	GKLT [33]	EQ [30]	GJ [34]	ZVR [35]	Lattice [36]
1^3S_1	6338	6332	6341	6317	6337	6308	6340	6321±20
1^1S_0	6271	6270	6286	6253	6264	6247	6260	6280±30±190
1^3P_2	6768	6762	6772	6743	6747	6773	6760	6783±30
$1P_1'$	6750	6749	6760	6729	6736	6757	6740	6765±30
$1P_1$	6741	6734	6737	6717	6730	6738	6730	6743±30
1^3P_0	6706	6699	6701	6683	6700	6689	6680	6727±30
θ_{1P}	22.4°	20.4°	28.5°	17.1°	$\sim -0.2°$	25.6°		33.4±1.5°
2^3S_1	6887	6881	6914	6902	6899	6886	6900	6990±80
2^1S_0	6855	6835	6882	6867	6856	6853	6850	6960±80
2^3P_2	7164	7156		7134	7153		7160	
$2P_1'$	7150	7145		7124	7142		7150	
$2P_1$	7145	7126		7113	7135		7140	
2^3P_0	7122	7091		7088	7108		7100	
θ_{2P}	18.9°	23.2°		21.8°	−17°			
3^3S_1	7272	7235			7280		7280	
3^1S_0	7250	7193			7244		7240	
1^3D_3	7045	7081	7032	7007	7005		7040	
$1D_2'$	7036	7079	7028	7016	7009		7030	
$1D_2$	7041	7077	7028	7001	7012		7020	
1^3D_1	7028	7072	7019	7008	7012		7010	
θ_{1D}	44.5°	−35.9°		−34.5°				
1^3F_4	7271						7250	
$1F_3'$	7266						7250	
$1F_3$	7276						7240	
1^3F_2	7269						7240	
θ_{1F}	41.4°							

Table 1.4: Predicted masses and Spin-Orbit mixing angles. The $P_1' - P_1$, $D_2' - D_2$, $F_3' - F_3$ states and mixing angles are defined using the convention of Equation 1.11.

study. So, the kinetic energy can be neglected in the heavy-light hadrons to the leading order. The corresponding effective theory is called Heavy Quark Effective Theory (HQET) [37]. In the doubly heavy mesons the kinetic energy is of the same order as the potential one, while the velocity of the heavy quark motion is small, and we deal with the non-relativistic QCD (NRQCD) [38] and its developments by taking into account the static energy in the potential NRQCD in a general form (pNRQCD) [39] or under the correlation of quarkonium size and the time for the formation of bound system with the improved scheme of expansion in the heavy quark velocity (vNRQCD) [40].

The B_c^+ meson allows us to use such advantages like the non-relativistic motion of $\bar{b}$ and c quarks similar to what is know in the heavy quarkonia $b\bar{b}$ and $c\bar{c}$, and suppression of light degrees of freedom: the quark-gluon sea is small in the heavy quarkonia. These two physical conditions imply two small expansion parameters for B_c^+:

- the relative velocity of quarks v,
- the ratio of confinement scale to the heavy quark mass $\Lambda_{\mathrm{QCD}}/m_Q$.

The perturbative QCD remains actual in the effective theories, since it is necessary for the calculation of Wilson coefficients determined by hard corrections. More definitely, the perturbative calculations determine both the matching of Wilson coefficients in the effective theory with the full QCD and the anomalous dimensions resulting in the evolution of the coefficients with the variation of normalization point. In this respect, the pNRQCD results on the static potential and the mass-dependent terms in the heavy quark-antiquark energy were confirmed by vNRQCD after appropriate limits and some calculational corrections in vNRQCD. In addition, the pNRQCD is a powerful tool in the studies of both the spectroscopy and the heavy quarkonium decays.

In contrast to the Wilson coefficients, the hadronic matrix elements of operators composed by the effective fields of non-relativistic heavy quarks cannot be evaluated in the perturbative manner. So, one should use the non-perturbative methods such as the QCD sum rules, OPE for inclusive estimates and potential models.

The B_c^+ decay can take place in three ways; (1) the $\bar{b}$-quark decay with the spectator c-quark, (2) the c-quark decay with the spectator $\bar{b}$-quark and (3) the annihilation channel. The diagrams for the three modes of the decay are shown in Figure 1.6. The total width of the decay is summed from the these partial widths,

$$\Gamma(B_c^+ \to X) = \Gamma(\bar{b} \to \bar{c}) + \Gamma(c \to s) + \Gamma(ann.) + \cdots . \tag{1.12}$$

As one of other contributions to the decay width, there is a Pauli interference contribution to the $\bar{b} \to \bar{c}c\bar{s}$ decay from the c-quark spectator. The simplest estimates with no account for the quark binding inside the B_c^+ meson and in the framework of the spectator mechanism of the

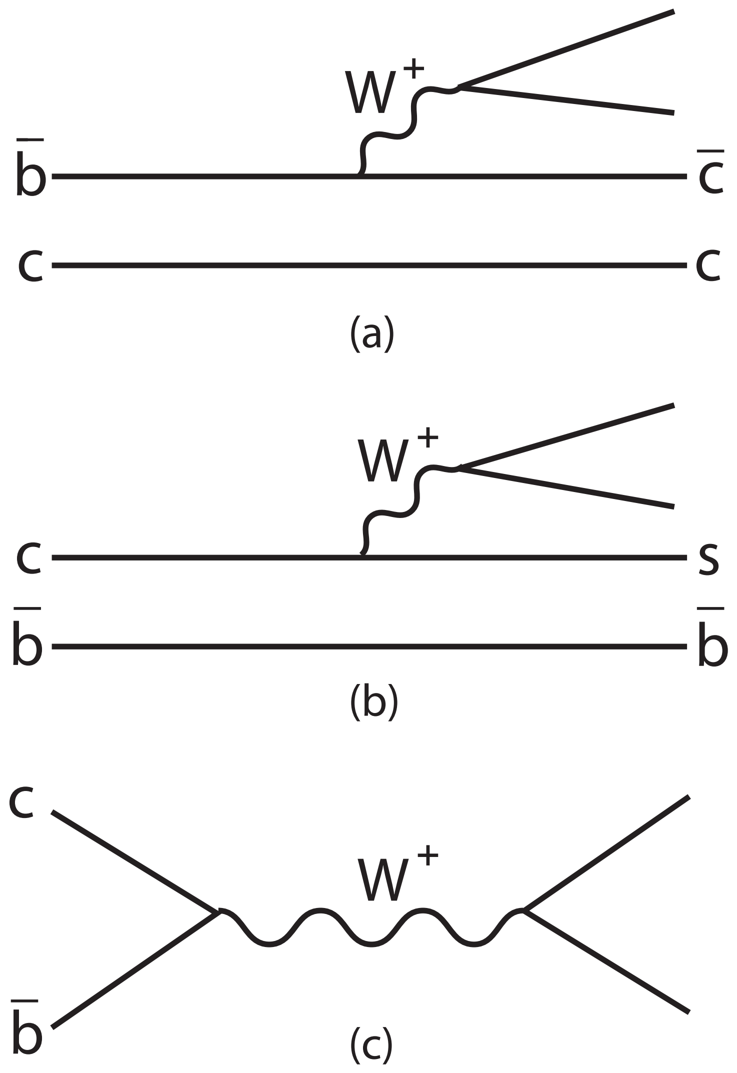

Figure 1.6: The diagrams of the B_c^+ decays; (a) the c-quark spectator; (b) the $\bar{b}$-quark spectator decays; (c) the annihilation decays.

decay for the first and second cases, lead to the expressions

$$\Gamma(\bar{b} \to \bar{c}) = 9\frac{G_F^2 \mid V_{cb} \mid^2 m_b^5}{192\pi^3}, \tag{1.13}$$

$$\Gamma(c \to s) = 5\frac{G_F^2 \mid V_{cs} \mid^2 m_c^5}{192\pi^3}, \tag{1.14}$$

where m_b and m_c are effective quark masses for bottom and charm quarks.

For the annihilation channel the $\Gamma(ann.)$ width can be reliably estimated in the framework of inclusive approach, where one takes the sum of the leptonic and quark decay modes with account for the hard gluon corrections to the effective four-quark interaction of weak currents. The width is expressed through the leptonic constant of $f_{B_c} \approx 400$ MeV. This estimate of the quark-contribution does not depend on a hadronization model, since a large energy release of the order of the meson mass takes place. The width of the annihilation channel can be expressed as :

$$\Gamma(ann.) = \sum_i \frac{G_F^2}{8\pi} \mid V_{cb} \mid^2 M_{B_c} m_i^2 \left(1 - \frac{m_i^2}{M_{B_c}^2}\right)^2 f_{B_c}^2 C_i, \tag{1.15}$$

where $C_i = 1$ for the $\tau\nu_\tau$ channel, $C_i = 3 \mid V_{cs} \mid^2$ for the $c\bar{s}$ channel, and m_i is the mass of the heaviest fermion (τ or c).

As for the non-annihilation decays, in the approach of the OPE for the quark currents of weak decays [41], one takes into account the α_s-corrections to the free quark decays and uses the quark-hadron duality for the final states. Then one considers the matrix element for transition operator over the bound meson state. The latter allows one also to take into account the effects caused by the motion and virtuality of decaying quark inside the meson because of the interaction with the spectator. In this way the $\bar{b} \to \bar{c}c\bar{s}$ decay mode turns out to be suppressed almost completely due to the Pauli interference with the c-quark from the initial state. Besides, the c-quark decays with the spectator $\bar{b}$-quark are essentially suppressed in comparison with the free quark decays because of a large bound energy in the initial state.

The three widths can be calculated from the known parameters in Equation 1.13, 1.14 and 1.15. From these calculations one can get a rough estimate on the lifetime, which should be of the order of $\tau_{B_c} \approx (2-5) \times 10^{-13}$ s. However, these estimates do not take into consideration the strong binding of the quarks in the B_c^+ meson. After incorporating the corrections due to the strong binding of the quarks in the B_c^+, the three processes for the B_c^+ meson decay result in an approximate estimate for the B_c^+ lifetime, which is quoted as

$$\tau_{B_c} \approx 5 \times 10^{-13} \text{ s}. \tag{1.16}$$

In this estimate, the fraction of the b-quark decay, c-quark decay and the annihilation decay are comparable size. Most of the uncertainty in the B_c^+ lifetime comes from the choice of the quark masses.

In the framework of exclusive approach, it is necessary to sum up widths of different decay modes calculated in the potential models [42, 43]. While considering the semileptonic decays due to the $\bar{b} \to \bar{c}\ell^+\nu_\ell$ and $c \to s\ell^+\nu_\ell$ transitions, one finds that in the former decays the hadronic final states are practically saturated by the lightest bound $1S$-state in the $(c\bar{c})$-system, i.e. by the η_c and J/ψ particles, and in the latter decays the $1S$-states in the $(\bar{b}s)$-system, i.e. B_s and B_s^*, which can only enter the accessible energetic gap. The energy release in the latter transition is low in comparison with the meson masses, and, therefore, a visible deviation from the picture of quark-hadron duality is possible. Numerical estimates show that the value of $B_c^+ \to (\bar{b}s)\ell^+\nu_\ell$ decay width is two times less in the exclusive approach than in the inclusive method, though this fact can be caused by the choice of narrow wave package for the $B_s^{(*)}$ mesons in the quark model, so that $f_{B_s} \approx 150$ MeV, while in the limit of static heavy quark, one should expect a larger value for the leptonic constant [37, 44]. This increase will lead to the widening of the wave package and, hence, to the increase of the overlapping integral for the wave functions of B_c^+ and B_c^{*+}.

Further, the $\bar{b} \to \bar{c}u\bar{d}$ channel, for example, can be calculated through the given decay width of $\bar{b} \to \bar{c}\ell^+\nu_\ell$ with account for the color factor and hard gluon corrections to the four-quark interaction. It can be also obtained as a sum over the widths of decays with the $(u\bar{d})$-system bound states.

The result of calculation for the total B_c^+ width in the inclusive OPE approach is

$$\tau_{B_c^+} = 0.55 \pm 0.15 \text{ ps}, \tag{1.17}$$

where the most significant uncertainty is related to the choice of quark masses (especially for the charm quark) [45]. Table 1.5 [41] shows the variations of the B_c^+ lifetime with various quark masses in the OPE framework. From the physics picture, the quark effective masses should have more precise meaning and be good to involve certain non-perturbative QCD effects [46]. The rates of direct $\bar{b}$ and c decays, which dominate the lifetime of the B_c^+ meson, are proportional to m_Q^5, the B_c^+ meson lifetime is somewhat sensitive to the m_Q values.

In Table 1.6 several predictions of the B_c^+ meson lifetime are also shown. These estimations mostly agree with the experimental result measured by CDF Run-I [22], $0.46^{+0.18}_{-0.16} \pm 0.03$ ps. As a result of the lifetime estimations, predictions of the exclusive decay channels of B_c^+ meson are summarized in Table 1.7 [45].

1.4.3 Hadronic production of the B_c^+ mesons

The B_c^+ meson carries two heavy flavors explicitly, so to produce it in the most favorable manner is to reduce two pairs of heavy quarks: c, $\bar{c}$, b, $\bar{b}$ first, and then the two heavy quarks c, $\bar{b}$ of them combine into the meson by certain possibility. Two pairs of the quarks c, $\bar{c}$, b, $\bar{b}$ are so heavy that their production always in the perturbative region of QCD, while the "possibility" to combine the two heavy quarks c, $\bar{b}$ into the meson, being non-perturbative nature, relates

Parameters [GeV/c^2]	$\Gamma(\sum \bar{b} \to \bar{c})$	$\Gamma(\sum c \to s)$	Γ(PI)	Γ(WA)	τ_{B_c}
$m_b = 5.0, m_c = 1.5, m_s = 0.20$	0.694 ps^{-1}	1.148 ps^{-1}	-0.115 ps^{-1}	0.193 ps^{-1}	0.54 ps
$m_b = 4.8, m_c = 1.35, m_s = 0.15$	0.576 ps^{-1}	0.725 ps^{-1}	-0.132 ps^{-1}	0.168 ps^{-1}	0.75 ps
$m_b = 5.1, m_c = 1.6, m_s = 0.45$	0.635 ps^{-1}	1.033 ps^{-1}	-0.101 ps^{-1}	0.210 ps^{-1}	0.55 ps
$m_b = 5.1, m_c = 1.6, m_s = 0.20$	0.625 ps^{-1}	1.605 ps^{-1}	-0.101 ps^{-1}	0.210 ps^{-1}	0.43 ps
$m_b = 5.05, m_c = 1.55, m_s = 0.20$	0.623 ps^{-1}	1.323 ps^{-1}	-0.107 ps^{-1}	0.201 ps^{-1}	0.48 ps
$m_b = 5.0, m_c = 1.5, m_s = 0.15$	0.620 ps^{-1}	1.204 ps^{-1}	-0.114 ps^{-1}	0.193 ps^{-1}	0.53 ps

Table 1.5: The value of B_c^+ meson lifetime together with the spectator and non-spectator contributions, $\sum \bar{b} \to \bar{c}$, $\sum c \to s$, Pauli Interference (PI), Weak Annihilation (WA), to the width at various choices of parameters in the OPE framework.

Reference	τ_{B_c} [ps]	Remarks
M. Beneke *et al.* [47]	0.55 ± 0.15	Operator Product Expansion with NRQCD
A. El-Hady *et al.* [49]	$0.46 \sim 0.47$	Bethe-Salpeter Model
A. Yu. Anisimov *et al.* [50]	0.59 ± 0.06	Light-Front Constituent Quark Model
A. Yu. Anisimov *et al.* [51]	0.63 ± 0.02	Light-Front ISGW Model
V. V. Kiselev [52]	0.55 ± 0.1	Hard-Soft Factorization
V. V. Kiselev *et al.* [48]	0.48 ± 0.05	QCD Sum Rules

Table 1.6: Several predictions of the B_c^+ lifetime.

Mode	BR, %	Mode	BR, %	Mode	BR, %
$B_c^+ \to \eta_c e^+\nu$	0.75	$B_c^+ \to J/\psi K^+$	0.011	$B_c^+ \to B_s^0 K^+$	1.06
$B_c^+ \to \eta_c \tau^+\nu$	0.23	$B_c^+ \to J/\psi K^{*+}$	0.022	$B_c^+ \to B_s^{*0} K^+$	0.37
$B_c^+ \to \eta_c' e^+\nu$	0.041	$B_c^+ \to D^+ \bar{D}^0$	0.0053	$B_c^+ \to B_s^0 K^{*+}$	-
$B_c^+ \to \eta_c' \tau^+\nu$	0.0034	$B_c^+ \to D^+ \bar{D}^{*0}$	0.0075	$B_c^+ \to B_s^{*0} K^{*+}$	-
$B_c^+ \to J/\psi e^+\nu$	1.9	$B_c^+ \to D^{*+} \bar{D}^0$	0.0049	$B_c^+ \to B^0 \pi^+$	1.06
$B_c^+ \to J/\psi \tau^+\nu$	0.48	$B_c^+ \to D^{*+} \bar{D}^{*0}$	0.033	$B_c^+ \to B^0 \rho^+$	0.96
$B_c^+ \to \psi(2S) e^+\nu$	0.132	$B_c^+ \to D_s^+ \bar{D}^0$	0.00048	$B_c^+ \to B^{*0} \pi^+$	0.95
$B_c^+ \to \psi(2S) \tau^+\nu$	0.011	$B_c^+ \to D_s^+ \bar{D}^{*0}$	0.00071	$B_c^+ \to B^{*0} \rho^+$	2.57
$B_c^+ \to D^0 e^+\nu$	0.004	$B_c^+ \to D_s^{*+} \bar{D}^0$	0.00045	$B_c^+ \to B^0 K^+$	0.07
$B_c^+ \to D^0 \tau^+\nu$	0.002	$B_c^+ \to D_s^{*+} \bar{D}^{*0}$	0.0026	$B_c^+ \to B^0 K^{*+}$	0.015
$B_c^+ \to D^{*0} e^+\nu$	0.018	$B_c^+ \to \eta_c D_s^+$	0.86	$B_c^+ \to B^{*0} K^+$	0.055
$B_c^+ \to D^{*0} \tau^+\nu$	0.008	$B_c^+ \to \eta_c D_s^{*+}$	0.26	$B_c^+ \to B^{*0} K^{*+}$	0.058
$B_c^+ \to B_s^0 e^+\nu$	4.03	$B_c^+ \to J/\psi D_s^+$	0.17	$B_c^+ \to B^+ \bar{K}^0$	1.98
$B_c^+ \to B_s^{*0} e^+\nu$	5.06	$B_c^+ \to J/\psi D_s^{*+}$	1.97	$B_c^+ \to B^+ \bar{K}^{*0}$	0.43
$B_c^+ \to B^0 e^+\nu$	0.34	$B_c^+ \to \eta_c D^+$	0.032	$B_c^+ \to B^{*+} \bar{K}^0$	1.60
$B_c^+ \to B^{*0} e^+\nu$	0.58	$B_c^+ \to \eta_c D^{*+}$	0.010	$B_c^+ \to B^{*+} \bar{K}^{*0}$	1.67
$B_c^+ \to \eta_c \pi^+$	0.20	$B_c^+ \to J/\psi D^+$	0.009	$B_c^+ \to B^+ \pi^0$	0.037
$B_c^+ \to \eta_c \rho^+$	0.42	$B_c^+ \to J/\psi D^{*+}$	0.074	$B_c^+ \to B^+ \rho^0$	0.034
$B_c^+ \to J/\psi \pi^+$	0.13	$B_c^+ \to B_s^0 \pi^+$	16.4	$B_c^+ \to B^{*+} \pi^0$	0.033
$B_c^+ \to J/\psi \rho^+$	0.40	$B_c^+ \to B_s^0 \rho^+$	7.2	$B_c^+ \to B^{*+} \rho^0$	0.09
$B_c^+ \to \eta_c K^+$	0.013	$B_c^+ \to B_s^{*0} \pi^+$	6.5	$B_c^+ \to \tau^+ \nu_\tau$	1.6
$B_c^+ \to \eta_c K^{*+}$	0.020	$B_c^+ \to B_s^{*0} \rho^+$	20.2	$B_c^+ \to c\bar{s}$	4.9

Table 1.7: Branching fractions [45] of exclusive B_c^+ decays at the fixed choice of factors: $a_1^c = 1.20$ and $a_2^c = -0.317$ in the non-leptonic decays of c-quark, and $a_1^b = 1.14$ and $a_2^b = -0.20$ in the non-leptonic decays of $\bar{b}$-quark. The lifetime of B_c^+ is appropriately normalized by $\tau_{B_c} \approx 0.45$ ps.

to a relevant matrix element in non-relativistic QCD (NRQCD) framework (for color-singlet production it can be related to the wave function of B_c^+ at origin in potential model framework) directly [53]. Therefore the production of B_c^+ meson may be always estimated by perturbative QCD (pQCD) with proper factorization formulation [53, 54, 55, 56, 57, 58].

Since the production cross section is relatively small in comparison with the production of the other heavy mesons (B, D etc.) and heavy quarkonia (J/ψ, Υ etc.), only at high energy hadronic colliders with high luminosity, can one collect enough B_c^+ events for experimental studies. The hadronic production of the B_c^+-states with different spin has been estimated by a lot of people, and all are mainly based on the gluon-gluon fusion mechanism, i.e. taking the hard subprocess $gg \to B_c^+ + b + \bar{c}$ as dominant one.

There are two theoretical approaches of pQCD to the estimate of its production: the so-called "fragmentation approach" [55] and the so-called "complete calculation approach" of the lowest-order perturbative QCD [53, 56, 57, 58]. There are several mechanisms for the hadronic production of B_c^+ meson, in most p_T (transverse momentum of the produced B_c^+ meson) region, the so-called "gluon-gluon fusion" mechanism is dominant [56, 57]. Since only LO estimates of B_c^+ production are available up-to now, so several important theoretical uncertainties for LO estimate are investigated [57]. Recently the P-wave excited B_c^+ production not only via its color-singlet component but also via its color-octet components is estimated, and it is pointed out that the P-wave production can be sizable [58]. The results of the two approaches agree essentially within theoretical uncertainties, especially, at high B_c^+ transverse momentum p_T and when the "fragmentation approach" additionally takes into account the contributions from gluon fragmentation. The "fragmentation approach" is appropriate if one is only interested in the information of the produced B_c^+ itself, and its accuracy is improving with the increasing of p_T. Comparatively, the advantage of the "complete approach" is that it can also retain the information of the accompanied c and $\bar{b}$ quarks (jets). For experiments, to retain more information of the events is more relevant.

Moreover according to pQCD, in addition to the gluon-gluon fusion mechanism, there are several different mechanisms for the production, such as that via quark-antiquark annihilation subprocess $q\bar{q} \to B_c^+ + b + \bar{c}$, and that via the color-octet mechanism and etc.. In Ref. [56], it is shown that the contributions to the production from quark-antiquark annihilation are much smaller than those from gluon-gluon fusion. It is mainly because of the fact that the relevant luminosity for gluon-gluon fusion is a product of the parton distribution functions (PDFs) for gluon components in the colliding hadrons, whereas that for quark-antiquark annihilation is a product of the quark and anti-quark distribution functions respectively while in a high energy collider, such as Tevatron ($p\bar{p}$ collision $\sqrt{s} \sim 2$ TeV) at Fermilab and LHC (pp collision $\sqrt{s} \sim 14$ TeV) at CERN, the luminosity for gluon-gluon fusion due to parton distribution functions at the most kinematic region is much higher than that for quark-antiquark annihilation [59]. Furthermore, in the annihilation subprocess, there is an additional S-channel suppression from the virtual gluon propagator, which will also make contributions to the production cross section small. According to NRQCD [60], for a double heavy meson, such as J/ψ, η_c, B_c^+, ..., there may be additional color-octet components which may contribute the production substantially. The magnitude of the color-octet components may be estimated with the NRQCD velocity scaling rule ($v \simeq \alpha_s(M_{B_c}) \sim 0.1$). One may find that there is no enhancement in the hadronic production (in contract to of the hidden flavored double heavy objects such as J/ψ, $\psi(2S)$ the production which can gain one order or more in α_s via the color octet components) and the color-octet components in B_c^+ are definitely smaller than the color-singlet ones (with the same input parameters, the total contributions to the hadronic production is $\leq v \sim v^2$ of the color-singlet one), therefore, the contributions from color-octet components of B_c^+ are ignorable at leading order.

There are 36 Feynman diagrams for the gluon-gluon fusion subprocess. The typical Feynman diagrams for the subprocess are plotted in Fig 1.7(a). In comparison, for the other mechanism, its subprocess is of quark-antiquark annihilation and there are 7 Feynman diagrams. The typical ones are plotted in Figure 1.7(b).

To be more useful experimentally, the uncertainties of B_c^+ hadronic production is studied by means of the "complete approach". At collision C.M. energy $\sqrt{s}$, $d\sigma$ of B_c^+ can be expressed as:

$$\begin{aligned} d\sigma(s, p_T, \cdots) &= \sum_{ij} \int dx_1 \int dx_2 F^i_{H_1,P_1}(x_1, \mu_F^2) \cdot F^j_{H_2,P_2}(x_2, \mu_F^2) \\ &\cdot \; d\hat{\sigma}_{ij\to B_c^+ b\bar{c}}(P_1, P_2, x_1, x_2, \mu_F^2, \hat{s}, p_T, \cdots), \end{aligned} \tag{1.18}$$

where $F^i_{H_1,P_1}(x_1, \mu_F^2)$ and $F^j_{H_2,P_2}(x_2, \mu_F^2)$ are the PDFs of incoming hadrons H_1 (momentum P_1) and H_2 (momentum P_2) for parton i (with the momentum fraction x_1) and parton j (with the momentum fraction x_2) respectively: μ_F is the energy scale where the factorization, renormalization for the PDFs, and the hard subprocess are made: $d\hat{\sigma}_{ij\to B_c^+ b\bar{c}}$ is the differential cross-section of the relevant hard subprocess, in which $\hat{s} = x_1 x_2 s$ is the c.m.s energy of the subprocess and p_T is the transverse momentum of B_c^+.

The Uncertainties Relevant to the Parameters of Potential Model and Masses of Quarks and the Meson

For all the approaches and the color-singlet mechanisms to the B_c^+ production, the "decay constant" f_{B_c} relating the hadron matrix element, as one of important input-parameters, is needed as input, and so far it may be calculated either by potential model [61] or by lattice QCD [36]. Within potential model, it directly relates to the wave function at the origin of the binding system in terms of the following formula,

$$f_{B_c}^2 = \frac{12 \mid \Psi_{[1S]}(0) \mid^2}{M_{B_c}}, \tag{1.19}$$

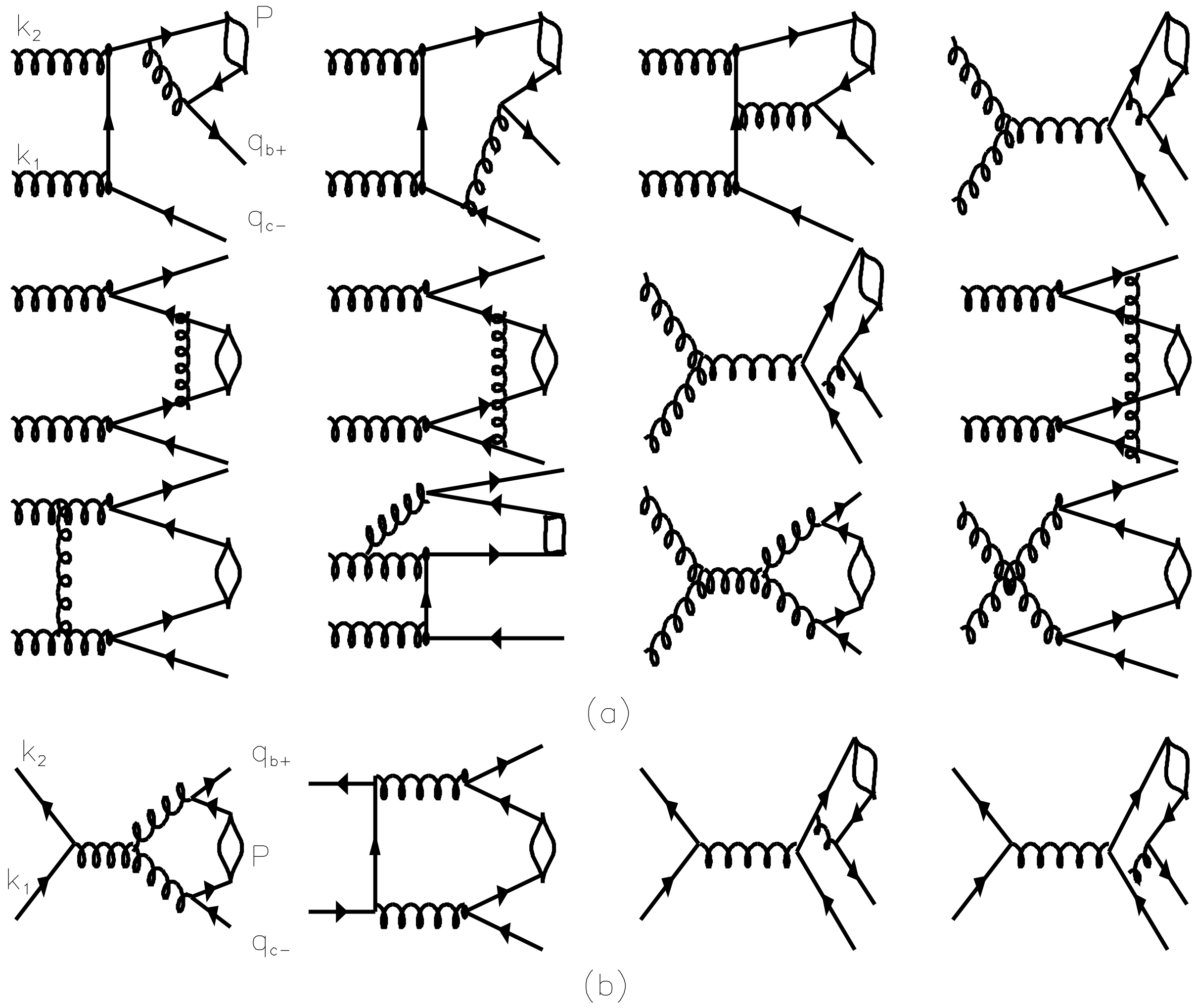

Figure 1.7: (a) The typical Feynman diagrams for the gluon-gluon fusion subprocess: (b) The typical Feynman diagrams for quark-antiquark annihilation subprocess.

-	Tevatron ($\sqrt{s} = 2.0$ TeV)						LHC ($\sqrt{s} = 14$ TeV)					
m_c (GeV/c^2)	1.3	1.4	1.5	1.6	1.7	1.8	1.3	1.4	1.5	1.6	1.7	1.8
$\sigma(B_c^+)$ (nb)	4.84	3.87	3.12	2.56	2.12	1.76	75.6	61.0	49.8	41.4	34.7	28.9
$\sigma(B_c^{*+})$ (nb)	12.3	9.53	7.39	5.92	4.77	3.87	194.	153.	121.	97.5	80.0	66.2

Table 1.8: The total cross section (in unit nb) [62] for hadronic production of $B_c^+[1^1S_0]$ and $B_c^{*+}[1^3S_1]$ with various values of the c-quark mass m_c and fixed b-quark mass $m_b = 4.9$ GeV/c^2. For definiteness and focusing the uncertainties from the quark masses alone, the rest uncertainty sources are fixed: the mass of the meson B_c^+, $M_{B_c} = m_c + m_b$; the gluon distribution function is taken from CTEQ5L; the factorization energy scale is chosen $\mu_F^2 = Q^2 = \hat{s}/4$ and the running α_s is of leading order.

where M_{B_c} is the B_c^+ meson mass, $\Psi_{[1S]}$ is the wave function at the origin of the binding system $(c\bar{b})$ at the $[1S]$ level. Since the spin splitting effects are ignored here, so there is no difference for the decay constant between the spin stats $[^1S_0]$ and $[^3S_1]$. There are several parameters in the potential model, which need to be fixed by fitting the experimental data of the heavy quarkonia ($(c\bar{c})$ and $(b\bar{b})$), so when computing the spectrum and the wave functions of the $(c\bar{b})$ system [61], certain uncertainties from the fitting procedure will cause some uncertainties of f_{B_c}. In the leading order (LO) approximation for the production, f_{B_c} appears in the amplitude as a linear factor exactly, so the production cross section is proportional to it squared. Therefore, the uncertainties in the production form f_{B_c} can be figured out straightforwardly, so the value $f_{B_c} = 0.48$ GeV is fixed here for the ground states.

In addition to the decay constant f_{B_c}, the quark mass value m_c and m_b also "generate" uncertainties for the hadronic production. If all of the rest parameters in the potential might be fixed, then the values of quark masses would determine the decay constant f_{B_c}, the meson mass M_{B_c} and etc. completely. However at present, the parameters in potential model, which also appear in the Equation 1.18, cannot be completely fixed by fitting the available data of the heavy quarkonia, so the relations of the quark masses to the decay constant f_{B_c}, the meson mass and etc. cannot be well determined. Therefore, when studying the uncertainties for the hadronic production, we can consider all of the factors, explicitly appearing in the potential model and in the formula for the subprocess Equation 1.18, in a "factorized" way. Furthermore, since B_c^+ is the non-relativistic and weak-binding bound state, at LO the relative momentum between the constitute quarks can be ignored, e.g. $M_{B_c} \approx m_b + m_c$. The uncertainties from m_c are indicated by the calculated total cross sections, as in Table 1.8 [62]. The uncertainties from m_b can be analyzed in a similar way and tabulated in Table 1.9 [62]. For the tables, one may observe how the values of m_c and m_b affect the cross section up to a sizable degree.

-	Tevatron ($\sqrt{s} = 2.0$ TeV)					LHC ($\sqrt{s} = 14$ TeV)				
m_b (GeV/c^2)	4.5	4.7	4.9	5.1	5.3	4.5	4.7	4.9	5.1	5.3
$\sigma(B_c^+)$ (nb)	4.10	5.33	3.12	2.70	2.38	63.4	56.2	49.8	44.1	39.6
$\sigma(B_c^{*+})$ (nb)	9.43	8.35	7.39	6.59	5.89	148.	133.	121.	110.	100.

Table 1.9: The total cross section (in unit nb) [62] for hadronic production of $B_c^+[1^1S_0]$ and $B_c^{*+}[1^3S_1]$ with various values of the b-quark mass m_b and fixed c-quark mass $m_c = 1.5$ GeV/c^2. For definiteness and focusing the uncertainties from the quark masses alone, the gluon distribution function is taken from CTEQ5L; the factorization energy scale is chosen $\mu_F^2 = Q^2 = \hat{s}/4$ and the running α_s is of leading order.

Uncertainties Relevant to the QCD Parameters and PDFs

In this sub-section, only gluon-gluon fusion mechanism is focused on. As shown in Equation 1.18, PDFs $F^i_{H_1,P_1}(x_1,\mu_F^2)$ and $F^j_{H_2,P_2}(x_2,\mu_F^2)$ with H_1=proton, H_2=proton for LHC; H_1=proton, H_2=anti-proton for Tevatron generate uncertainties in the production. PDFs are of non-perturbative nature, and in Equation 1.18 they have been factorized out at the energy scale μ_F^2 with the help of pQCD factorization theorem.

Usually the factorization is carried out at Q^2, a characteristic energy scale for the hard subprocess, i.e. $\mu_F^2 = Q^2$, so Q^2 and μ_F^2 on the equal footing are used here. All the estimates of the production are leading (the lowest) order of pQCD and then how to choose the energy scale Q^2 is a very tricky problem. If Q^2 is chosen properly, the results may be quite accurate. From experience, for a hard subprocess with a two-body final state, generally when taking $Q^2 = \hat{s}/4$, we can achieve quite an accurate result for LO calculations. However, in the present case, the gluon-gluon fusion subprocess is of three-body final state and contain heavy quarks, so there are ambiguities in choosing Q^2 and various choices of Q^2 would generate quite different results. Since such kind of ambiguity cannot be justified by the LO calculation itself, so it is necessary to take the Q^2 variations as the uncertainty of the LO calculation.

According to the factorization, the running of α_s and PDFs should be on leading logarithm order (LLO), and the energy scale Q^2 appearing in the calculation should be taken as one of the possible characteristic energy scales of the hard subprocess. In principle, there are several typical ways to choose the scale Q^2 and to relate it to a characteristic energy scale ($Q^2 \gg \Lambda^2_{QCD}$) of the subprocess, such as $Q^2 = 4m_c^2$, $Q^2 = p_T^2 + M^2_{B_c}$, $Q^2 = \hat{s}/4$ and *etc.*. The PDFs can be obtained only through global fitting of the experimental data and evolute them to the requested characteristic scale Q^2 in standard way of pQCD. For comparison between Tevatron and LHC and to pinpoint the uncertainties from PDFs, α_s running and the choices of the characteristic energy scale Q^2, the production cross sections are calculated according to three types of PDFs, the strong coupling α_s up to LLO fixed by the PDFs and the characteristic Q^2. The obtained

	CTEQ6L	GRV98L	MRST2001L	CTEQ6L	GRV98L	MRST2001L
-	$Q^2 = \hat{s}/4$			$Q^2 = p_T^2 + M_{B_c}^2$		
-	Tevatron					
$\sigma(B_c^+)$	3.79	3.27	3.40	5.50	4.54	4.86
$\sigma(B_c^{*+})$	9.07	7.88	8.16	13.4	11.1	11.9
-	LHC					
$\sigma(B_c^+)$	53.1	53.9	47.5	71.1	70.0	61.4
$\sigma(B_c^{*+})$	130.	131.	116.	177.	172.	153.

Table 1.10: Total cross section [62] for the hadronic production of $B_c^+[1^1S_0]$ and $B_c^{*+}[1^2S_1]$ at Tevatron and at LHC with the leading logarithm order (LLO) running α_s and the characteristic energy scale $Q^2 = \hat{s}/4$ or $Q^2 = p_T^2 + M_{B_c}^2$. The cross section is in unit of nb.

C.M. energy	1.8 TeV	1.9 TeV	1.96 TeV	2.0 TeV
$\sigma(B_c^+)$	0.40	0.44	0.46	0.47
$\sigma(B_c^{*+})$	1.00	1.09	1.14	1.18

Table 1.11: The integrated hadronic cross section for Tevatron at different C.M. energies [62]. The gluon distribution is chosen from CTEQ5L and the characteristic energy scale of the production is chosen as $Q^2 = \hat{s}/4$. In addition, a cut for transverse momentum p_T ($p_T > 5$ GeV/c) and a cut for rapidity y ($\mid y \mid < 1.5$) have been applied. The cross section is in unit of nb.

results are shown in Table 1.10 [62]. In Figure 1.8, 1.9 and 1.10 [62], the production cross section of the B_c^+ meson as a function of p_T and y with different PDFs, different choices of Q^2 and α_s are plotted. As can be seen, choice of energy scale Q^2 gives the biggest effect on the B_c^+ production cross section.

Finally, the cross section for B_c^+ meson production is quite sensitive to the C.M. energy of the collider. Since Run-II of Tevatron is running now at a slightly higher energy than that 1.8 TeV of Run-I, Tevatron is taken as an example to study the increase caused by slight changes in the C.M. energy. The cross section of B_c^+ is calculated as function of C.M. energy (1.8, 1.9, 1.96 and 2.0 TeV) at Tevatron. The obtained results for the values of the integrated cross-section with suitable cuts ($p_T > 5$ GeV/c, and $\mid y \mid < 1.5$) are shown in Table 1.11 [62].

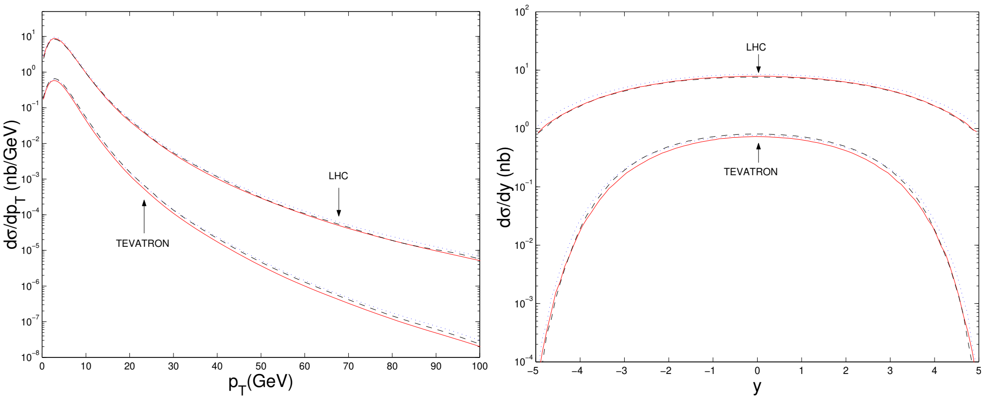

Figure 1.8: B_c^+ differential distributions versus its transverse momentum p_T and rapidity y for different versions of gluon distributions in leading order [62]. The characteristic energy scale is taken as $Q^2 = \hat{s}/4$. Solid line: CTEQ5L; dotted line: GRV98L and dashed line: MRST2001L. The lower (upper) three lines corresponding to the distributions in Tevatron (LHC).

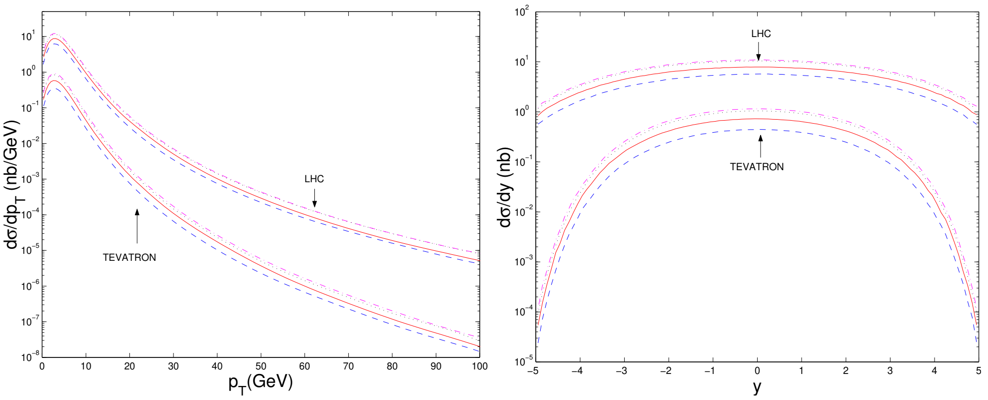

Figure 1.9: B_c^+ differential distributions versus its transverse momentum p_T and rapidity y for four typical choices of the characteristic energy scale Q^2 [62]. The gluon distribution is chosen as CTEQ5L and the running α_s is in leading order. The choice of Q^2 is: solid line $Q^2 = \hat{s}/4$; dotted line $Q^2 = p_T^2 + M_{B_c}^2$; dashed line $Q^2 = \hat{s}$ and dash-dot line $Q^2 = p_T^2 + m_b^2$. The lower (upper) three lines corresponding to the distributions at Tevatron (LHC).

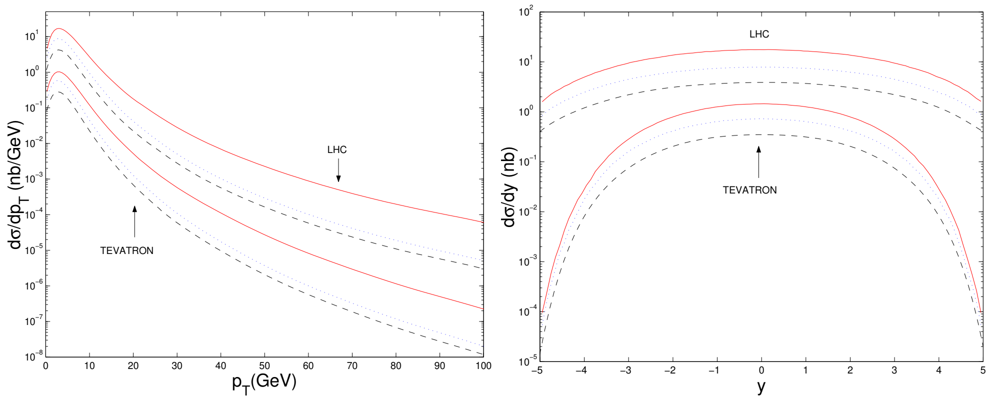

Figure 1.10: B_c^+ differential distributions versus its transverse momentum p_T and rapidity y for different running α_s [62]. The gluon distribution of CTEQ5L and the characteristic energy scale $Q^2 = \hat{s}/4$, are used here. The solid line stands for the constant $\alpha_s = 0.22$, the dotted line for the leading order running α_s and the dashed line for the next leading order running α_s. The lower (upper) four lines correspond to the distributions in Tevatron (LHC).

Comparison between the Mechanisms of Gluon-Gluon Fusion and Quark-Antiquark Annihilation

In this subsection, a brief comparison between the mechanisms of gluon-gluon fusion and quark-antiquark annihilation is discussed. Since, in hadron such as p, $\bar{p}$, π, $\cdots$, the PDFs of heavy quarks are very small throughout the active region $\mid x_i \mid \leq 1$, it is sufficient to take into account only the light quark pair (u-$\bar{u}$, d-$\bar{d}$ and s-$\bar{s}$) annihilations.

The comparative results for the gluon-gluon fusion and the quark-antiquark annihilation mechanisms are shown in Figure 1.11 [62]. From the figure, the gluon-gluon fusion mechanism is dominant over the quark-antiquark annihilation mechanism at a high energy, such as Tevatron and LHC. For the transverse momentum distributions, at low p_T the contributions from gluon-gluon fusion are greater than those from quark-antiquark annihilation by at least two orders of magnitude for both LHC and Tevatron. For rapidity y distributions, in the $\mid y \mid \simeq 0$ region the contributions from gluon-gluon fusion are greater by two orders of magnitude in both colliders.

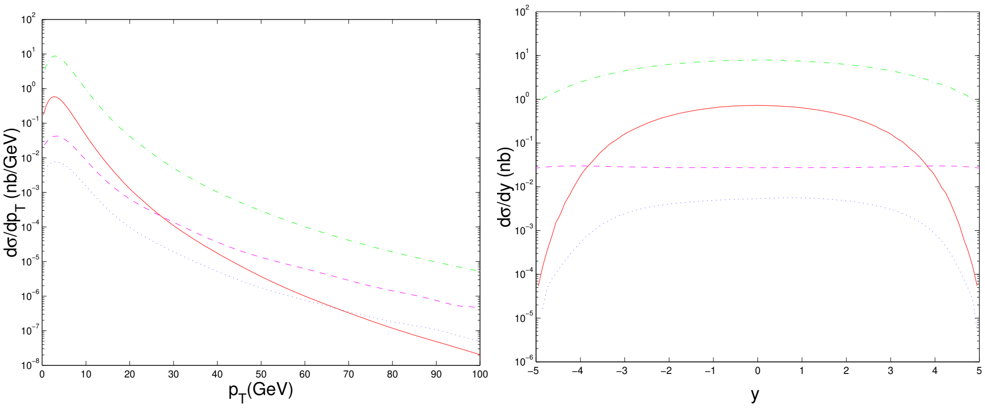

Figure 1.11: B_c^+ distributions versus its transverse-momentum p_T and rapidity y of B_c^+ due to gluon-gluon fusion and quark-antiquark annihilation (the direction of positive y is defined as that of the momentum of the colliding proton) [62]. The PDFs are taken from CTEQ5L, α_s running is set at leading order, and $Q^2 = \hat{s}/4$. The solid lines correspond to gluon-gluon fusion and the dotted lines to quark-antiquark annihilation in Tevatron. The dashed-dotted lines correspond to gluon-gluon fusion and the dashed lines to quark-antiquark annihilation in LHC.

1.5 Outline of this analysis

Using the data of 360 pb^{-1} collected with the CDF II detector, we search for the ground state of $(c\bar{b})$ meson family, B_c^+ meson, in a semileptonic decay mode of $B_c^+ \to J/\psi e^+ \nu_e$, where the J/ψ decays into a $\mu^+\mu^-$ pair. The B_c^+ signal candidates are reconstructed from J/ψ+electron pair with a displaced vertex of three tracks (μ^+, μ^- and an electron) because the J/ψ immediately decays. We start from optimization of the electron identification algorithm by studying the reconstruction efficiency and the fake electron rate using well-identified electron and hadron tracks. Then we estimate the background sizes and shapes with selection criteria optimized for $B^+ \to J/\psi K^+$ reconstruction which has a similar topology to $B_c^+ \to J/\psi e^+ \nu$ and kinematic properties of B_c^+ semileptonic decays. We use data together with Monte Carlo simulation without looking at events in the signal window during the background study. Finally, we open the blinded box and calculate the signal excess over the background with pre-defined selection.

In the following chapters, the experimental setup, event selection and background estimation for the $B_c^+ \to J/\psi e^+ \nu_e$ decay are described. Using the background estimation, we first try to establish the B_c^+ signal. We apply a decay length cut on J/ψ+electron vertex to kill prompt background which cannot be estimated easily. After having established the B_c^+ signal, we release the decay length cut and perform an unbinned likelihood fit to the pseudo-proper decay length of J/ψ+electron pair to extract the B_c^+ meson lifetime.

Chapter 2

Experimental Setup

Fermilab Tevatron Collider represents the high energy frontier in particle physics. It is currently the source of the highest energy proton-antiproton ($p\bar{p}$) collisions. The collisions occur at two points on an underground ring, which has a radius of about 1 km. At these collision points there are two detectors: the Collider Detector at Fermilab (CDF II) and DØ . This analysis uses data collected with the CDF II Detector.

Between 1997 and 2001, both the accelerator complex and the collider detectors underwent major upgrades, mainly aimed at increasing the luminosity of the accelerator, and gathering data samples of 2 fb^{-1} or more. The upgraded machine accelerates 36 bunches of protons and antiprotons, whereas the previous version of the accelerator operated with only 6. Consequently, the time between bunch crossings has been decreased from 3.5 μs for the previous version to 396 ns for the current collider.

The new configuration required detector upgrades at CDF II to ensure a maximum response time shorter than the time between beam crossings. In the following pages, we describe how the proton and antiproton beams are produced, accelerated to their final center of mass energy of 1.96 TeV, and collided. We then describe the components used to identify and measure properties of the particles produced in the collision.

2.1 The Tevatron collider

To create the world's most powerful particle beams, Fermilab uses a series of accelerators. The diagram in Fig. 2.1 shows the paths taken by protons and antiprotons from initial acceleration to collision in the Tevatron.

The Cockcroft-Walton[63] pre-accelerator provides the first stage of acceleration. Inside this device, hydrogen gas is ionized to create H^- ions, which are accelerated to 750 keV of kinetic energy. Next, the H^- ions enter a linear accelerator (Linac)[64], approximately 500 feet long, where they are accelerated to 400 MeV. The acceleration in the Linac is done by a series of

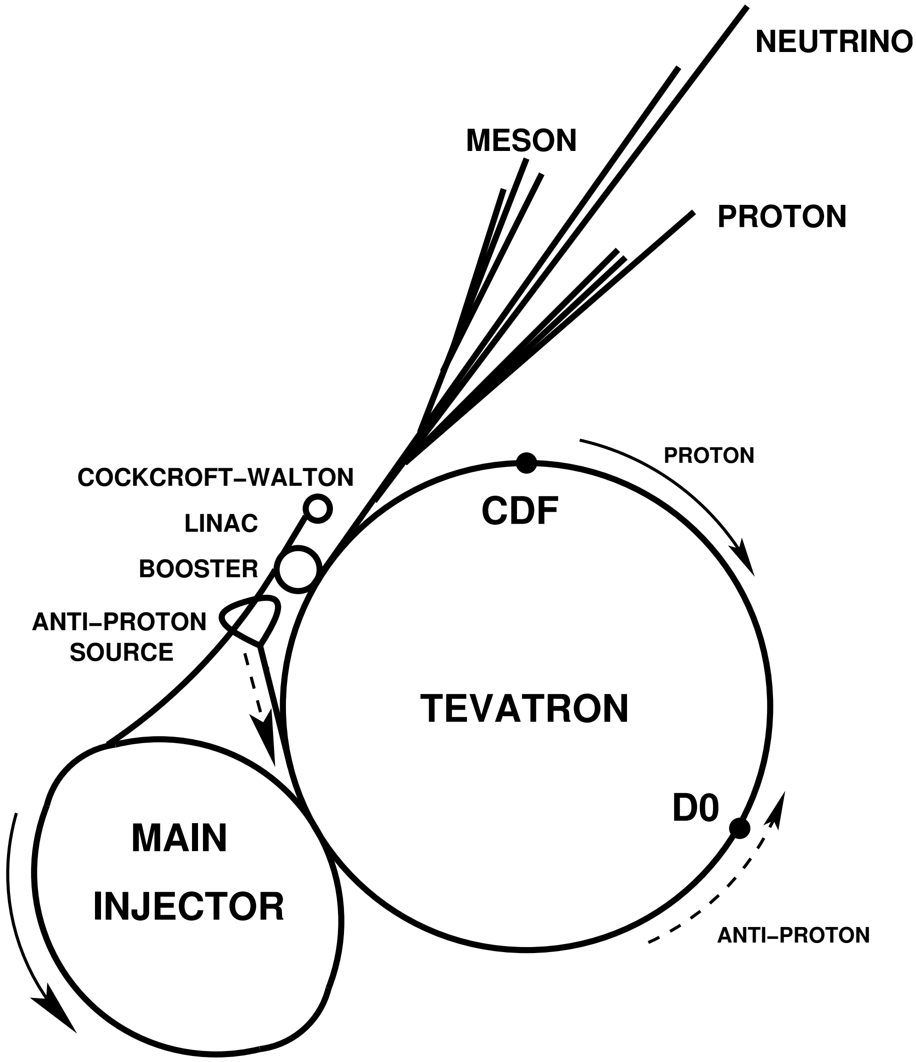

Figure 2.1: Layout of the Fermilab accelerator complex.

"kicks" from Radio Frequency (RF) cavities. The oscillating electric field of the RF cavities groups the ions into bunches.

The 400 MeV H^- ions are then injected into the Booster, a circular synchrotron[64] 74.5 m in diameter. A carbon foil strips the electrons from the H^- ions at injection, leaving bare protons. The intensity of the proton beam is increased by injecting new protons into the same orbit as the circulating ones. The protons are accelerated from 400 MeV to 8 GeV by a series of "kicks" applied by RF cavities. Each turn around the Booster, the protons accrue about 500 keV of kinetic energy.

Protons are extracted from the Booster into the Main Injector [65], which operates at 53 MHz. It has four functions. It accelerates protons from 8 GeV to 150 GeV before injection into the Tevatron, it produces 120 GeV protons which are used for antiproton production, it receives antiprotons from the Antiproton Source and accelerates them to 150 GeV for injection into the Tevatron, and finally, it injects protons and antiprotons into the Tevatron.

The Main Injector replaced the Main Ring accelerator which was situated in the Tevatron tunnel. The Injector is capable of containing larger proton currents than its predecessor, which results in a higher rate of antiproton production. The Main Injector tunnel also houses the Antiproton Recycler. Not all antiprotons in a given store are used up by the collisions. Recycling the unused antiprotons and reusing them in the next store significantly reduces the stacking time. The task of the Antiproton Recycler is to receive antiprotons from a Tevatron store, cool them and re-integrate them into the stack, so that they can be used in the next store.

To produce antiprotons, 120 GeV protons from the Main Injector are directed into a nickel target. In the collisions, about 20 antiprotons are produced per one million protons, with a mean kinetic energy of 8 GeV. The antiprotons are focused by a lithium lens and separated from other particle species by a pulsed magnet.

Before the antiprotons can be used in the narrow beams needed in the collider, the differences in kinetic energy between the different particles need to be reduced. Since this process reduces the spread of the kinetic energy spectrum of the beam, it is referred to as "cooling" the beam. New batches of antiprotons are initially cooled in the Debuncher synchrotron, collected and further cooled using stochastic cooling [66] in the 8 GeV Accumulator synchrotron. The principle of stochastic cooling is to sample a particles motion with a pickup sensor and correct its trajectory later with a kicker magnet. In reality, the pickup sensor samples the average motion of particles in the beam and corrects for the average. Integrated over a long period of time, this manifests itself as a damping force applied onto individual particles which evens out their kinetic energies. It takes between 10 and 20 hours to build up a "stack" of antiprotons which is then used in collisions in the Tevatron. Antiproton availability is the most limiting factor for attaining high luminosities, assuming there are no technical problems with the accelerator (assuming, for example, perfect transfer efficiencies between accelerator subsystems)[64, 65].

Roughly once a day, the stacked antiprotons (36 bunches of about 3×10^{10} antiprotons per

parameter	Run I	Run II
number of bunches (N_B)	6	36
bunch length [m]	0.6	0.37
bunch spacing [ns]	3500	396
protons/bunch (N_p)	2.3×10^{11}	2.7×10^{11}
antiprotons/bunch ($N_{\bar{p}}$)	5.5×10^{10}	3.0×10^{10}
total antiprotons	3.3×10^{11}	1.1×10^{12}
β^* [cm]	35	35
interactions/crossing	2.5	2.3
integrated luminosity [pb^{-1}]	112	450
peak luminosity [cm^{-2}s^{-1}]	2×10^{31}	1.2×10^{32}

Table 2.1: Accelerator parameters for Run I and Run II configurations.

bunch) are injected back into the Main Injector. They are accelerated to 150 GeV together with 36 bunches of roughly 3×10^{11} protons. Both the protons and antiprotons are transferred to the Tevatron.

The Tevatron is the last stage of Fermilab's accelerator chain. It receives 150 GeV protons and antiprotons from the Main Injector and accelerates them to 980 GeV. The protons and antiprotons circle the Tevatron in opposite directions. The beams are brought to collision at two "collision points", B0 and DØ. The two collider detectors, the Collider Detector at Fermilab (CDF II) and DØ , are built around the respective collision points.

The luminosity of collisions can be expressed as:

$$\mathcal{L} = \frac{f N_B N_p N_{\bar{p}}}{2\pi(\sigma_p^2 + \sigma_{\bar{p}}^2)} F\left(\frac{\sigma_l}{\beta^*}\right), \tag{2.1}$$

where f is the revolution frequency, N_B is the number of bunches, $N_{p(\bar{p})}$ is the number of protons(antiprotons) per bunch, and $\sigma_{p(\bar{p})}$ is the protons(antiprotons) rms beam size at the interaction point. F is a form factor which corrects for the bunch shape and depends on the ratio of σ_l, the bunch length to β^*, the beta function, at the interaction point. The beta function is a measure of the beam width, and it is proportional to the beam's x and y extent in phase space.

Table 2.1 shows a comparison of Run I and design Run II [65] accelerator parameters.

2.2 The CDF II detector

The CDF II Detector [67] is a substantial upgrade of the original CDF Detector [68]. It is located at the B0 collision point of the Tevatron Collider. The detector is designed to detect and measure properties of particles emanating from $p\bar{p}$ collisions. The design is not geared

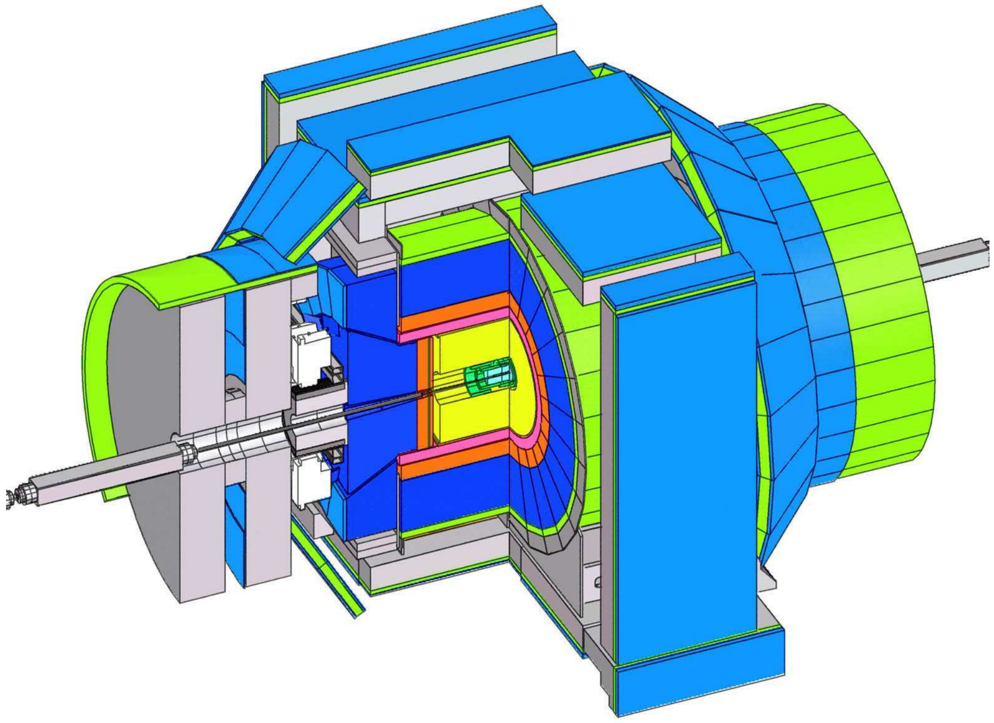

Figure 2.2: The CDF II Detector with quadrant cut to expose the different subdetectors.

toward one particular physics measurement, but rather optimized toward extracting a number of different properties about all particle species created in the $p\bar{p}$ collision. Such particle detectors are often called multi-purpose detectors.

A diagram of the CDF II Detector is shown in Fig. 2.2. A quadrant of the detector is cut out to expose the different subdetectors. The detector subsystems can be grouped as follows. The innermost system is the integrated tracking system. The tracking system is barrel-shaped and consists of cylindrical subsystems which are concentric with the beam. It is designed to detect charged particles, measure their momenta and displacements from the point of collision (primary interaction vertex). The tracking system is surrounded by the Time of Flight system, designed to provide particle identification for low-momentum charged particles. Both the tracking and Time of Flight systems are placed inside a superconducting coil, which generates a 1.4 T solenoidal magnetic field. The coil is surrounded by calorimetry systems, which measure the energy of particles that shower when interacting with matter. The calorimetry systems are surrounded by muon detector systems. When interacting with matter, muons act as "minimally ionizing particles" - they only deposit small amounts of ionization energy in the material. Therefore, they are able to penetrate both the tracking and calorimeter systems. The integrated material of the tracking system, TOF, solenoid and calorimetry systems serves as a particle filter. Particles which penetrate through all that material are mostly muons, and they are detected by leaving tracks in the muon detection system, located outside of the calorimeter.

The most important parts of the detector for this analysis are the tracking system and the trigger, and these will be described in detail in the following sections. The description of the remaining systems will be brief. More detailed information on these systems can be found in the Technical Design Reports of the CDF II Detector [68, 67].

2.3 Standard coordinate system in CDF

Because of its barrel-like detector shape, the CDF II Detector uses a cylindrical coordinate system (r, ϕ, z) with the origin at the center of the detector and the z-axis along the nominal direction of the proton beam. The y-axis points upwards. Since the coordinate system is right-handed, this also defines the direction of the x-axis. Particles moving through a homogeneous solenoidal magnetic field follow helical trajectories. Reconstructed charged particle trajectories are referred to as "tracks". The plane perpendicular to the beam is referred to as the "transverse plane", and the transverse momentum of the track is referred to as p_T. As opposed to e^+e^- collisions, in $p\bar{p}$ collisions not all of the center of mass energy of the $p\bar{p}$ system is absorbed in the collision. The colliding partons inside the proton carry only a fraction of the kinetic energy of the proton. As a result, the center of mass system of the parton collisions is boosted along the beam direction (the "longitudinal" direction) by an unknown amount, but quantities defined in the transverse plane are conserved in the collisions. For instance, the sum of all transverse momenta of particles in a collision is zero, $\sum \vec{p_T} = 0$.

To uniquely parameterize a helix in three dimensions, five parameters are needed. The CDF coordinate system chooses three of these parameters to describe a position, and two more to describe the momentum vector at that position. The three parameters which describe a position describe the point of closest approach of the helix to the beam line. These parameters are d_0, ϕ_0, and z_0, which are the r, ϕ and z cylindrical coordinates of the point of closest approach of the helix to the beam. The momentum vector is described by the track curvature (c) and the angle of the momentum in the $r-z$ plane ($\cot\theta$). From the track curvature we can calculate the transverse momentum. The curvature is signed so that the charge of the particle matches the charge of the curvature. From $\cot\theta$, we can calculate $p_z = p_T \cdot \cot\theta$. At any given point of the helix, the track momentum is a tangent to the helix. This basically means that the angle ϕ_0 implicitly defines the direction of the transverse momentum vector at the point of closest approach, $\vec{p_T}$.

The impact parameter (d_0) of a track is another signed variable; its absolute value corresponds to the distance of closest approach of the track to the beamline. The sign of d_0 is taken to be that of $\hat{p} \times \hat{d} \cdot \hat{z}$, where $\hat{p}$, $\hat{d}$ and $\hat{z}$ are unit vectors in the directions of $\vec{p}$, $\vec{d_0}$ and $\vec{z}$, respectively. An alternate variable that describes the angle between the z-axis and the momentum of the particle is the pseudorapidity η, which is defined as:

$$\eta \equiv -\ln\tan\left(\frac{\theta}{2}\right). \tag{2.2}$$

For decaying particles, we often define the displacement L_{xy},

$$L_{xy} = \vec{d}\cdot\hat{p_T}\ , \tag{2.3}$$

where $\vec{d}$ is the displacement of the decay vertex, and $\hat{p_T}$ is the unit vector in the direction of $\vec{p_T}$.

2.4 Tracking systems

The detector has a cylindrical tracking system immersed in a 1.4 T solenoidal magnetic field for the measurement of charged-particles momenta. We will describe this system starting from the devices closest to the beam and moving outwards. The innermost tracking device is a silicon strip vertex detector, which consists of three subdetectors. A layer of silicon sensors, called Layer 00 (L00) [69], is installed directly onto the beryllium vacuum beam pipe, with the sensors at radii 1.35 and 1.62 cm from the beam. The beam pipe is made of beryllium because this metal has the best mechanical qualities, yet lowest nuclear interaction cross section of all materials.

The layer of silicon on the beam pipe is followed by five concentric layers of silicon sensors (SVX-II) [70] located at radii between 2.45 and 10.6 cm. The Intermediate Silicon Layers (ISL) [71] are the outermost silicon subdetector systems, consisting of one layer at a radius of 22 cm in the central region and two layers at radii 20 and 28 cm in the forward regions. Surrounding the silicon detector is the Central Outer Tracker (COT) [72], a 3.1 m-long cylindrical open-cell drift chamber covering radii from 43.4 to 132.3 cm.

2.4.1 Silicon tracking detectors

Silicon tracking detectors are used to obtain precise position measurements of the path of a charged particle. A silicon tracking detector is fundamentally a reverse-biased p-n junction. When a charged particle passes through the detector material, it causes ionization. In the case of a semiconductor material, this means that electron-hole pairs will be produced. Electrons drift towards the anode, and holes drift toward the cathode, where the charge is gathered. The amount of charge is, to first order, proportional to the path length traversed in the detector material by the charged particle.

By segmenting the p or n side of the junction into "strips" and reading out the charge deposition separately on every strip, we obtain sensitivity to the position of the charged particle. All the CDF II silicon tracking detectors are implemented as microstrip detectors. The typical distance between two strips is about 60 μm. Charge deposition from a single particle passing through the silicon sensor will be read out on one or more strips. This charge deposition is called a "cluster". There are two types of microstrip detectors: single and double-sided. In single-sided

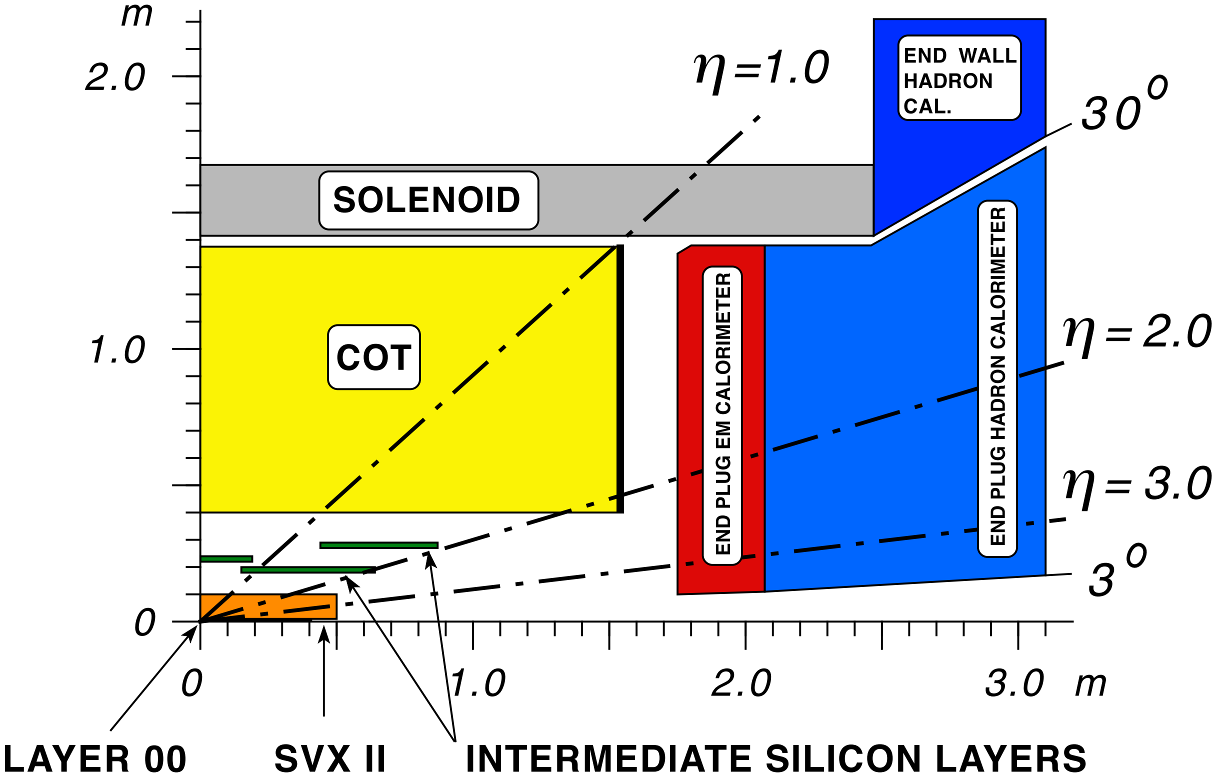

Figure 2.3: The CDF II tracker layout showing the different subdetector systems.

property	Layer 0	Layer 1	Layer 2	Layer 3	Layer 4
number of ϕ strips	256	384	640	768	869
number of z strips	256	576	640	512	869
stereo angle	90°	90°	+1.2°	90°	-1.2°
ϕ strip pitch [μm]	60	62	60	60	65
z strip pitch [μm]	141	125.5	60	141	65
active width [mm]	15.30	23.75	38.34	46.02	58.18
active length [mm]	72.43	72.43	72.38	72.43	72.43

Table 2.2: Relevant parameters for the layout of the sensors of the SVX-II layers.

detectors only one (p) side of the junction is segmented into strips. Double-sided detectors have both sides of the junction segmented into strips. The benefit of double-sided detectors is that while one (p) side has strips parallel to the z direction, providing $r-\phi$ position measurements, the other (n) side can have strips at an angle (stereo angle) with respect to the z direction, which will give z position information.

The innermost layer, L00, is made of single-sided silicon sensors which only provide $r-\phi$ measurements. The SVX-II and ISL are made of double-sided silicon sensors. The ISL detector provides small angle (1.2°) stereo information. As shown in Table 2.2, the SVX-II layers have different stereo angles. Two layers have a 1.2° stereo angle and three have a 90° stereo angle. Four silicon sensors are stacked length-wise into a "ladder" structure which is 29 cm long. The readout electronics are mounted onto the ends of the ladders. The ladders are organized in an approximately cylindrical configuration, creating "barrels". A SVX-II barrel is segmented into 12 wedges, each covering approximately 30° in ϕ with a small overlap at the edges, allowing for several silicon hits per track. There are three SVX-II barrels, adjacent to each other along the z-axis, covering the nominal interaction point in the center of the CDF II Detector. The coverage of the silicon detector subsystems is shown in Fig. 2.4. The silicon tracking system is used in stand-alone mode to provide an extension of tracking down to 2.8 in pseudorapidity.

2.4.2 Central outer tracker

The COT drift chamber provides accurate information in the $r-\phi$ plane for the measurement of transverse momentum, and substantially less accurate information in the $r-z$ plane for the measurement of the z component of the momentum, p_z. The COT contains 96 sense wire layers, which are radially grouped into eight "superlayers", as inferred from the end plate section shown in Fig. 2.5. Each superlayer is divided in ϕ into "supercells", and each supercell has 12 sense wires and a maximum drift distance that is approximately the same for all superlayers. Therefore, the number of supercells in a given superlayer scales approximately with the radius of the superlayer. The entire COT contains 30,240 sense wires. Approximately half the wires run

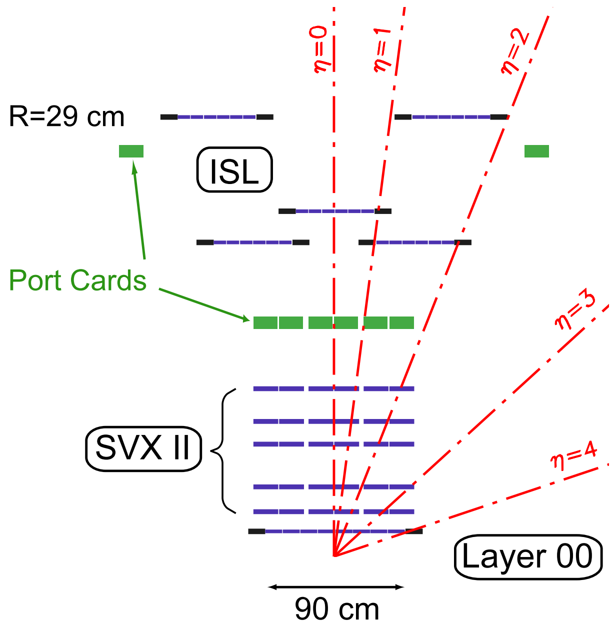

Figure 2.4: Coverage of the different silicon subdetectors projected into the $r-z$ plane. The r and z axes have different scales.

along the z direction ("axial"). The other half are strung at a small angle ($\pm 2^\circ$) with respect to the z direction ("stereo").

The active volume of the COT begins at a radius of 43.4 cm from the nominal beamline and extends out to a radius of 132.3 cm. The chamber is 310 cm long. Particles originating from the interaction point which have $|\eta| < 1$ pass through all 8 superlayers of the COT. Particles which have $|\eta| < 1.3$ pass through 4 or more superlayers.

The supercell layout, shown in Fig. 2.6 for superlayer 2, consists of a wire plane containing sense and potential (for field shaping) wires and a field (or cathode) sheet on either side. Both the sense and potential wires are 40 μm diameter gold plated tungsten. The field sheet is 6.35 μm thick Mylar with vapor-deposited gold on both sides. Each field sheet is shared with the neighboring supercell.

The COT is filled with an Argon-Ethane gas mixture and Isopropyl alcohol (49.5:49.5:1). The mixture is chosen to have a constant drift velocity across the cell width. When a charged particle passes through, the gas is ionized. Electrons drift towards the sense wires. The electric field in a cylindrical system grows exponentially with decreasing radius. As a result, the electric field very close to the sense wire is large, resulting in an avalanche discharge when the charge drifts close to the wire surface. This effect provides a gain of $\sim 10^4$. The maximum electron drift time is approximately 100 ns. Due to the magnetic field that the COT is immersed in, electrons drift at a Lorentz angle of $\sim 35^\circ$. The supercell is tilted by 35° with respect to the

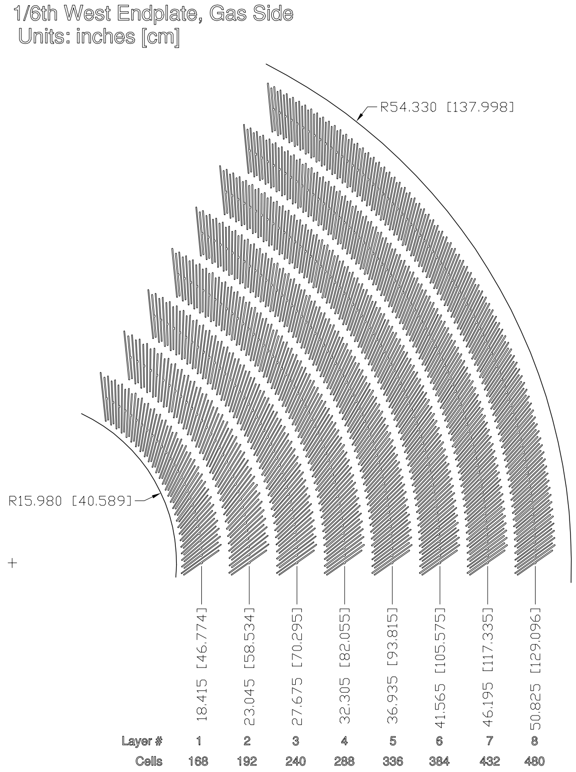

Figure 2.5: Layout of wire planes on a COT endplate.

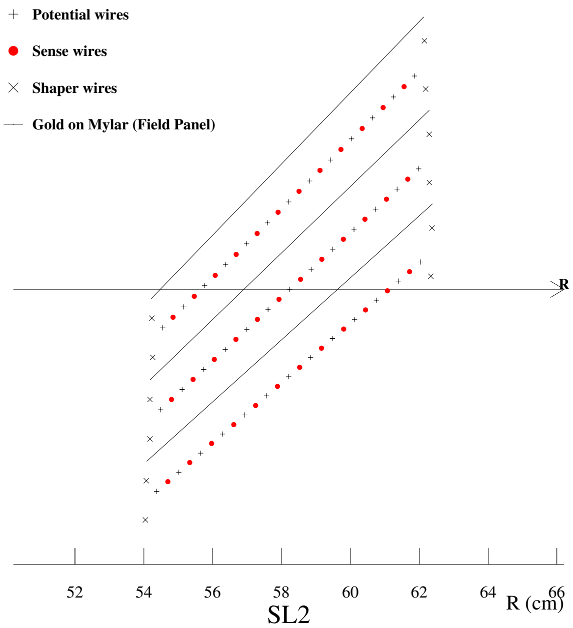

Figure 2.6: Layout of wires in a COT supercell.

radial direction to compensate for this effect.

Signals on the sense wires are processed by the ASDQ (Amplifier, Shaper, Discriminator with charge encoding) chip, which provides input protection, amplification, pulse shaping, baseline restoration, discrimination and charge measurement [73]. The charge measurement is encoded in the width of the discriminator output pulse, and is used for particle identification by measuring the ionization along the trail of the charged particle (dE/dx). The pulse is sent through ~ 11 m of micro-coaxial cable, via repeater cards to Time to Digital Converter (TDC) boards in the collision hall. Hit times are later processed by pattern recognition (tracking) software to form helical tracks. The hit resolution of the COT is about 140 μm. The transverse momentum resolution has been measured using cosmic ray events to be

$$\frac{\sigma_{p_T}}{p_T^2} = 0.0017\ [\mathrm{GeV}/c]^{-1}. \tag{2.4}$$

2.4.3 Pattern recognition algorithms

As explained in the previous sections, charged particles leave small charge depositions as they pass through the tracking system. By following, or "tracking", these depositions, pattern recognition algorithms can reconstruct the charged particle track.

There are several pattern recognition algorithms used to reconstruct tracks in the CDF II tracking system. Most of the tracks are reconstructed using "Outside-In" algorithms which we will describe here. The name of this group of algorithms suggests that the track is followed from the outside of the tracking system inwards.

The track is first reconstructed using only COT information. The COT electronics report hit time and integrated charge for every wire in an event. The hit time corresponds to the time that an avalanche occurred at a sense wire. The hit time can be interpreted as the drift time of the charge in the gas, but first it has to be corrected for time of flight. The hit timing resolution is of the order of a few ns; this roughly corresponds to the average spread in collision times. It is assumed that the collision times always happen at the same time in a cycle during a store. An average of collision times is done for many previous events and this is used as the event collision time. Hit times corrected for the collision time are interpreted as drift times and used in pattern recognition. To perform the final track fit, an additional time of flight correction is performed assuming massless particles.

The helical track, when projected into the two dimensional $r-\phi$ plane, is a circle. This simplifies pattern recognition, so the first step of pattern recognition in the COT looks for circular paths in radial superlayers of the COT. Supercells in the radial superlayers are searched for sets of 4 or more hits that can be fit to a straight line. These sets are called "segments". The straight-line fit for a segment gives sufficient information to extrapolate rough measurements of curvature and ϕ_0. Once segments are found, there are two approaches to track finding. One approach is to link together segments for which the measurements of curvature and ϕ_0 are consistent. The other approach is to improve the curvature and ϕ_0 measurement of a segment reconstructed in superlayer 8 by constraining its circular fit to the beamline, and then adding hits which are consistent with this path. Once a circular path is found in the $r-\phi$ plane, segments and hits in the stereo superlayers are added by their proximity to the circular fit. This results in a three-dimensional track fit. Typically, if one algorithm fails to reconstruct a track, the other algorithm will not. This results in a high track reconstruction efficiency ($\sim$ 95%) in the COT for tracks which pass through all 8 superlayers ($p_T \geq 400$ MeV/c). The track reconstruction efficiency mostly depends on how many tracks there are to be reconstructed in the event. If there are many tracks present close to each other, hits from one track can shadow hits from the other track, resulting in efficiency loss.

Once a track is reconstructed in the COT, it is extrapolated into the SVX-II. Based on the estimated errors on the track parameters, a three-dimensional "road" is formed around the extrapolated track. Starting from the outermost layer, and working inwards, silicon clusters found inside the road are added to the track. As a cluster gets added, the road gets narrowed according to the knowledge of the updated track parameters. Reducing the width of the road reduces the chance of adding a wrong hit to the track, and also reduces computation time. In the first pass of this algorithm, $r-\phi$ clusters are added. In the second pass, clusters with stereo information are added to the track.

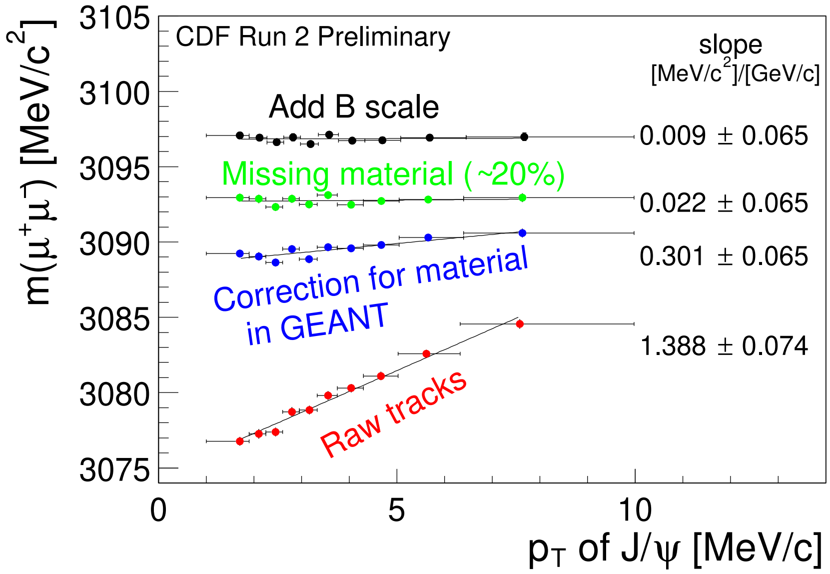

Figure 2.7: Dependence of the reconstructed invariant mass of $J/\psi \to \mu^+\mu^-$ decays on the p_T of the J/ψ.

2.4.4 Momentum scale

As the charged particle traverses through the tracker material, it loses energy. For a track that passes through the entire SVX-II volume, the amount of energy loss is roughly 9 MeV. The value is practically independent of the momentum of the particle. In the reconstructed distribution of invariant mass of $J/\psi \to \mu^+\mu^-$ decays, this effect will be more noticeable for low-momentum J/ψ decays than for high-momentum decays. Fig. 2.7 illustrates this effect. We use the momentum-dependence of the $\mu^+\mu^-$ invariant mass to calibrate the momentum scale of our detector. The J/ψ mass has to be invariant of transverse momentum and match with the world average [9] value if the momentum scale is correctly calibrated. Our calibration procedure follows two steps. First, the momentum dependence of the J/ψ mass is removed by correctly accounting for the energy loss in the tracker material, and then the overall shift of the J/ψ mass is removed by correcting the value of the magnetic field used in the conversion of curvature into transverse momentum.

There are two types of material in the SVX-II tracker. The silicon sensors are read out and therefore called active material. Everything else in the silicon tracker (readout chips, cards, cables, cooling pipes) is passive material. The energy loss in the active material of the tracking system is taken into account by mapping out the material in the GEANT [74] description of our detector. The passive material in the detector description is not complete, so some energy loss is unaccounted for by this method. An additional layer of material is added to the detector description, to correct for the missing material on average. By tuning the amount of missing material, the momentum dependence of the J/ψ mass is removed. The remaining discrepancy with respect to the PDG average is corrected for by scaling the magnetic field. Because of the implementation of this procedure, we can not use it to measure the J/ψ mass, but the results of the calibration process (the amount of missing material and the corresponding magnetic field) can be used to correct the momentum scale in any other measurement. A more detailed description can be found in [75].

2.5 Time of Flight counter

Outside the tracking system, still inside the superconducting magnetic coil, CDF II has a Time of Flight (TOF) [76] system. The TOF system is designed to distinguish low momentum pions, kaons and protons by measuring the time it takes these particles to travel from the primary vertex of the $p\bar{p}$ collision to the TOF system. The system consists of 216 bars of scintillating material, roughly 300 cm in length and with a cross section of 4×4 cm. The bars are arranged into a barrel around the COT cylinder. They are surrounded by the superconducting solenoid on the outside. Particles passing through the scintillating material of the bars deposit energy causing small flashes of visible light. This light is detected by photomultiplier (PMT) tubes which are attached at both ends of each bar. The signal from the photomultiplier tube is processed by a pre-amplifier circuit mounted directly onto the tube. The amplified signal is sent via a twisted pair to the readout electronics in the collision hall. The readout electronics perform both time and amplitude digitization of the signal. The TDC information is a digitization of the time when the signal pulse reaches a fixed discriminator threshold. This time depends on the amplitude of the pulse, since a large pulse crosses the threshold earlier (time walk). The digitization of the pulse amplitude is needed to correct for this effect. After correcting for time walk effects, the timing resolution of the TOF system is currently about 110 ps for particles crossing the bar exactly in front of one of the photomultiplier tubes. The timing resolution varies with displacement from the photomultiplier tube. Large pulses give better timing resolution, and light attenuates while traveling through the scintillator material. Therefore, particles passing through the bar near the photomultiplier tube have better timing resolution than those which are farther away.

2.6 Calorimeters

The main effort of the Run II upgrade of the CDF II central calorimeter system dealt with upgrading the electronics to handle the faster bunch crossings. The active detector parts were taken over from Run I without modification. The plug calorimeter system was completely re-designed and constructed. This system will be described briefly. A detailed description can be

system	η coverage	energy resolution (%)	thickness
CEM	$\|\eta\| < 1.1$	$13.5/\sqrt{E_T} \oplus 3$	$18X_0$
PEM	$1.1 < \|\eta\| < 3.5$	$16/\sqrt{E} \oplus 1$	$21X_0$
CHA	$\|\eta\| < 0.9$	$50/\sqrt{E_T} \oplus 3$	$4.5\lambda_0$
WHA	$0.7 < \|\eta\| < 1.3$	$75/\sqrt{E_T} \oplus 4$	$4.5\lambda_0$
PHA	$1.3 < \|\eta\| < 3.5$	$80/\sqrt{E} \oplus 5$	$7\lambda_0$

Table 2.3: Pseudorapidity coverage, energy resolution and thickness for the different calorimeter subdetectors of the CDF II Detector. The $\oplus$ symbol means that the constant term is added in quadrature to the resolution. λ_0 signifies interaction lengths and X_0 radiation lengths.

found in the CDF II Technical Design Report [68].

The CDF II calorimeter has a "projective tower" geometry. This means that it is segmented in η and ϕ "towers" that point to the interaction region. The coverage of the calorimetry system is 2π in ϕ and $|\eta| < 4.2$ in pseudorapidity. The calorimeter system is divided into three regions: central, plug and forward. Corresponding to these regions, the subsystems will have one of the letters C and P in their acronym. Each calorimeter tower consists of an electromagnetic shower counter followed by a hadron calorimeter. This allows for comparison of the electromagnetic and hadronic energies deposited in each tower, and therefore separation of electrons and photons from hadrons.

There are two subdetectors for the electromagnetic calorimeter: CEM and PEM. These correspond to the central and plug regions of $|\eta|$, respectively. These calorimeters use lead sheets interspersed with scintillator as the active detector medium. The hadron calorimeters in the central region are the central (CHA) and the endwall (WHA). The plug region is covered by the PHA calorimeter. These calorimeters are composed of alternating layers of iron and scintillator. The pseudorapidity coverage, resolutions and thickness for the different electromagnetic and hadron calorimeters are given in Table 2.3.

2.7 Muon systems

Muons are particles which interact with matter only by ionization. For energies relevant to this experiment, they do not cause showers in the electromagnetic or hadronic calorimeters. As a result, if a muon is created in the collision and has enough momentum, it will pass through the calorimeter with minimal interaction with the material inside. Therefore, the calorimeter can be considered as a filter which retains particles that shower when interacting with matter and muons, which do not. Muon detection systems are therefore placed radially outside the calorimeters.

The CDF II Detector has four muon systems: the Central Muon Detector (CMU), the

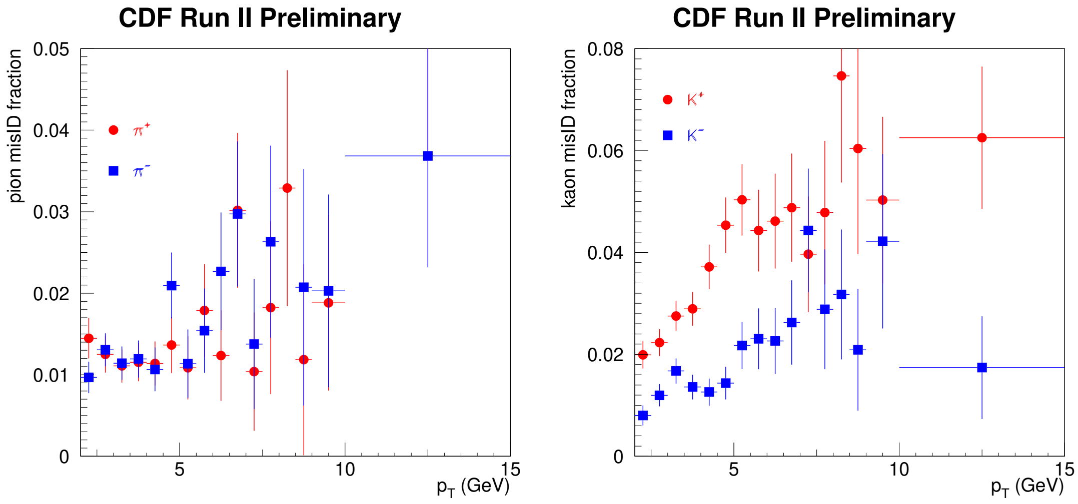

Figure 2.8: Rate of kaon and pion tracks faking muon signals in the CDF II Detector. Roughly 1% of all pions (left) and $2-4\%$ of all kaons (right) will fake a muon signal.

Central Muon Upgrade Detector (CMP), the Central Muon Extension Detector (CMX), and the Intermediate Muon Detector (IMU) [77]. The CMU detector is made of drift cells, and the CMP, CMX detectors are made of drift cells and scintillation counters, which are used to reject background based on timing information. Using the timing information from the drift cells of the muon systems, short tracks (called "stubs") are reconstructed. Tracks reconstructed in the COT are extrapolated to the muon systems. Based on the projected track trajectory in the muon system, the estimated errors on the tracking parameters and the position of the muon stub, a χ^2 value of the track-stub match is computed. To ensure good quality of muons, an upper limit is placed on the value of χ^2_ϕ, the χ^2 of the track-stub match in the ϕ coordinate.

Most of the particles that pass through the calorimeter without showering are muons, but it is also possible for pions or kaons to survive the passage. These particles can then fake muon signals in the muon chambers. Typically, these fake rates are at the percent level, as seen in Fig. 2.8 for the CMU and CMP detectors combined. The Fig. 2.8 shows the rate at which charged pions and kaons fake muon signals in the muon systems. The difference between K^+ and K^- rates comes from the different cross section for interaction of these two mesons with the calorimeter material. The different interaction cross section for these two mesons comes from their quark content: in the K^+, the strange quark is the antiquark.

2.8 Trigger system

Triggering systems are necessary because it is not physically possible to store information about every single $p\bar{p}$ collision. Collisions happen roughly at a rate of 2.5 MHz, and the readout of the full detector produces an event roughly the size of 250 kB. There is no medium available which is capable of recording data this quickly, nor would it be practical to analyze all this data later on. The trigger system is a pre-filter, which reduces data rates and volumes to manageable levels, according to all possible or foreseen physics prescriptions.

The CDF II triggering system is designed based on three conditions. The first condition is that the trigger has to be deadtimeless. This means that the trigger system has to be quick enough to make a decision for every single event, before the next event occurs. The second condition is imposed by the Tevatron upgrade for Run II, and it is the time between collisions, 396 ns. The last condition is that the data logging system can write about 30-50 events per second to tape, because of limited resources. In short, the trigger has to be fast enough to analyze every collision, and it has to figure out which 50 of 2.5 million events it should save in a given second. This is achieved by staging trigger decisions in three levels, as shown in Fig. 2.9.

Each level of the trigger is given a certain amount of time to reach a decision about accepting or rejecting an event. By increasing the time allowed for triggering at different levels of the trigger, the complexity of reconstruction tasks can be increased at every level. At the first level of the trigger, only very rough and quick pattern recognition and filtering algorithms are used. In order to do this in time, the Level 1 and Level 2 triggering mechanisms are implemented with custom electronics. The third level of the trigger is implemented with a PC farm with about 300 CPUs. Using each CPU as an event buffer allows for nearly one second to be allocated for the trigger decision. As a result, nearly offline quality of event reconstruction is available at the third level of triggering. The Level 3 rejection rate is about 10, resulting in 30 events/sec being accepted by the Level 3 trigger and written to tape.

The delay necessary to make a trigger decision is achieved by storing detector readout information in a storage pipeline. At Level 1, for every Tevatron clock cycle, the event is moved up one slot in the pipeline. By the time it reaches the end of the pipeline, the trigger will have reached a decision whether to accept or reject this event. If the event is accepted, its information will be sent to the higher level of the trigger. Otherwise, the event is simply ignored. Since the Level 1 takes up to about 5 μs to reach an accept/reject decision, the front-end electronics is equipped with a 14-event deep buffer to accommodate new events while the Level 1 decision is taken. The accept rate is less than 50 kHz, much smaller than the total input rate of 2.5 MHz. The rejection factor after Level 1 is about 150. The Level 2 trigger takes more time and adds more information to take a further decision about the event. The Level 2 trigger hardware takes less than 30 μs to make the global decision, and with implementation of a set of 4 event buffers the total accept rate is below 300 Hz.

A set of requirements that an event has to fulfill at Level 1, Level 2 and Level 3 constitutes a

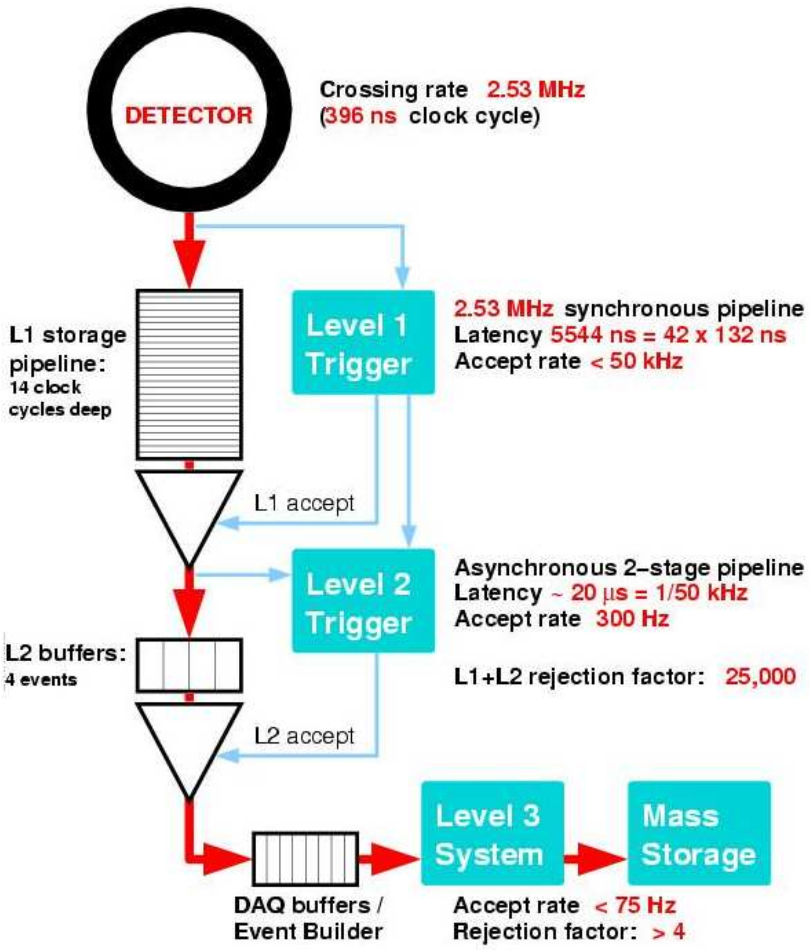

Figure 2.9: Schematic diagram of the CDF global Trigger system.

trigger path. Requiring that an event be accepted through a well defined trigger path eliminates volunteer events. The CDF II trigger system implements about 100 trigger paths. An event will be accepted if it passes the requirements of any one of these paths.

In this thesis three trigger paths have been used, which will be described in detail.

2.8.1 Di-Muon trigger

The first one is oriented to collect a sample rich in J/ψ mesons. It is defined by specific trigger requirements at Level 1 and Level 3. In this data sample, any event which passes the Level 1 J/ψ trigger is automatically accepted by Level 2. To be considered a J/ψ candidate at Level 1, there must be either two muon stubs in the CMU, or one muon stub in the CMU and one in the CMX. The muon stubs must be matched to an XFT (eXtremely Fast Tracker) track [78].

The XTRP [79] extrapolates the XFT tracks into the muon chambers. Taking into account multiple scattering and alignment corrections, a maximum $\delta\phi$ between the track and muon stub is determined. In the CMU, the XFT tracks are required to have $p_T > 1.5$ GeV/c. Stubs in the CMX must match an XFT track with $p_T > 2.0$ GeV/c.

At Level 3, muon pairs are required to have opposite charge. Muon matching requirements are again enforced. The requirement is Δx(track, stub) < 30 cm for CMU muons and Δx(track, stub) < 50 cm for CMX muons. The two muon tracks are required to have $\Delta z < 5$ cm at the point of closest approach to the origin. Finally, for an event to be part of the J/ψ dataset, it is required that $2.7 < M_{\mu\mu} < 4$ GeV/c^2, where $M_{\mu\mu}$ is the invariant mass of the di-muon pair.

2.8.2 8 GeV single electron trigger

In this trigger path, a XFT track with 4 GeV/$c > p_T$ is chosen as an electron candidate and required to have E_T(CEM) > 4 GeV and $E_{\mathrm{HAD}}/E_{\mathrm{EM}} < 0.125$ at Level 1. Then the candidate is prescaled at Level 2. At Level 3, the candidate is required to have $p_T > 8$ GeV/c, E_T(CEM) $>$ 8 GeV, $E_{\mathrm{HAD}}/E_{\mathrm{EM}} < 0.055$, $|\Delta x$(CES cluster, track)$| < 3$ cm, $|\Delta z$(CES cluster, track)$| <$ 5 cm, and LSHR < 0.2. The definition of variable LSHR is

$$\mathrm{LSHR} = 0.14 \sum_i \frac{E_i^{adjacent} - E_i^{expected}}{\sqrt{(0.14\sqrt{E})^2 + (\Delta E_i^{expected})^2}}, \tag{2.5}$$

where the sum is over towers in the electromagnetic cluster, and $E_i^{adjacent}$ and $E_i^{expected}$ are the measured and expected energy in towers adjacent to the seed tower. The expected energy is calculated from the test beam data. $\Delta E_i^{expected}$ denotes and error of the energy estimation.

It is possible to obtain an un-biased electron by finding a partner track associated with this trigger track in physics signatures such as $\gamma \to e^+e^-$, $J/\psi \to e^+e^-$. This trigger path is also useful to study B semileptonic decays.

2.8.3 Hadronic trigger

The other trigger path used in this thesis is the "two-track" trigger path. It is optimized for finding charm and bottom hadrons that decay in hadronic final states. The strategy of the trigger path is as follows. At Level 1, fast measurements of XFT track momenta are available. By cutting on track momenta and angles, most of the inelastic background will be rejected. At Level 2, the additional time available for reconstruction allows to use SVX-II information and obtain better impact parameter measurements of the tracks. Requiring non-zero impact parameters of tracks will imply that they come from decays of long-lived particles: charmed and bottom hadrons.

The Level 1 trigger decision is based on the information from the eXtremely Fast Tracker. This device examines the hit information of the COT in wedges of 15° linking the hits in four

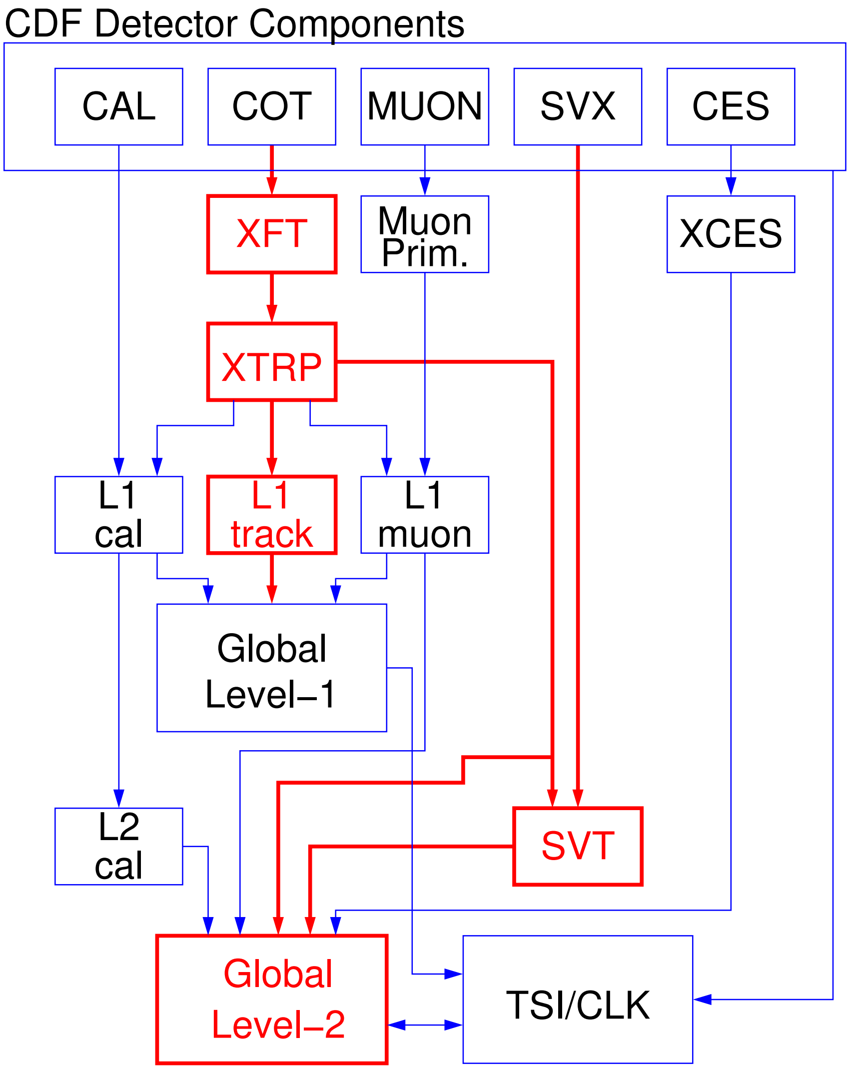

Figure 2.10: Diagram of the different trigger paths at Level 1 and Level 2. The data flow for the track trigger paths is outlined in red.

axial superlayers. It reports the measurement of the track p_T and ϕ_6, the angle of the transverse momentum at the sixth superlayer of the COT, which is located 106 cm radially from the beamline. Based on pre-loaded patterns of COT hits, it is capable of recognizing track segments for tracks with $p_T > 1.5$ GeV/c in 15° wedges of the COT. Two tracks are reported from a given 15° wedge, the two tracks which are closest to the left and right boundaries of a given wedge. As mentioned in Sec. 2.4.3, based on the hit information from a single COT cell, assuming that the track comes from the beamline, a rough measurement of the track p_T and ϕ_6 is obtained. This is the information that the XFT device determines per track. An event is accepted at Level 1 if two tracks are found in the event such that they have opposite charge, both tracks have $p_T > 2$ GeV/c, the scalar sum of transverse momenta $p_{T1} + p_{T2} > 5.5$ GeV/c and the ϕ separation between the tracks at superlayer 6 is $|\Delta\phi_6| < 135°$.

At Level 2 tracking information from the XFT is combined with SVX-II cluster information by the Silicon Vertex Tracker (SVT) [80]. The goal of the second level of the trigger is to obtain a precise measurement of the track d_0, and improved measurements of p_T and ϕ_0.

As mentioned in Sec. 2.4.1, the SVX-II is segmented into 12 wedges in ϕ and three mechanical barrels in z. The SVT makes use of this symmetry and does tracking separately for each wedge and barrel. Tracks which cross wedge and barrel boundaries are only reconstructed under certain circumstances. A SVT track starts with a two dimensional XFT "seed". The XFT measurement is extrapolated into the SVX-II forming a "road". Clusters of charge on the inner four $r-\phi$ layers of the given wedge have to be found inside this road. The silicon cluster information and the XFT segment information are fed into a linearized fitter which returns the measurements of p_T, ϕ_0 and d_0 for the track.

As shown in Fig. 2.11, the width of the Gaussian fit for the distribution of track impact parameters is 47 μm. This width is a combination of the intrinsic impact parameter resolution of the SVT measurement, and the transverse intensity profile of the interaction region. The region profile is roughly circular in the transverse plane and can be approximated by a Gaussian distribution with $\sigma \sim 35$ μm. The intrinsic SVT resolution is obtained by subtracting the beamline width from the width of the d_0 distribution in quadrature. The impact parameter resolution is about 35 μm for tracks with $p_T > 2$ GeV/c. The Level 1 trigger conditions are confirmed with the improved measurements of p_T and ϕ_0. An event passes Level 2 selection if there is a track pair reconstructed in the SVT such that the tracks have opposite charge, each track has $p_T > 2$ GeV/c and 120 μm $< |d_0| <$ 1 mm. The vertex of the track pair has to have $L_{xy} > 200$ μm with respect to the beamline.

The third level of the trigger system is implemented as a PC farm. Every CPU in the farm provides a processing slot for one event. With roughly 300 CPUs, and an input rate of $\sim$ 300 Hz, this allocates approximately 1 second to do event reconstruction and reach a trigger decision.

Fig. 2.12 shows the implementation of the Level 3 farm. The detector readout from the Level 2 buffers is received via an Asynchronous Transfer Mode (ATM) switch and distributed

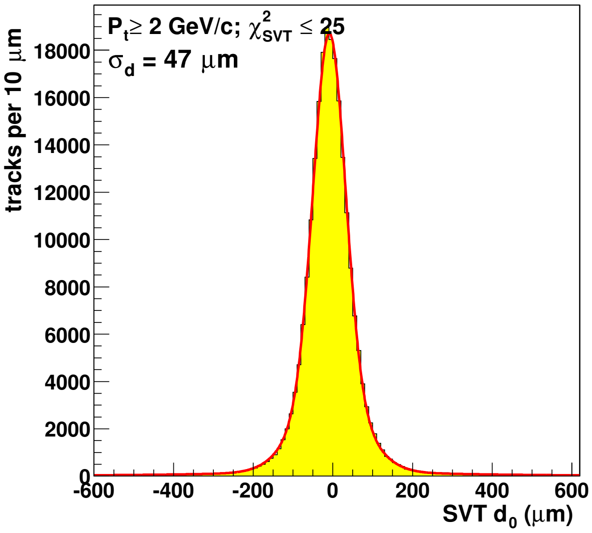

Figure 2.11: SVT impact parameter resolution.

to 16 "converter" node PCs , shown in Fig. 2.12 in green. The main task of these nodes is to assemble all the pieces of the same event as they are delivered from different subdetector systems through the ATM switch. The event is then passed via an Ethernet connection to a "processor" node, which there are about 150 in the farm and are shown in Fig. 2.12. Each processor node is a separate dual-processor PC. Each of the two CPUs on the node process a single event at a time. The Level 3 decision is based on near-final quality reconstruction performed by a "filter" executable. If the executable decides to accept an event, it is then passed to the "output" nodes of the farm. These nodes send the event onward to the Consumer Server / Data Logger (CSL) system for storage first on disk, and later on tape.

For most of the data used in this thesis, full COT tracking has been used to reconstruct tracks. The measurements of p_T, z_0, ϕ_0 and $\cot\theta$ from the COT are combined with the d_0 measurement from the SVT to create a further improved track. The Level 1 and Level 2 trigger conditions (including the requirement on the two-track vertex L_{xy}) are repeated at Level 3 using improved track measurements. For later data full SVX-II tracking is available, and the trigger conditions are repeated using a combined COT/SVX-II fit of the track helices.

2.9 Luminosity measurement

At hadron collider experiments the beam luminosity can be measured using the process of inelastic $p\bar{p}$ scattering. It has a large cross section, $\sigma_{in} \sim 60$ mb. The rate of inelastic $p\bar{p}$ interactions is given by:

$$\mu \cdot f_{bc} = \sigma_{in} \cdot L\,, \tag{2.6}$$

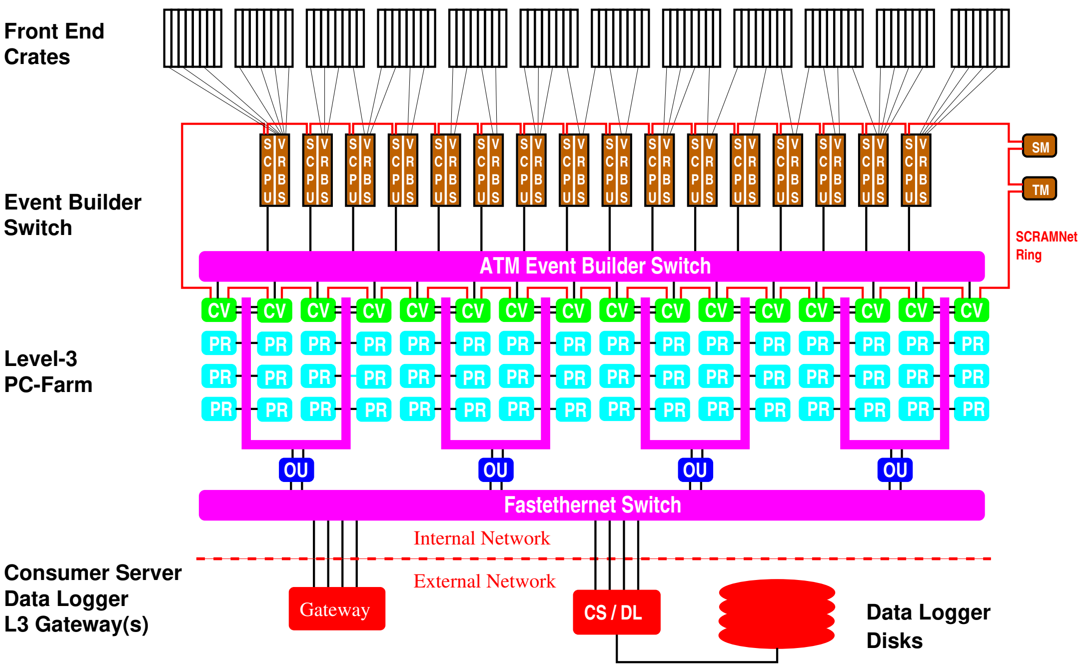

Figure 2.12: Principle of Event Building and Level 3 Filtering. Data from the front end crates is prepared by Scanner CPUs (SCPU) and fed into the ATM switch. On the other side of the switch, converter nodes (CV) assemble events and pass them to processor nodes (PR). Accepted events are passed to output nodes (OU) which send them to the Consumer Server and Data Logging systems (CS/DL).

where L is the instantaneous luminosity, f_{bc} is the rate of bunch crossings in the Tevatron and μ is the average number of $p\bar{p}$ interactions per bunch crossing.

To detect inelastic $p\bar{p}$ events efficiently a dedicated detector at small angles, operating at high rate and occupancy, is required. The Cherenkov Luminosity Counters (CLC) are being used by CDF to measure the Tevatron luminosity. The CLC is designed to measure μ accurately (within a few percent) all the way up to the high luminosity regime $L \sim 2 \times 10^{32}$ cm^{-2}s^{-1}. The CLC is one of the upgrades of the CDF II Detector. It provides an improved measurement of the luminosity with respect to the Run I device. The luminosity measured by the CLC is used to monitor the Tevatron's performance. The CLC modules and the luminosity measurement method are described in detail in [81].

There are two CLC modules in the CDF detector, installed at small angles in the proton (East) and antiproton (West) directions with pseudorapidity coverage between 3.75 and 4.75. Each module consists of 48 thin, long, gas-filled, Cherenkov counters. The counters are arranged around the beam pipe in three concentric layers, with 16 counters each, and pointing to the center of the interaction region. The cones in the two outer layers are about 180 cm long and the inner layer counters (closer to the beam pipe) have a length of 110 cm. The Cherenkov light is detected with fast, 2.5 cm diameter, photomultiplier tubes. The tubes have a concave-convex, 1 mm thick, quartz window for efficient collection of the ultraviolet part of Cherenkov spectra and operate at a gain of 2×10^5.

The counters are mounted inside a thin pressure vessel made of aluminum and filled with isobutane. The Cherenkov angle is 3.1° and the momentum threshold for light emission is 9.3 MeV/c for electrons and 2.6 GeV/c for pions.

The number of $p\bar{p}$ interactions in a bunch crossing follows Poisson statistics with mean μ, where the probability of empty crossings is given by $P_0(\mu) = e^{-\mu}$. An empty crossing is observed when there are fewer than two tubes with signals above threshold in either module of the CLC. The measured fraction of empty bunch crossings is corrected for the CLC acceptance and the value of μ is calculated. The measured value of μ is combined with the inelastic $p\bar{p}$ cross section to determine the instantaneous luminosity.

Chapter 3

Data Set and Event Selection

3.1 Data samples

The J/ψ samples collected using di-muon triggers are used for the reconstruction of $B_c^+ \rightarrow J/\psi e^+ \nu_e$ and $B^+ \rightarrow J/\psi K^+$ which is used for several normalizations. In specific, events from "good runs" in dataset are used, where the "good run" definition follows the recommendation of the B-group [82]. The total integrated luminosity for the sample is 360 pb^{-1}. Figure 3.1 shows the di-muon invariant mass distributions obtained from all of CDF di-muon triggers.

For electron identification studies, we also reconstruct $\gamma \rightarrow e^+e^-$, $J/\psi \rightarrow e^+e^-$ from the 8 GeV single electron-triggered sample and $K_S^0 \rightarrow \pi^+\pi^-$, $D^0 \rightarrow K^-\pi^+$ (also including that from $D^{+*} \rightarrow D^0\pi^+$) and $\Lambda^0 \rightarrow p\pi^-$ from the 2-track trigger sample. The "good runs" are also used for those samples.

3.2 Track selection

The track selection starts with the "defTrack" collection in an event, which already passed through CDF standard selection criteria with very high efficiency. Additional criteria is applied to choose better measured tracks. The quality of the tracks is required to have at least 20 COT axial and 16 COT stereo hits, and have r-ϕ hits from at least 3 SVX-II hits. The COT covariance matrix scaling and magnetic field calibration are made. During the correction, the energy loss correction procedure is also performed by re-fitting the tracks. Silicon hits from L00 are dropped before the track refitting. Tracks used in all decay channels used in this analysis are required to pass these selection criteria.

3.3 J/ψ reconstruction

J/ψ is reconstructed using decay $J/\psi \rightarrow \mu^+\mu^-$. Both muon tracks are required to pass CDF standard muon selection criteria. In addition to the default reconstruction criteria, muons are

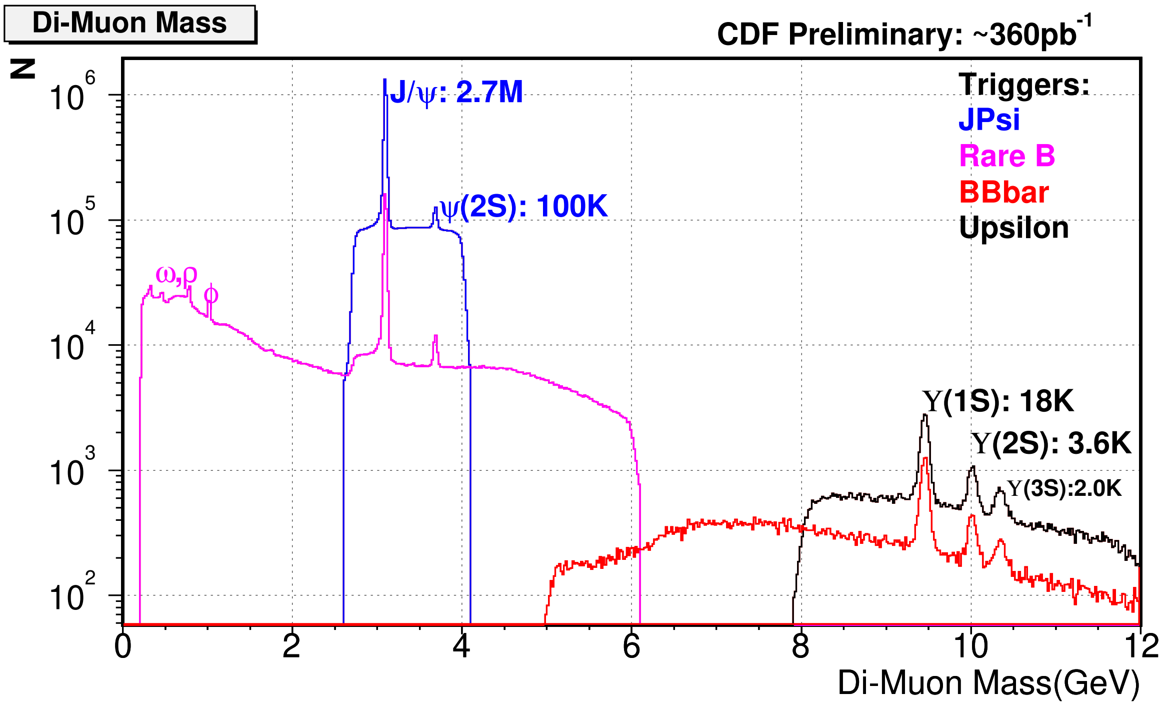

Figure 3.1: Invariant di-muon mass distribution for CDF di-muon triggers.

required to be CMU or CMX muons with a track-stub matching quality of $\chi^2(\Delta\phi) < 9$ between the positions measured using the muon chamber hits and that projected from the associated COT track. The minimum p_T requirement is 1.5 GeV/c for CMU muon and 2.0 GeV/c for CMX muon. To follow the J/ψ trigger path, we require that at least one of the muons in the pair as a CMU muon. The muons are required to satisfy the track selection criteria described earlier. To further reduce the background, muons are also required to have at least 0.1 GeV energy deposited in hadronic calorimeter. This cut reduces about 16% background while keeping more than 97% good J/ψ.

The J/ψ vertex is formed from the intersection of the two muon tracks using the CDF vertex fitting package CTVMFT [83]. The χ^2 of the 3D vertex fitting is required to be less than 15. The momentum of the muon track is adjusted assuming its production point as in J/ψ vertex instead of the primary vertex. The combined p_T of the di-muon pair is required to be greater than 3 GeV/c. The invariant mass of the two muons is then calculated and the pairs with a mass within 50 MeV/c^2 around the PDG value 3.0969 GeV/c^2 [9] are taken as the J/ψ candidates. (The 50 MeV/c^2 window is about 3σ wide. The RMS error σ is about 15 MeV/c^2 obtained from a simple Gaussian fit to the invariant mass.) Di-muons within the 50 MeV/c^2 wide windows around the two masses 10σ away from the peak are used to estimate fake J/ψ background.

3.4 Electron identification

Elecron track is required to have the transverse momentum greater than 2 GeV/c , and the absolute value of the pseudo-rapidity less than 1.0. In order to use the COT specific ionization dE/dx value for the track, the minimum number of COT hits used in the dE/dx calculation is required to be greater than 43 hits.

The electron identification process starts with the soft electron objects reconstructed using a track-based electron-reconstruction algorithm [84, 85]. The algorithm takes a good quality track and extrapolates it to the Central Strip chamber (CES) and the Central Preradiator (CPR). The track is extrapolated as a helix up to the solenoid where CPR is located behind and then as a straight line further to CES. Along the projected trajectory, Central ElectroMagnetic calorimeter (CEM) towers, CES clusters, CPR clusters are sorted and matched to the trajectory to form the electron objects. The matching to the CEM tower is done using η and ϕ positions and a hit tower is required to have a minimal energy of 50 MeV. A 2-tower cluster is formed using the nearest tower in z to the hit tower and the total electromagnetic (EM) energy and hadronic (HAD) energy are calculated from these two towers.

3.4.1 Variables for soft electron objects

The CES fiducial coverage requires that the track hit position within 21 cm in X_{CES} and in between 9 cm - 230 cm in Z_{CES} on the tower center, where X_{CES} and Z_{CES} are the local coordinates of the calorimeter tower in r-ϕ and z views. The CPR fiducial coverage requires that the track hit position within 16 cm in X_{CPR} and in between 8.4 cm - 118 cm and 125 cm - 200 cm in Z_{CPR}. The fiducial coverage is about 85% for CES and 70% for CPR. Electron candidates are required to be in the fiducial coverage of CES but not necessarily in the CPR fiducial. All the CES/CEM related selection cuts will apply to electron candidate but the CPR related selection cuts will apply only if the electron candidate is determined in the CPR fiducial. Below is the list of the variables for the soft electron object.

- $E_{\mathrm{HAD}}/E_{\mathrm{EM}}$

  This is the ratio of the energy measured in the hadronic calorimeters of the Central Hadronic Calorimeter (CHA) and the endWall Hadronic Calorimeter (WHA) to that from the CEM for the two-tower cluster. An real electron has a smaller $E_{\mathrm{HAD}}/E_{\mathrm{EM}}$ value.

- E/p

  This is the ratio of the energy in the EM cluster to the associated track momentum measured in COT. An real electron is to deposit most of its energy in the CEM calorimeter and has the ratio around 1.

- $Q \cdot \Delta X_{\mathrm{CES}}/\sigma_{Q\cdot\Delta X_{\mathrm{CES}}}$

ΔX_{CES} is the distance in the r-ϕ plane between the extrapolated track position and the best-matching CES cluster position. Q is the charge of the track. The measurement error of $Q \cdot \Delta X_{\text{CES}}$ is studied using pure electrons in the conversion sample and parameterized as a function of p_T. The pull distribution, $Q \cdot \Delta X_{\text{CES}}/\sigma_{Q \cdot \Delta X_{\text{CES}}}$, is expected to be between ± 3 for real electrons.

- $\Delta Z_{\text{CES}}/\sigma_{\Delta Z_{\text{CES}}}$

  ΔZ_{CES} is the distance in the r-z plane between the extrapolated track position and the best-matching CES cluster position. The ΔZ_{CES} distribution does not have a charge asymmetry. The measurement error of ΔZ_{CES} is studied using pure electrons in the conversion sample and parameterized as a function of p_T. The pull distribution $\Delta Z_{\text{CES}}/\sigma_{\Delta Z_{\text{CES}}}$ is expected to be within ± 3 for electrons.

- CES shower profile comparison : χ^2_{strip}

  This is the χ^2 comparison of the CES shower profile in the r-z view (by the strip electrodes) with the same profile extracted from test beam electrons. Real electrons are expected to have smaller χ^2_{strip} values.

- CES shower profile comparison : χ^2_{wire}

  This is the χ^2 comparison of the CES shower profile in the r-ϕ view (by the chamber anode wires) with the same profile extracted from test beam electrons. Electrons are expected to have smaller value of χ^2_{wire}.

- CES pulse height : E_{CES}/p^*

  This is the shower energy measured from the 7-wire cluster's pulse height in the unit of GeV scaled by the $p^* = 10 \cdot (p/10)^\alpha$ with $\alpha = 0.85 + 0.15 \cdot e^{-p/15} - p/1000$, where p is the track momentum reference. The value of E_{CES}/p^* for an electron is expected to be approaching 1.

- CES pulse height ratio : $E_{\text{strip}}/E_{\text{wire}}$

  This is ratio of the pulse heights between the r-z measurement of strip and r-ϕ measurement of wire chamber. The electrons tend to have larger value of the ratio while hadrons tend to have smaller ratio.

- CPR cluster energy : E_{CPR}

  The preradiator energy is determined by summing the charges of the 3 CPR wires in the associated CPR cluster. A parameterized correction [84] is done to reduce momentum dependence. The value of E_{CPR} tends to be larger for electrons than for hadrons since electrons lose more energy in the CPR.

- $\Delta X_{\rm CPR}$

  This is the distance in the r-ϕ plane between the extrapolated track position and the best-matching CPR cluster position. A smaller value of $\Delta X_{\rm CPR}$ indicates a good matching.

- dE/dx

  For low momentum electrons, the specific ionization in COT dE/dx is also a very powerful variable to reject hadron fakes. We will discuss the use of dE/dx for electron identification in later section.

- Conversion electron removal

  In most of the B semileptonic decay reconstructions, it is desirable to remove the electrons from photon conversion $\gamma \to e^+e^-$ generated from interaction in the detector material. Electron pair from the photon conversion is identified by using variables of $\Delta \cot \Theta$ and d_{XY}, where $\Delta \cot \Theta$ is simply the difference of track parameter $\cot \Theta$ of the two tracks and the d_{XY} is found by first collapsing the helices of the two tracks into two circles on the r-ϕ plane and then take the distance at the point where the two circles are parallel to each other. In this analysis, electron candidates are to be rejected if a partner track with $p_T > 400$ MeV/c satisfies the conversion criteria $\mid \Delta \cot \Theta \mid < 0.05$ and $-0.3\ cm < d_{XY} < 0.5\ cm$.

- Isolation

  The isolation variable for an electron is defined as the ratio between the scalar sum of p_T for tracks projected into the same EM tower as the the electron track and in a cone of $\Delta R = \sqrt{(\Delta\eta)^2 + (\Delta\phi)^2} < 0.7$ surrounding the electron track to the p_T of the electron track, $I = \sum p_T(i)/p_T(e)$. Electron reconstruction efficiency and fake rate are found to be a function of the isolation variable.

We study these variables using pure electrons reconstructed from photon conversion, $\gamma \to e^+e^-$, and hadrons from $K_S^0 \to \pi^+\pi^-$, $D^0 \to K^-\pi^+$ and $\Lambda^0 \to p\pi^-$.

3.4.2 Likelihood functions for electron identification

Instead of making cuts on each of the electron identification variables, a likelihood function is formed to combine the information of all electron identification variables and the identification is based on the single variable of the combined function.

A likelihood ratio is defined as:

$$\mathcal{L} = \frac{\prod_{i=1}^{10} \mathcal{F}_e(i)}{\prod_{i=1}^{10} \mathcal{F}_e(i) + \prod_{i=1}^{10} \mathcal{F}_h(i)}, \tag{3.1}$$

where $\mathcal{F}_e(i)$ and $\mathcal{F}_h(i)$ are the probability density function distributions of i^{th} selection variables for electrons and hadrons, respectively. There are 10 variables used for the likelihood ratio,

$E_{\rm HAD}/E_{\rm EM}$, E/p, $Q \cdot \Delta X_{\rm CES}/\sigma_{Q \cdot \Delta X_{\rm CES}}$, $\Delta Z_{\rm CES}/\sigma_{\Delta Z_{\rm CES}}$, $\chi^2_{\rm strip}$, $\chi^2_{\rm wire}$, $E_{\rm CES}/p^*$, $E_{\rm strip}/E_{\rm wire}$, $E_{\rm CPR}$ and $\Delta X_{\rm CPR}$. The probability density function templates for kaon tracks are very similar to those for pions. The ones from using protons are slightly different from those from using pions. Since the proton track fraction in CDF events is rather small and the template differences are small, we keep using the pion templates for all hadrons. The distributions of $\mathcal{L}$ for electrons and hadrons obtained from electron tracks in $\gamma \to e^+e^-$ and pion tracks in $K_S \to \pi^+\pi^-$ decays, are shown in Figure 3.2.

The electron identification could be simply a cut on the $\mathcal{L}$ values. But to reduce p_T dependence of election selection efficiency, a new variable $\mathcal{P}_e(\mathcal{L}')$, called normalized cumulative likelihood ratio, is defined as

$$\mathcal{P}_e(\mathcal{L}') = \frac{\int_{\mathcal{L}'}^1 \mathcal{F}_e(\mathcal{L}) d\mathcal{L}}{\int_0^1 \mathcal{F}_e(\mathcal{L}) d\mathcal{L}}, \tag{3.2}$$

where $\mathcal{L}'$ is the likelihood ratio value, $\mathcal{F}_e(\mathcal{L})$ is the probability distribution of $\mathcal{L}$ for electrons. The $\mathcal{P}_e(\mathcal{L}')$ could be understood as the probability to find a larger likelihood ratio value than $\mathcal{L}'$. By definition, $\mathcal{P}_e(\mathcal{L}')$ is the same as the precision on $\mathcal{L}'$ measurement or bin size, and has flat distribution for real electrons. Since the hadron tracks tend to have smaller value of likelihood value, $\mathcal{P}_e(\mathcal{L}')$ tends to be larger for hadrons.

As shown in Figure 3.3, the probability functions for $\mathcal{P}_e$ stays flat for electrons and peaks at larger value for hadrons. A value of $\mathcal{P}_e < 0.7$ is chosen to separate electrons from hadrons. The electron identification efficiency for this cut is found to be around 70% independent of p_T, as shown in Figure 3.7 and tabulated in Table 3.1. This is an expected value of efficiency from the definition of $\mathcal{P}_e$. The fake electron probabilities of charged hadrons are measured by applying the electron selection cuts to the hadron tracks identified by physics signatures of $D^0 \to K^-\pi^+$ and $\Lambda^0 \to p\pi^-$. In Figures 3.4, 3.5 and 3.6, the D^0 and Λ^0 invariant mass distributions are shown for pion, kaon and proton tracks in the CES fiducial before and after applying the electron selection cuts. The fake rate is simply defined as the ratio of fitted D^0 or Λ^0 events before and after passing the $\mathcal{P}_e < 0.7$ cuts. The fake rate are also obtained this way for different track p_T bins. Muon track from $J/\psi \to \mu^+\mu^-$ is also used to measure its ability to fake electron. The probability is found to be very small for a muon to fake electron and we ignore the muon track contribution in the fake electron rate calculation.

Isolation distribution for photon conversion, D^0, and Λ^0 samples are similar to that of the $J/\psi \to \mu\mu$ sample but small differences do exist. To take into account the effect from isolation difference, the events are re-weighted to force them to have similar isolation distributions to $B^+ \to J/\psi K^+$ events during efficiency calculation and to J/ψ+track events during fake rate calculation.

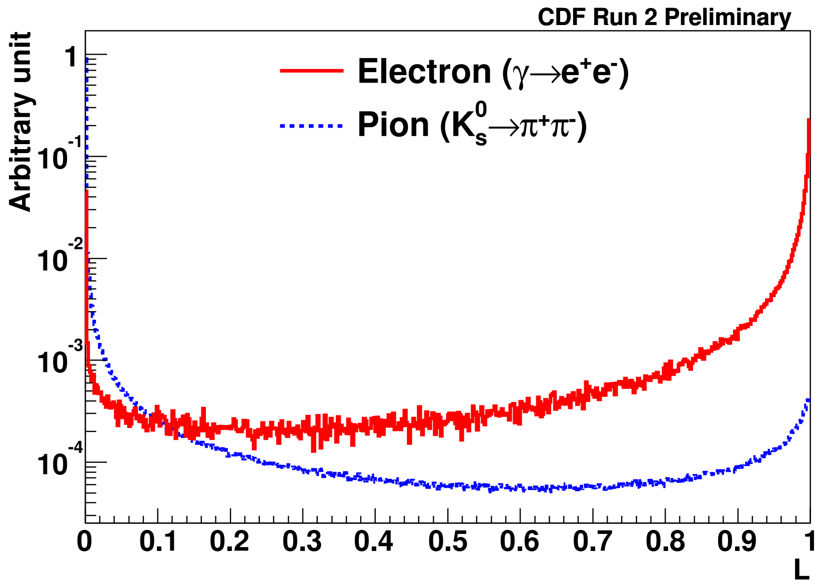

Figure 3.2: Distributions of the likelihood ratio $\mathcal{L}$ for electrons (red, solid lines) and pions (blue, dashed lines).

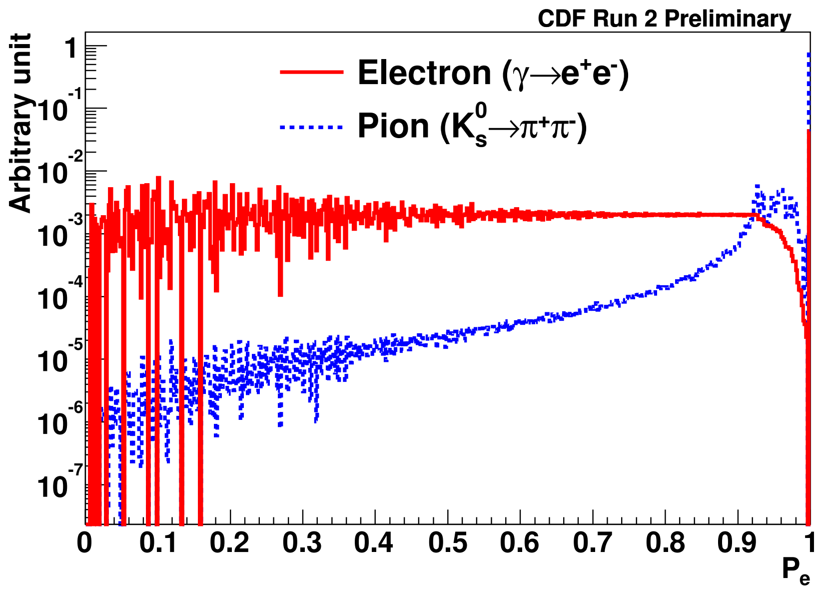

Figure 3.3: Distributions of the cumulative likelihood ratio $\mathcal{P}_e$ for electrons (red, solid lines) and pions (blue, dashed lines). The edge effect in $\mathcal{P}_e$ for electron sample is due to the $E/p > 0.5$ cut during the sample selection for conversion electrons.

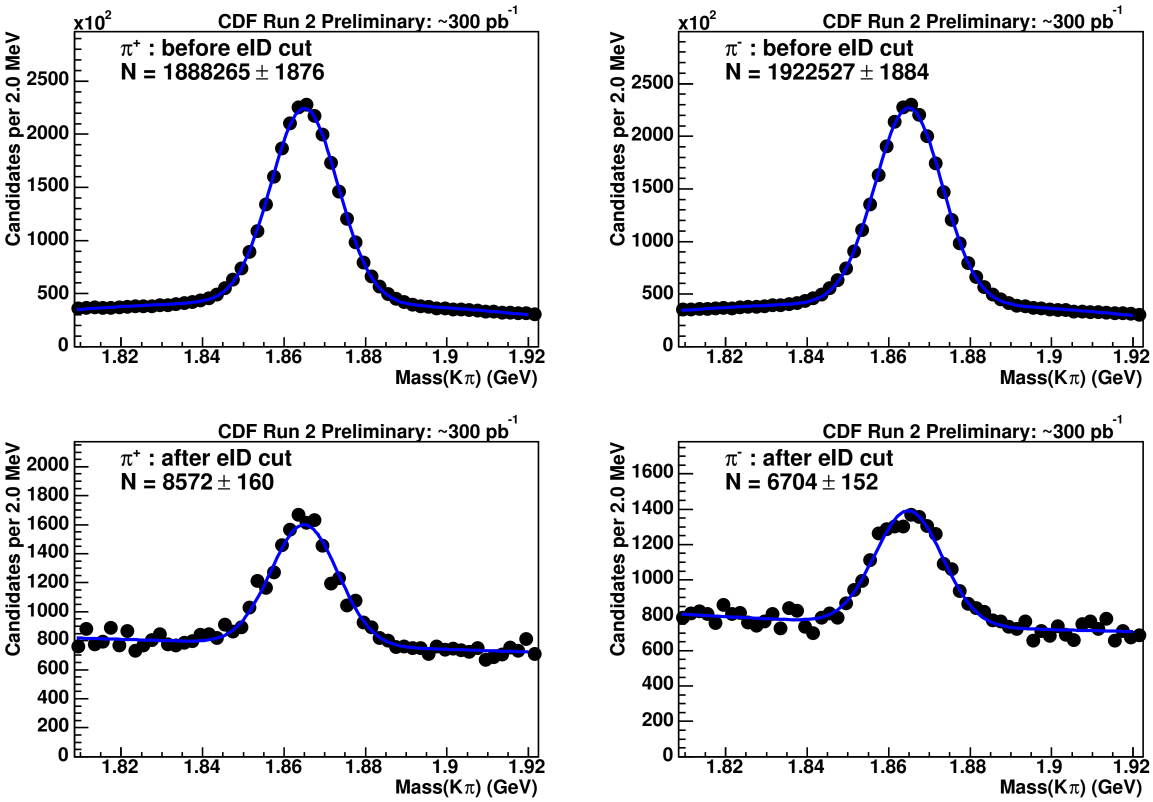

Figure 3.4: D^0 mass distributions for pion tracks in the CES fiducial before (top) and after (bottom) applying the electron selection cut $\mathcal{P}_e < 0.7$. Positively charged tracks are on the left and negatively charged tracks on the right.

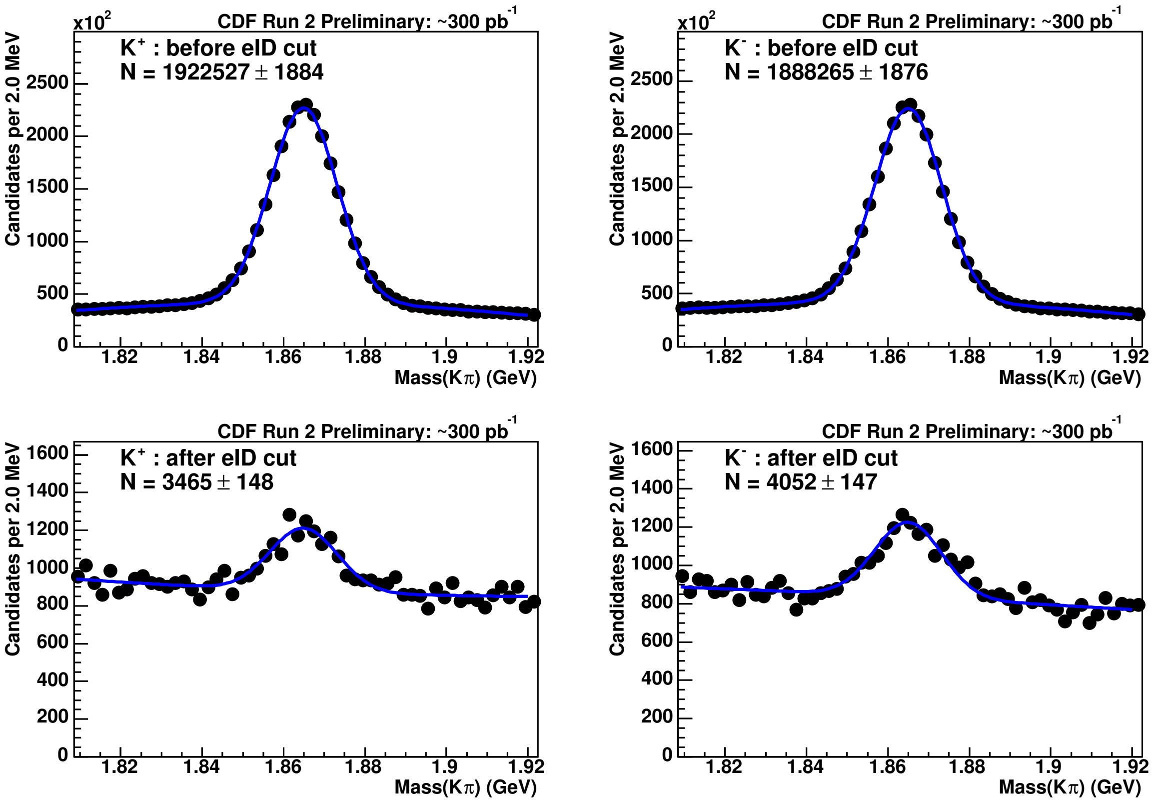

Figure 3.5: D^0 mass distributions for kaon tracks in the CES fiducial before (top) and after (bottom) applying the electron selection cut $\mathcal{P}_e < 0.7$. Positively charged tracks are on the left and negatively charged tracks on the right.

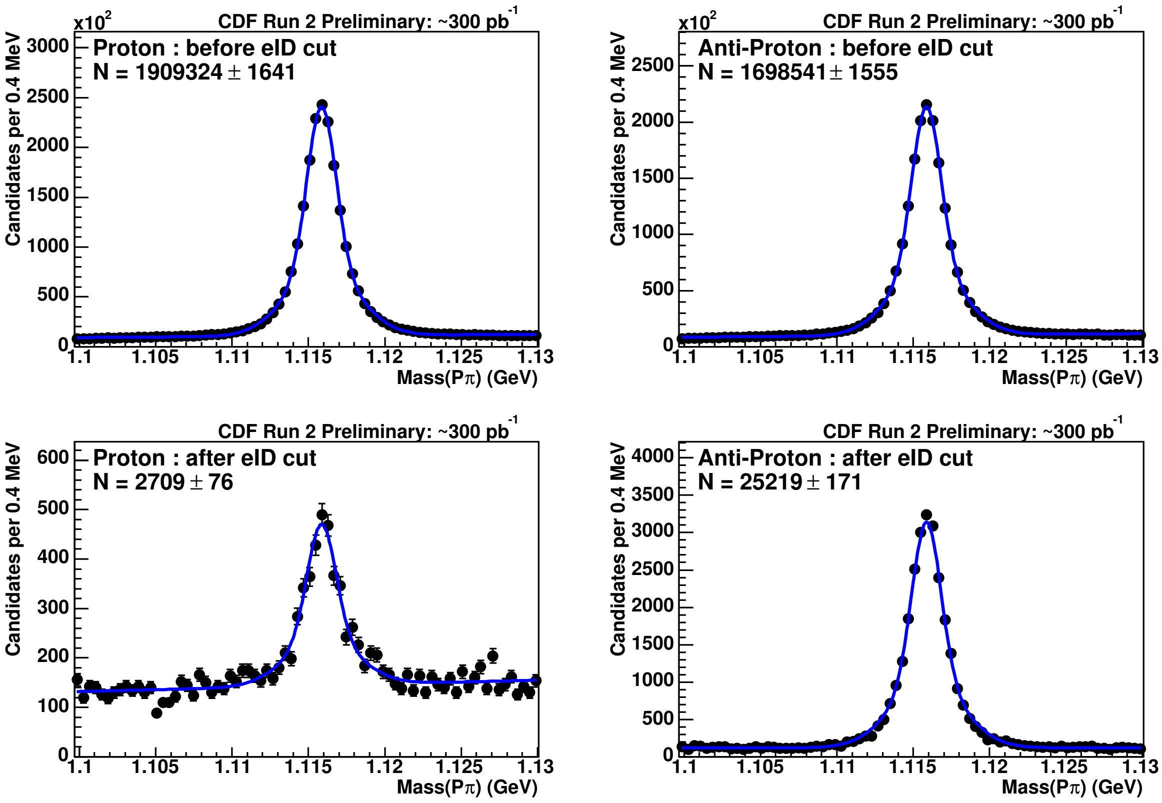

Figure 3.6: Λ^0 mass distributions for proton tracks in the CES fiducial before (top) and after (bottom) applying the electron selection cut $\mathcal{P}_e < 0.7$. Positively charged tracks are on the left and negatively charged tracks on the right.

Table 3.1: Efficiency (%) of likelihood-based electron selection with $\mathcal{P}_e < 0.7$. The events in photon conversion sample are weighted to have similar isolation distribution as of $B^+ \to J/\psi K^+$.

p_T (GeV/c)	$\epsilon(e^+)$	$\epsilon(e^-)$
2-3	68.51 ± 0.34	67.93 ± 0.38
3-4	68.84 ± 0.51	69.47 ± 0.52
4-5	68.89 ± 0.78	69.56 ± 0.70
5-6	68.90 ± 1.05	68.07 ± 1.20
> 6	67.64 ± 1.00	68.52 ± 0.91

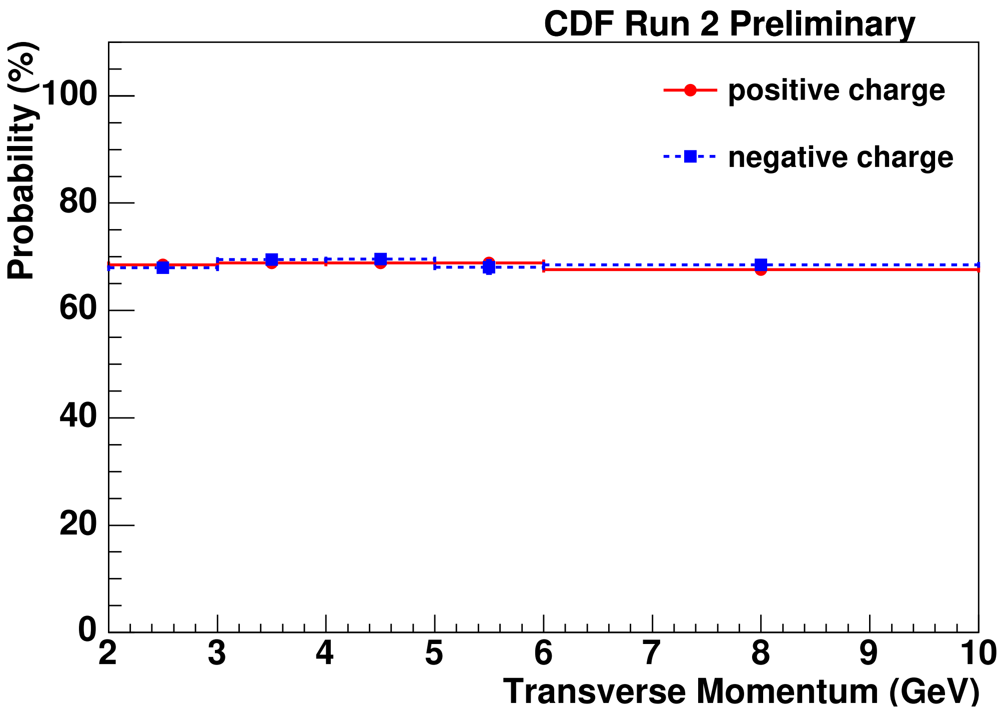

Figure 3.7: Electron identification efficiency using the cumulative likelihood ratio cut $\mathcal{P}_e < 0.7$. The events in photon conversion sample are weighted to have similar isolation distribution as of $B^+ \to J/\psi K^+$.

3.4.3 dE/dx for electron identification

The specific ionization dE/dx in COT is a powerful variable to separate electron tracks from hadron tracks. We use the logarithm ratio between the measured dE/dx value and expected value for electron tracks, called Z_e, to help the electron identification in addition to other variables described in the previous sections.

$$Z_e = \ell n[(dE/dx)_{measured}/(dE/dx)_{predicted}] \tag{3.3}$$

Figure 3.9 shows the pull distribution of Z_e for each charged track. The measurements for positively and negatively charged tracks are found to be consistent and thus are combined. A cut $Z_e/\sigma_{Z_e} > -1.3$ is chosen with high efficiency for electrons while rejecting large fraction of hadronic tracks. The efficiency of this cut as a function of the track momentum is shown in Figure 3.10. The numeric values of the efficiencies are listed in Table 3.2.

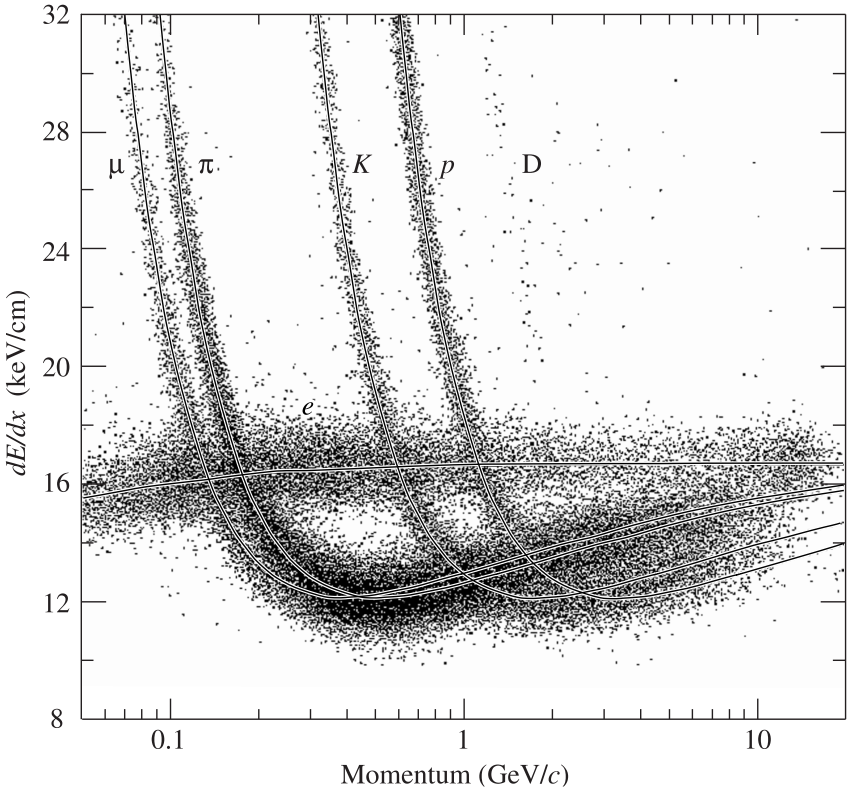

Figure 3.8: dE/dx in the 8.5 atm Ar-CH_4 as a function of the track momentum for several particles [86].

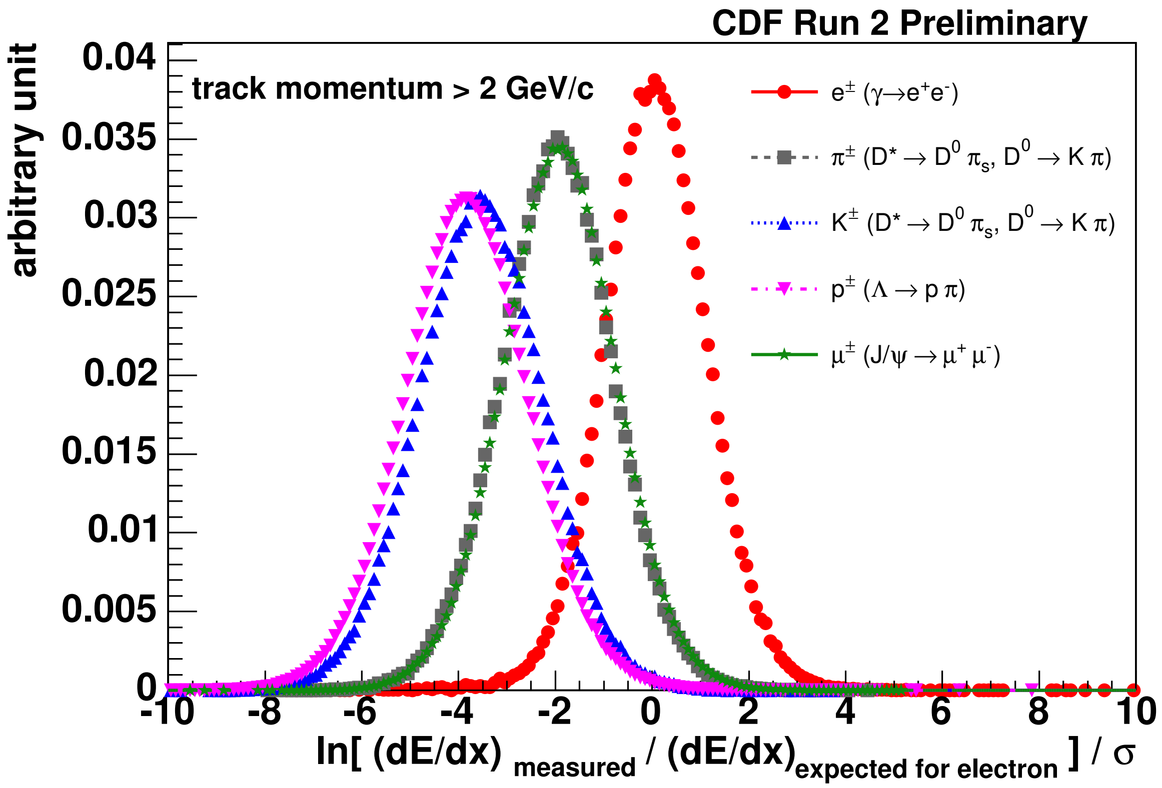

Figure 3.9: Z_e/σ distribution for each charged track

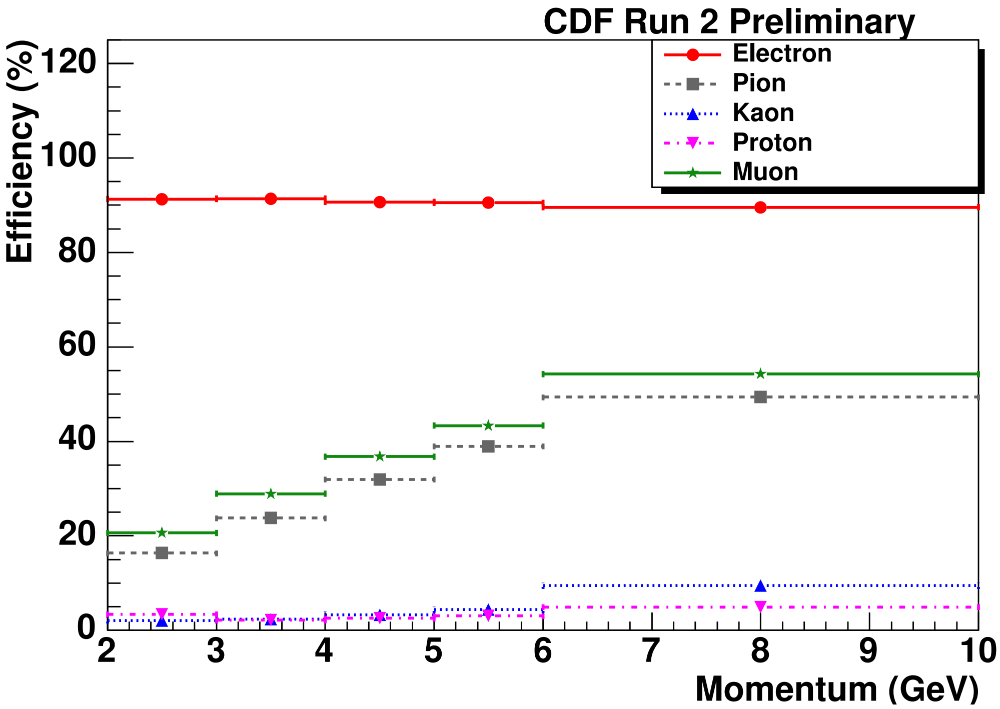

Figure 3.10: Efficiency of $Z_e/\sigma > -1.3$ cut as a function of track momentum for each charged track.

Table 3.2: The efficiency (%) of the dE/dx $Z_e/\sigma > -1.3$ cut as a function of track momentum for electron and hadron tracks.

p (GeV/c)	electron	kaon	proton	pion	muon
2-3	91.30 ± 0.14	2.086 ± 0.088	3.380 ± 0.031	16.369 ± 0.075	20.632 ± 0.092
3-4	91.39 ± 0.15	2.353 ± 0.071	2.138 ± 0.035	23.754 ± 0.098	28.91 ± 0.12
4-5	90.66 ± 0.21	3.288 ± 0.087	2.537 ± 0.070	31.96 ± 0.12	36.77 ± 0.14
5-6	90.52 ± 0.28	4.36 ± 0.12	3.03 ± 0.14	38.95 ± 0.15	43.35 ± 0.17
> 6	89.54 ± 0.20	9.46 ± 0.15	4.91 ± 0.22	49.38 ± 0.16	54.27 ± 0.16

3.5 Event selection for J/ψ-electron pair

The signature of $B_c^+ \to J/\psi e^+ \nu_e$ in CDF is the high p_T J/ψ-electron pairs with a displaced decay vertex and with an invariant mass in the kinematic limits of $m_{J/\psi} < M_{J/\psi e} < m_{B_c}$. A Monte Carlo sample of $B_c^+ \to J/\psi e^+ \nu_e$ decay is generated. The B_c^+ meson momentum spectrum is from a theoretical calculation [62].The mass and lifetime of B_c^+ in the generator are chosen to be 6.271 GeV/c^2 and 0.55 ps, respectively. The mass, p_T and the transverse opening angle $\Delta\phi$ (also called "azimuthal angle") distributions of J/ψ-electron pair from B_c^+ decay in the generator level before and after kinematic cuts on decay products, $p_T(\mu) > 1.5$ GeV/c, $\mid \eta(\mu) \mid < 1.0$, $p_T(e) > 2.0$ GeV/c and $\mid \eta(e) \mid < 1.0$, are shown in Figure 3.12 and Figure 3.11. A cut of $p_T(J/\psi e) > 5$ GeV/c is quite efficient to the signal. For most of the pairs, the opening angle is less than 90 degrees which will be served as an initial cut to reduce $b\bar{b}$ background (see section 4.5). The invariant mass $M_{J/\psi e}$ distribution with kinematic cut on muons, J/ψ and electrons are shown in Figure 3.11. Most of events are in the range of $4 < M_{J/\psi e} < 6$ GeV/c^2 which is defined as our search range for the B_c^+ signal. Increasing the lower mass bound from the 3 GeV/c^2 kinematic limit enhances the rejection (reduces the sensitivity) to fake electron backgrounds from hadrons, conversion decays and feeding-downs from other higher mass states.

Other selection criteria for J/ψ-electron pair is developed based on the experiences of the topologically similar $B^+ \to J/\psi K^+$ reconstruction and generic B semileptonic decay reconstructions. The cuts for the J/ψ-electron selection are summarized in Table 3.3.

Events in a wider window (0-12 GeV/c^2) of J/ψ-electron invariant mass are used to study the shapes of background events and any mis-counting of additional backgrounds. Unlike fully reconstructed B events where the mass resolution is a key to reduce the background, the J/ψ mass constraint is not used for $B_c^+ \to J/\psi e^+\nu_e$ event reconstruction. The mass constraint here does not contribute greatly to the improvement of J/ψ-electron invariant mass resolution and we also need the sideband events on the di-muon pair to estimate the fake J/ψ background. To reduce combinatorial background, we require a higher B vertex fitting quality. The B_c^+ candidates are required to have a displaced vertex L_{xy} which is 3σ away from a primary vertex to reduce the background from prompt J/ψ. In addition, J/ψ-electron pair is removed from the candidate list if the invariant mass of the pair is within 50 MeV/c^2 around the B^+ meson mass of 5.279 GeV/c^2 [9] after assigning a kaon mass to the electron.

After establishing the B_c^+ signal, we release the decay length cut and then measure the B_c^+ meson lifetime.

3.6 Selection of $B^+ \to J/\psi K^+$ events

We also reconstruct B^+ events as our normalization channel. The similar selection cuts as the B_c^+ reconstruction are applied except for the electron identification cut, as listed in Table 3.4. As a normalization mode to the $B_c^+ \to J/\psi e^+\nu_e$, we add the requirement that the kaon track to be in the CEM fiducial. The B vertex and decay length cuts are also modified to be in line to that of the B_c^+ selection. Using these cuts, 2872 ± 59 B^+ events are obtained, as shown in Figure 3.13.

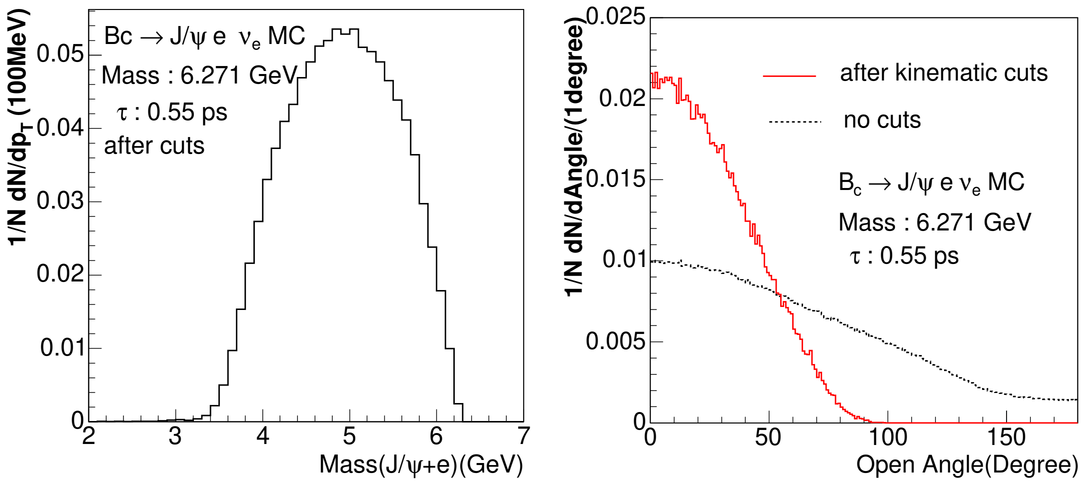

Figure 3.11: Generator level distributions of invariant mass and opening angle of the J/ψ-electron pairs for events from $B_c^+ \to J/\psi e^+ \nu_e$ decay after application of kinematic cuts on the decay products of B_c^+, $p_T(\mu) > 1.5$ GeV/c, $\mid \eta(\mu) \mid < 1.0$, $p_T(e) > 2.0$ GeV/c and $\mid \eta(e) \mid < 1.0$.

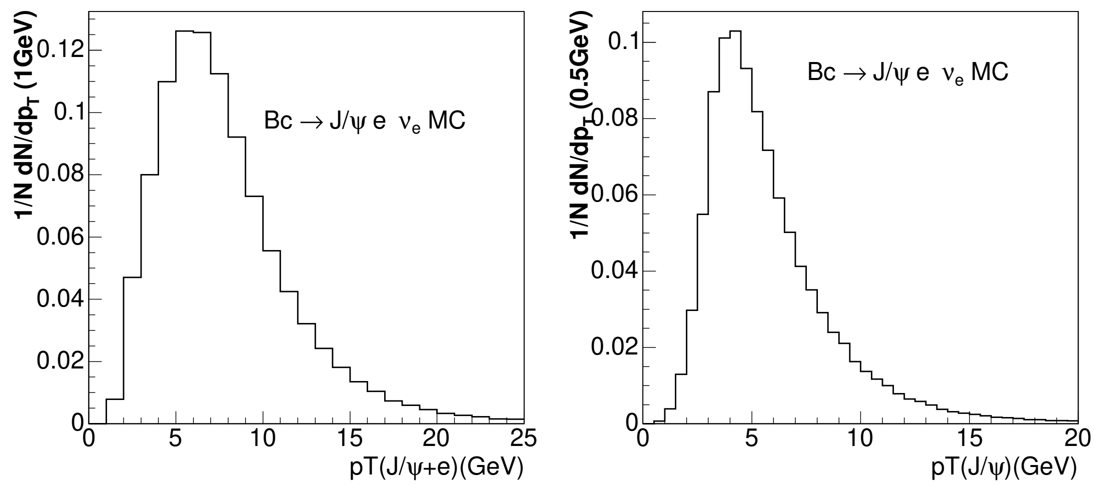

Figure 3.12: Generator level $p_T(J/\psi + e^+)$ and $p_T(J/\psi)$ distributions for events from $B_c^+ \to J/\psi e^+ \nu_e$ decay after application of kinematic cuts on the decay products of B_c^+, $p_T(\mu) > 1.5$ GeV/c, $\mid \eta(\mu) \mid < 1.0$, $p_T(e) > 2.0$ GeV/c and $\mid \eta(e) \mid < 1.0$.

Table 3.3: Event selections for $B_c^+ \to J/\psi e^+ \nu_e$ events.

Cut description	Value
CMU track-stub match	$\chi^2(r\phi) < 9$
CMX track-stub match	$\chi^2(r\phi) < 9$
Hadron energy for muons	$E_{\mathrm{HAD}} > 0.1$ GeV
Di-muon vertex fitting	$\chi^2(3D) < 15$
Di-muon mass window for J/ψ peak	$\mid M(\mu\mu) - 3.09687$ GeV$/c^2 \mid < 50$ MeV$/c^2$
Di-muon mass window for J/ψ sidebands	$\mid M(\mu\mu) - 3.09687 \pm 10 \times 0.015$ GeV$/c^2 \mid < 50$ MeV$/c^2$
p_T of J/ψ	$p_T(J/\psi) > 3$ GeV$/c$
p_T of electron	$p_T(e) > 2$ GeV$/c$
Pseudo-rapidity of electron	$\mid \eta \mid < 1.0$
Electron fiducial	in CEM
dE/dx hits numbers	Nhits ≥ 43
eID by dE/dx	$Z_e/\sigma_{Z_e} > -1.3$
eID by calorimeter	$\mathcal{P}_e < 0.7$
p_T of J/ψ-electron	$p_T(J/\psi e) > 5$ GeV$/c$
$B^+ \to J/\psi K^+$ veto	$\mid M(J/\psi K) - 5.2789$ GeV$/c^2 \mid > 50$ MeV$/c^2$
B vertex quality	$prob(\chi^2_{3d}/1.5, dof) > 0.1\%$
Decay length	$L_{xy}/\sigma_{L_{xy}} > 3$

Table 3.4: Event selections for $B^+ \to J/\psi K^+$ events.

Cut description	Value
CMU track-stub match	$\chi^2(r\phi) < 9$
CMX track-stub match	$\chi^2(r\phi) < 9$
Hadron energy for muons	$E_{\mathrm{HAD}} > 0.1$ GeV
Di-muon vertex fitting	$\chi^2(3D) < 15$
Di-muon mass window	$\mid M(\mu\mu) - 3.09687$ GeV$/c^2 \mid < 50$ MeV$/c^2$
J/ψ mass constraint to PDG value	3.09687 GeV$/c^2$
p_T of J/ψ	$p_T(J/\psi) > 3$ GeV$/c$
p_T of kaon	$p_T(K) > 2$ GeV$/c$
Pseudo-rapidity of kaon	$\mid \eta \mid < 1.0$
dE/dx hits numbers	Nhits ≥ 43
Kaon fiducial	in CEM
p_T of B	$p_T(B^+) > 5$ GeV$/c$
B vertex quality	$prob(\chi^2_{3d}/1.5, dof) > 0.1\%$
Decay length	$L_{xy}/\sigma_{L_{xy}} > 3$

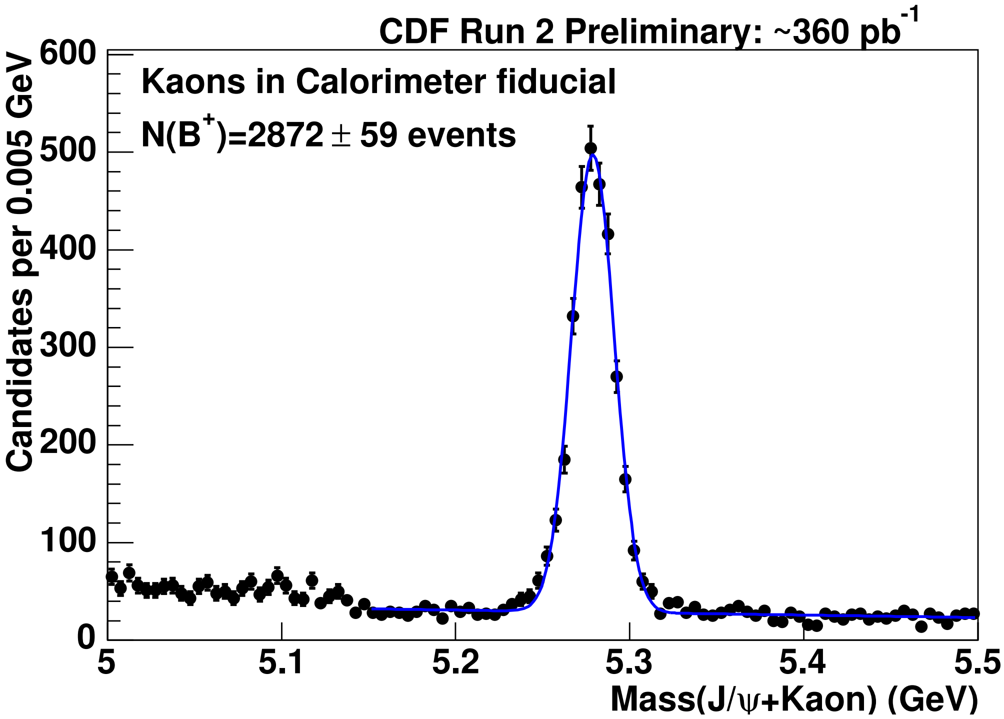

Figure 3.13: B^+ invariant mass distribution. 2872 ± 59 signals are found from a fitting to the distribution.

Chapter 4

Background Estimates

4.1 Fake J/ψ background

The fake J/ψ background is estimated using the sideband events on the J/ψ mass window, $| M(\mu\mu) - 3.09687 \pm 10 \times 0.015$ GeV/c^2 $| < 50$ MeV/c^2. Since our control samples obtained from J/ψ data (J/ψ+track, tagged conversion, and electron events) have fake J/ψ component each other, we exclude J/ψ mass sideband events from those samples in the following estimations to avoid double-counting of the contribution of the fake J/ψ.

4.2 Prompt background

It would be better if we could select the B_c^+ signal events without any cuts depending on the lifetime. However there are a lot of prompt QCD J/ψ events in the J/ψ sample (about 90% of the J/ψ's are prompt J/ψ events). Since it is difficult to estimate the size of the prompt background, we apply a decay length cut, $L_{xy}/\sigma_{L_{xy}} > 3$, on the J/ψ-electron vertex to reduce the prompt J/ψ contribution until the B_c^+ signal events have been confirmed. This cut will be released when we measure the B_c^+ meson lifetime.

4.3 Fake electron background

The fake electron background is estimated using the J/ψ+track data sample. The event selections are similar to that for the J/ψ-electron but there is no requirement for the track to be identified as an electron by the calorimeter information.

Systematic uncertainty on the fake electron background estimation comes from several sources, fake rate dependence on the electron isolation environment, uncertainty of track particle type, and the SVT-track bias.

4.3.1 Dependence on the electron isolation

The electron isolation is one of sources to affect the electron identification. The definition we are using is described in section 3.4.1. After checking isolation distribution for the $D^0 \to K^-\pi^+$ events selected using the 2-track trigger, the sample tends to have more isolated tracks comparing to the J/ψ+track events. We correct the difference by making the isolation distribution in $D^0 \to K^-\pi^+$ similar to that as in J/ψ+track events using an event-by-event weighting method during the fake rate calculation. The difference on fake rates before and after re-weighting is found to be about 15%. We use the weighted fake rate for our estimation of background contribution but take the difference as a systematic uncertainty. The effect from this uncertainty corresponds to 2.24 events in the signal window of $4 < M_{J/\psi e} < 6$ GeV/c^2.

4.3.2 SVT trigger bias

Another source of systematic uncertainty on the fake rate is the potential bias from the trigger difference. The $D^0 \to K^-\pi^+$ sample used for the fake rate measurement is from the 2-track SVT triggered sample, the tracks having a much tighter requirement on the silicon hits than the tracks around J/ψ. The SVT track requires at least 4 silicon hits attached to it. From the distributions of the number of silicon hits, the fraction of tracks with less than 4 hits in the J/ψ sample is much bigger than that from $D^0 \to K^-\pi^+$ sample. We first look at the fake rate difference between tracks with less than 4 hits and the ones with at least 4 hits. The $K_S^0 \to \pi^+\pi^-$ decay reconstructed in the J/ψ sample is used for this study. Due to limited statistics, the fake rates for tracks with different number of silicon hits are calculated only as p_T integrated results. Using the silicon hit distributions in J/ψ+track sample as the weighting factors, the new averaged fake rates are calculated and found to be different by about 7% from those obtained in the original 2-track triggered sample. We take this variation and assign it as a systematic uncertainty. This uncertainty of the background corresponds to 1.11 events in $4 < M_{J/\psi e} < 6$ GeV/c^2.

4.3.3 Dependence on the hadron track type

As discussed in the previous chapter, the fake electron rate is different for pions, kaons and protons. To properly estimate the fake electron background, we calculate the averaged fake rate after taking into account the probabilities for a track to be of a pion, kaon or proton. We obtain this information using PYTHIA Monte Carlo [87]. A generic J/ψ sample from B decays is produced using the PYTHIA setting "msel=1" with "tuning-A" for underlying events [88]. We analyze the Monte Carlo sample in the same way as for the J/ψ+track data to find the track candidates around the J/ψ. The track particle-type is found by matching the reconstructed track with the Monte Carlo track information at generator level. Distributions of particle-type being pion, kaon and proton are then calculated. The dE/dx cut is not reliable for Monte Carlo tracks, so dE/dx efficiencies listed in Table 3.2 are instead used to correct the original particle-type distributions. In Table 4.1, the fractions of particle-type for tracks with different p_T are listed and also plotted in Figure 4.1. With the particle-type fractions in Table 4.1, the fake rate results for the pion, kaon and proton are re-weighted to get the average fake electron rates for a track around J/ψ, as shown in Fig 4.2. The numeric values are listed in Table 4.2

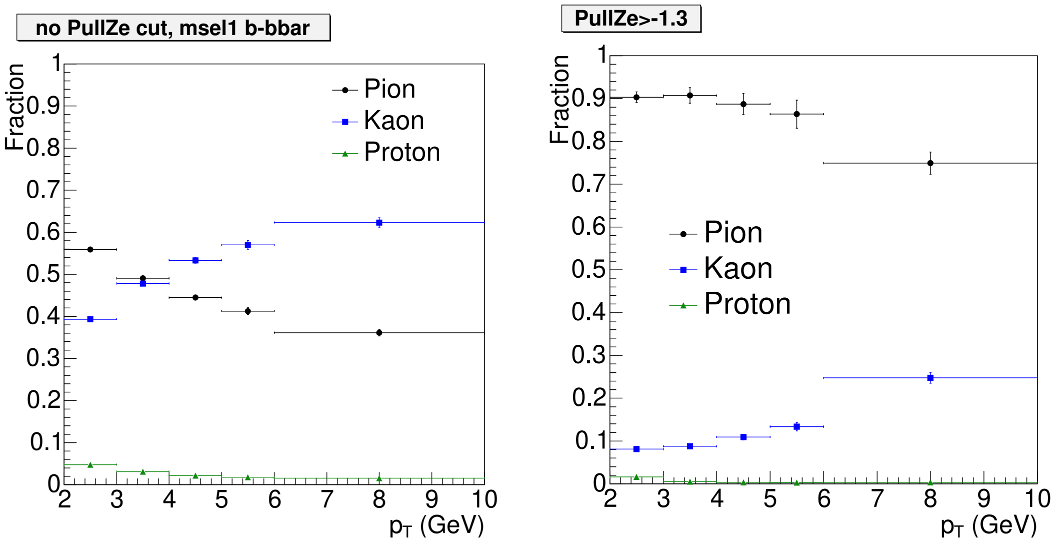

Figure 4.1: Fraction of particle-type for tracks around J/ψ obtained from PYTHIA Monte Carlo before(left) and after(right) applying dE/dx cut efficiency.

Table 4.1: Fraction of particle-type for tracks around J/ψ obtained from PYTHIA Monte Carlo before and after applying dE/dx cut efficiency.

p_T GeV/c	Before dE/dx cut			After dE/dx $Z_e/\sigma_{Z_e} > -1.3$ cut		
	kaon	pion	proton	kaon	pion	proton
2-3	0.393 ± 0.002	0.559 ± 0.003	0.0477 ± 0.0007	0.081 ± 0.003	0.903 ± 0.012	0.0159 ± 0.0012
3-4	0.478 ± 0.004	0.491 ± 0.004	0.0312 ± 0.0009	0.088 ± 0.004	0.907 ± 0.018	0.0052 ± 0.0010
4-5	0.533 ± 0.007	0.445 ± 0.006	0.0218 ± 0.0011	0.109 ± 0.007	0.887 ± 0.024	0.0035 ± 0.0011
5-6	0.570 ± 0.011	0.412 ± 0.008	0.0176 ± 0.0015	0.134 ± 0.010	0.864 ± 0.033	0.0029 ± 0.0014
> 6	0.653 ± 0.011	0.361 ± 0.008	0.0157 ± 0.0014	0.248 ± 0.013	0.749 ± 0.026	0.0032 ± 0.0013

Table 4.2: Averaged fake electron probabilities (%) as function of track p_T after isolation-weighting.

p_T (GeV/c)	positive charged	negative charged
2-3	0.773 ± 0.037	0.640 ± 0.035
3-4	0.371 ± 0.026	0.371 ± 0.023
4-5	0.372 ± 0.032	0.273 ± 0.028
5-6	0.290 ± 0.044	0.250 ± 0.037
> 6	0.134 ± 0.041	0.211 ± 0.042

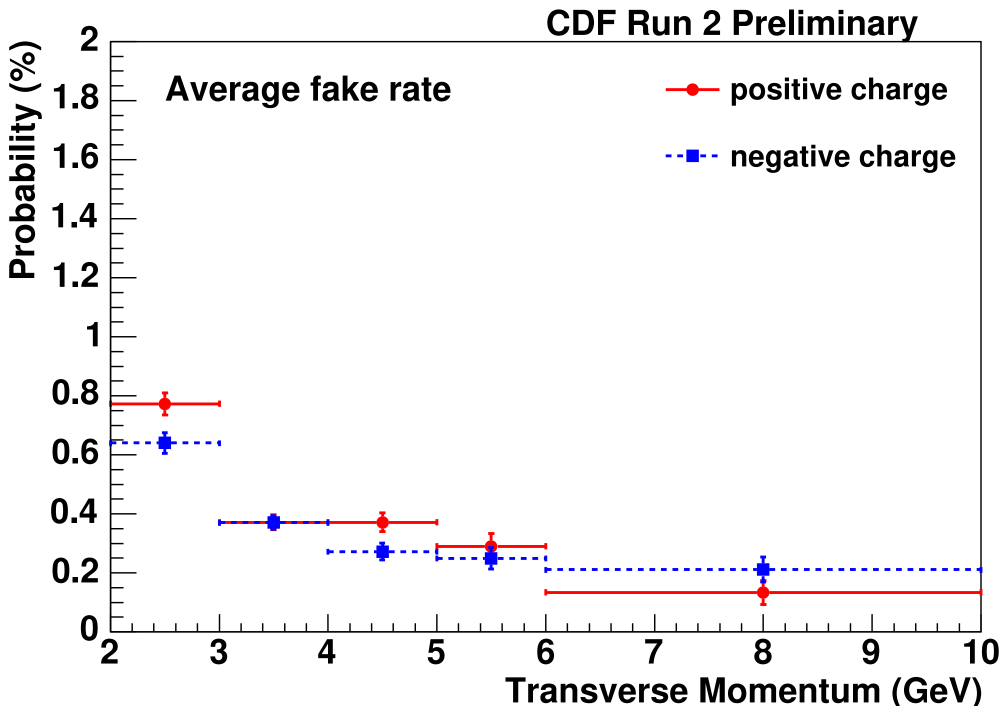

Figure 4.2: The averaged fake electron probabilities as function of track p_T .

The J/ψ+track candidates with the dE/dx cut are multiplied by the averaged fake electron probabilities to obtain the contributions of a fake electron combined with a real J/ψ. The invariant mass distribution for this background is shown in Figure 4.3. The expected number of this background in $4 < M_{J/\psi e} < 6$ GeV/c^2 is 15.43 events

We compare the particle-type fractions predicted from the Monte Carlo and obtained from fitting data using dE/dx values. The dE/dx distribution for kaon and proton particles are similar thus we are only able to separate pions from kaons and protons. So we fit the track used in the J/ψ+track sample to obtain the pion fraction. The shape of the Z_e/σ_{Z_e} for pions and kaons are assumed to be a Gaussian function. We also combine the contribution of protons to of kaons since they are very similar. We simply calculate the pion fraction and it is found that the pion fraction from the fitting is consistent with that predicted from Monte Carlo within 3% accuracy. We take the difference and re-calculate the averaged fake rate and fake background contribution. From this estimation, the uncertainty of the background corresponds to 0.29 events in $4 < M_{J/\psi e} < 6$ GeV/c^2.

We also check the fake electron prediction by comparing it to that evaluated from a dE/dx fitting on the J/ψ-electron sample. The electron track dE/dx distribution is fitted to a sum of

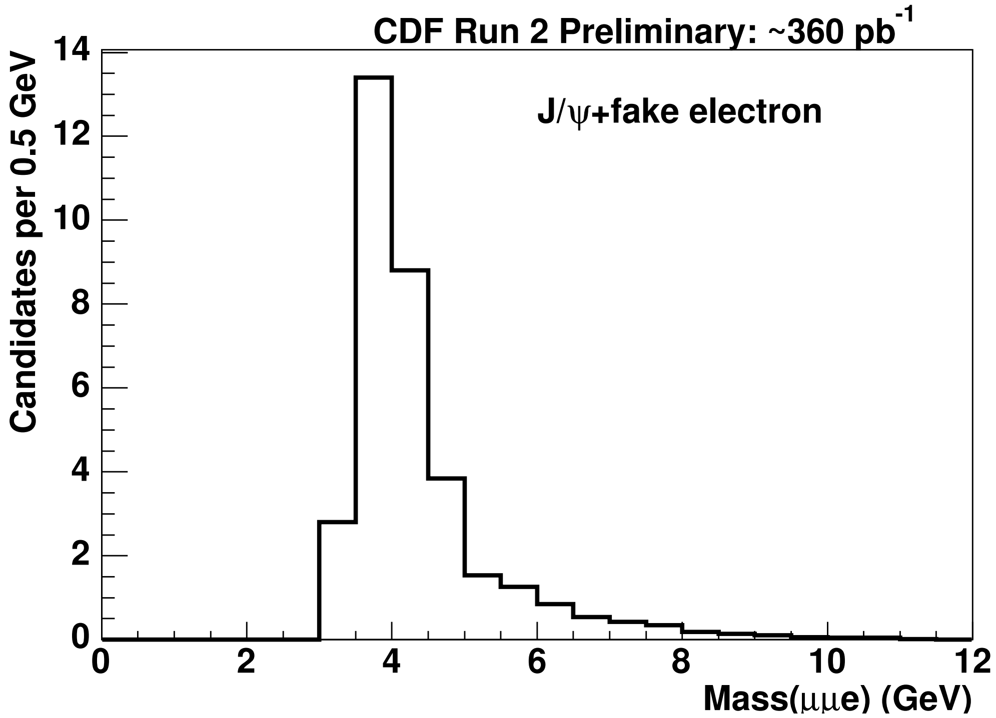

Figure 4.3: Invariant mass distribution of J/ψ+fake electron background. Fake J/ψ contributions are excluded with sideband subtractions.

the expected shapes for electrons, pions, kaons and protons to extract the fraction of electrons and of hadrons for events in $3 < M_{J/\psi e} < 12$ GeV/c^2 and in $4 < M_{J/\psi e} < 6$ GeV/c^2. The obtained electron and hadron contributions are 281 ± 9 (electron) and 31 ± 5 (hadron) in $3 < M_{J/\psi e} < 12$ GeV/c^2 and 167 ± 7 (electron), 9 ± 3 (hadron) in $4 < M_{J/\psi e} < 6$ GeV/c^2, which are good agreement with the fake rate prediction. So no systematic error is assigned from this study.

The total systematic uncertainty on the fake electron background in the $4 < M_{J/\psi e} < 6$ GeV/c^2 window is found to be 2.52 events.

4.4 Residual photon conversion electrons

During the selection of J/ψ-electron sample, electrons identified as from photon conversion are excluded as described in section 3.4.1. The conversion electron is identified if a partner track with $p_T > 400$ MeV/c satisfies $\mid \Delta \cot \Theta \mid < 0.05$ and -0.3 cm $< d_{XY} < 0.5$ cm. We calculate the conversion finding efficiency using a Monte Carlo simulation and estimate the contribution from residual conversion electron to the B_c^+ candidate events from data together with the conversion finding efficiency.

The conversion finding efficiency is defined as a probability to find a partner track satisfying the conversion selection for the identified electrons. The partner track is not required to be identified as an electron. We estimate this efficiency using Monte Carlo samples in two kinds of ways. The primary method is to use the measured p_T spectrum of the inclusive B hadrons [17] to generate a decay chain $B^0 \to J/\psi\pi^0$, $\pi^0 \to \gamma\gamma$ (98%) with one leg goes to an electron-positron pair $\gamma \to e^+e^-$, or $\pi^0 \to \gamma e^+e^-$ (2%). The second method is to use the p_T spectrum of the track

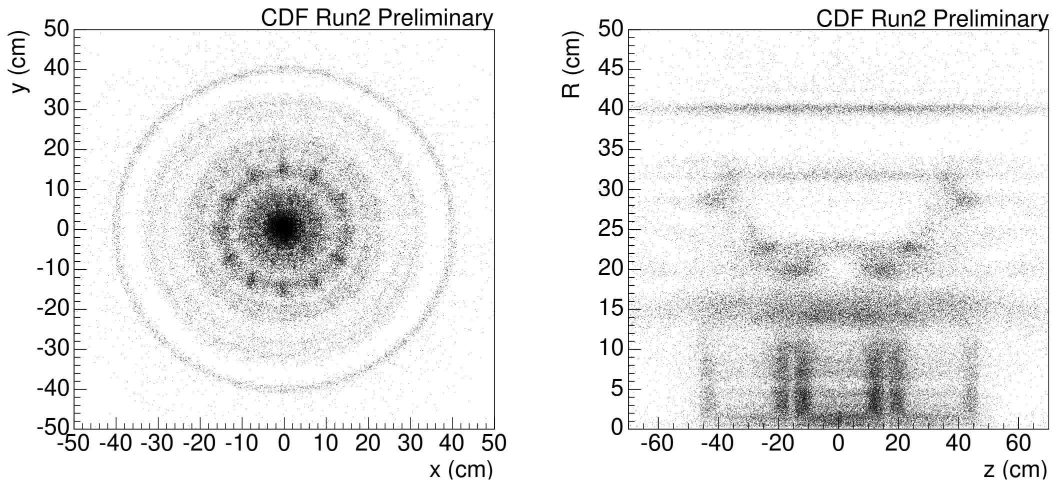

Figure 4.4: Photon conversion points in x-y plane and r-z plane.

found in the J/ψ+track sample for π^0 in $J/\psi\pi^0$ events where π^0 decays as in the first method. The second method generates a conversion electron sample with a softer p_T spectrum thus gives a lower reconstruction efficiency than the first method. The conversion finding efficiency as a function of electron p_T obtained from the first method is plotted in Figure 4.5 and listed in Table 4.3.

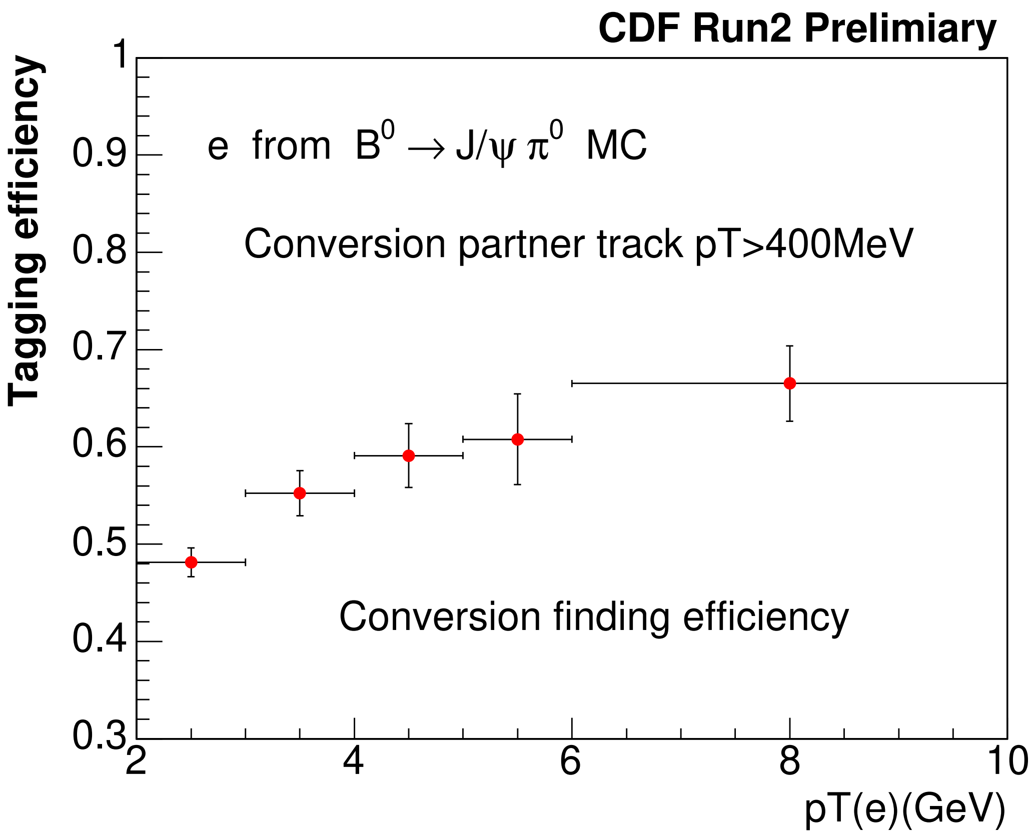

Figure 4.5: Conversion finding efficiency estimated using a Monte Carlo sample generated with decay chain $B^0 \rightarrow J/\psi\pi^0$, $\pi^0 \rightarrow \gamma\gamma$ with $\gamma \rightarrow e^+e^-$(98%) and $\pi^0 \rightarrow \gamma e^+e^-$(2%).

Table 4.3: Conversion finding efficiency (%) estimated using a Monte Carlo sample generated with decay chain $B^0 \rightarrow J/\psi\pi^0$, $\pi^0 \rightarrow \gamma\gamma$ with $\gamma \rightarrow e^+e^-$(98%) and $\pi^0 \rightarrow \gamma e^+e^-$(2%).

p_T(seed electron) (GeV/c)	2-3	3-4	4-5	5-6	6>
ϵ_{conv} (%)	49.8 ± 1.4	55.0 ± 2.2	56.5 ± 3.3	61.5 ± 4.5	69.2 ± 3.4

The residual conversion rate relative to the identified one is simply

$$N_{res} = N_{conv} \times \frac{1 - \epsilon_{conv}}{\epsilon_{conv}}, \tag{4.1}$$

where N_{res} is the number of residual electrons, photon conversion electron which are not found due to limited kinematic coverage, N_{conv} is the number of conversion electrons identified, and ϵ_{conv} is the conversion electron finding efficiency.

We analyze the J/ψ data using the cuts listed in Table 3.3 and identify the J/ψ+conversion electron pairs. We then make an event-by-event correction using Equation 4.1 to obtain the invariant mass distribution of the J/ψ+residual conversion electron pairs, as shown in Figure 4.6. The expected number of the background events in $4 < M_{J/\psi e} < 6$ GeV$/c^2$ is 14.54 events.

The following sources of systematic uncertainty on residual electron background are studied. The p_T spectrum of the electron and its partner track have a large impact on the efficiency estimation. We estimate this effect by comparing the conversion finding efficiency estimated using $B^0 \to J/\psi\pi^0$ Monte Carlo sample with that estimated regarding the track p_T spectrum in the J/ψ+track sample as the π^0 p_T spectrum. From this study, the efficiency difference is 13% to 22% over the p_T bins, which corresponds to a difference of 6.36 events in total.

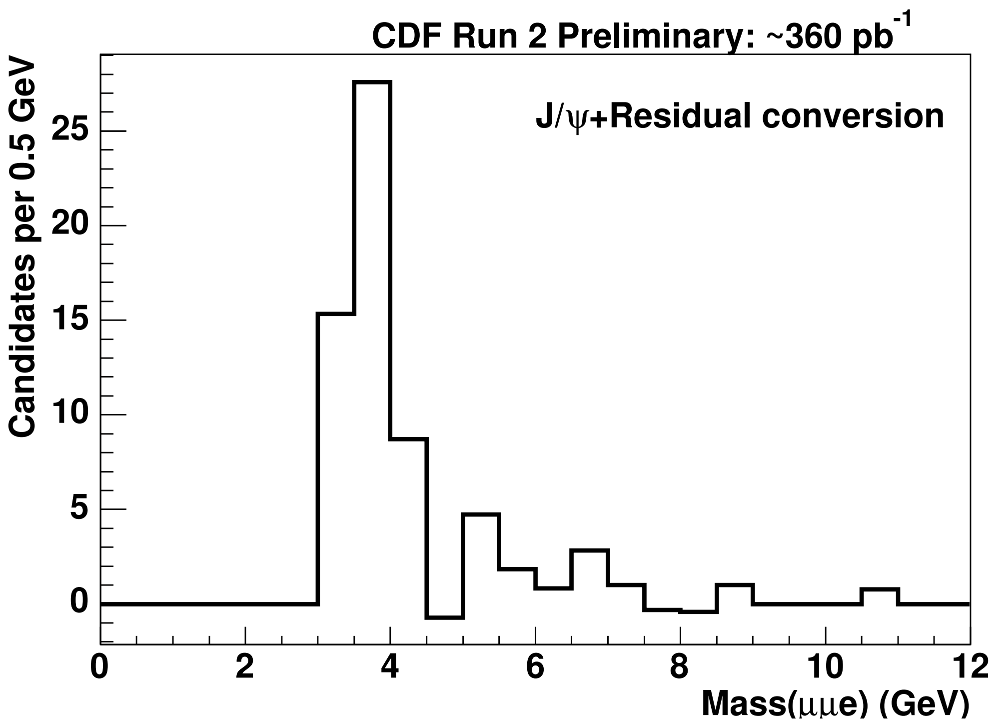

Figure 4.6: Invariant mass distribution of J/ψ+residual conversion electron pair. Fake J/ψ contributions are excluded with sideband subtractions.

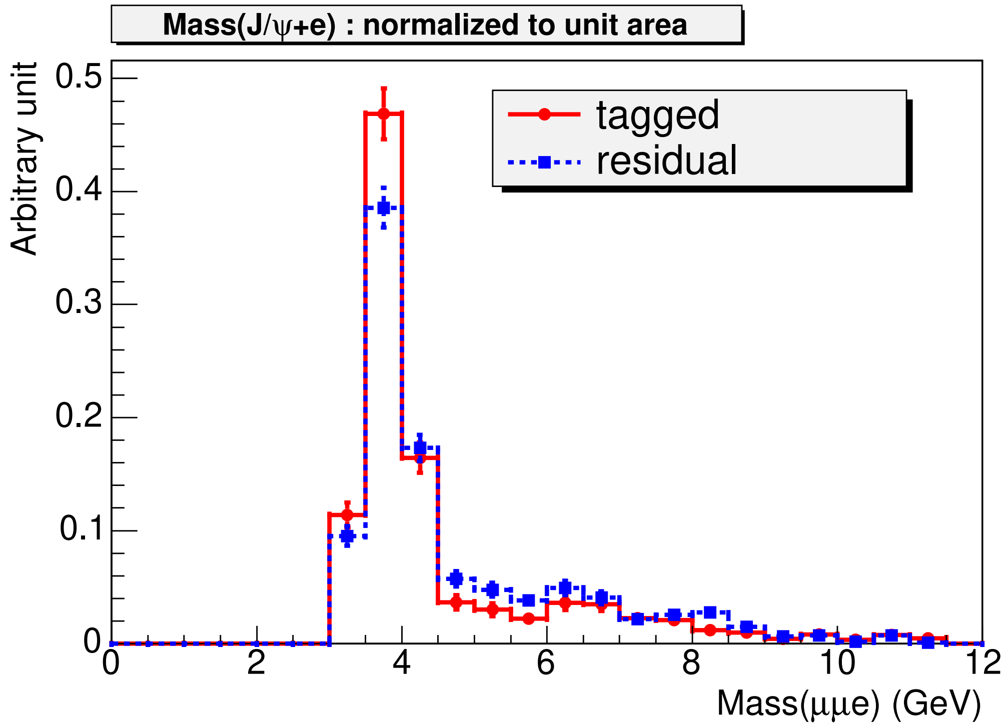

Figure 4.7: Monte Carlo distributions of invariant mass calculated from J/ψ and tagged conversion electron pair (solid lines) or the residual conversion electron (dotted lines). These are normalized to unit area.

Another source of systematic uncertainty is the composition of pure $\pi^0 \to \gamma\gamma$ with $\gamma \to e^+e^-$ and Dalitz decay of $\pi^0 \to \gamma e^+e^-$. The Dalitz-electron finding efficiency is found to be 5% lower than that of pure conversion electrons. The composition of residual conversion electrons from these two sources changes from 98%:2% to 87%:13% after the detector simulation. We assign 100% uncertainty and vary the composition from 97%:3% to 77%:23%. The change of averaged conversion finding efficiency is found to differ by about 1%, which corresponds to the number of residual events of 0.15 events.

We also check the efficiency dependence on the origin where the conversion electron is produced. We set the lifetime of B^0 to be zero in the Monte Carlo simulation and calculate the efficiency. The efficiency differences are less than 1%, which corresponds to the background events of 0.29 events.

We compare the invariant mass distribution from tagged conversion electrons with that from residual conversion electrons using a Monte Carlo. As shown in Figure 4.7 the distributions are similar, so we do not assign systematic uncertainty from this.

Finally, we redo the efficiency and background estimation using different p_T thresholds of 300 MeV/c and 500 MeV/c instead of the default value of 400 MeV/c for the partner tracks.

These results are consistent and we assign no systematic uncertainty from this.

In summary, the total systematic error on the residual conversion background in the $4 < M_{J/\psi e} < 6$ GeV/c^2 window is found to be 6.39 events.

4.5 $b\bar{b}$ background

The $b\bar{b}$ is another major source of background to the B_c^+ signal. The particular process concerned is that one b decays into a J/ψ and its associated $\bar{b}$ produces an electron either in the direct semileptonic decays or through the so-called sequential decays, $\bar{b} \to c \to e$. It is possible that the electron projects through the J/ψ vertex and the invariant mass of the two falls into the B_c^+ search window, thus the events may not be distinguishable from a B_c^+ decay. We estimate the size of this background using a realistic Monte Carlo simulation.

The PYTHIA 6.216 Monte Carlo program [87] is chosen for the generation of the concerned decay chains of the $b\bar{b}$ events. To avoid a double counting and to increase the efficiency of the Monte Carlo generation, the b-hadron is forced to decay to a J/ψ while the $\bar{b}$-hadron is allowed to decay through the default decay table.

There are several parameters relevant to the estimation of amount of background to the B_c^+ signal: the parton distribution function (PDF), the amount of initial state radiations (ISR) determined by the PYTHIA parameter PARP(67), and the relative contributions of the three leading sources for $b\bar{b}$ production. The three leading sources are classified as Flavor Creation (FC), Flavor Excitation (FE) and Gluon Splitting (GS). As pointed out by R. Field [89] and confirmed by the Run-I analysis as in the PRD paper [88], there are sizable contributions from the next to leading order processes of the flavor excitation and the gluon splitting in addition to the leading order process of the flavor creation. The Run-I analysis done by Kevin Lannon *et al.* [88] used a simultaneous fitting to the lifetime distribution of J/ψ and the impact parameter distribution of leptons in two regions of the opening angle ($\Delta\phi$) between the lepton and J/ψ. This analysis concluded that the CDF data is in general consistence with the predictions from PYTHIA after tuning by Rick Field [89], as shown in Table 4.4. It also indicates the CDF data favors a setting of CTEQ5L for PDF, PARP(67)=4 for ISR and the default fractions FC/FE/GS from the PYTHIA. We use events generated using these default settings to estimate the $b\bar{b}$ background in the B_c^+ signal and treat a variation from these settings as systematic uncertainty.

We first check the distribution of opening angles between the two b-quarks on the r-ϕ plane at the generator level without the detector simulation and kinematic cuts on their decay products. Events are generated with the requirement that one of the b-quark has a p_T larger than 5 GeV/c and to be in the absolute value of the pseudo-rapidity less than 1. The three major $b\bar{b}$ production sources are generated using different processes (MSEL=5 for FC, MSEL=1 for FE and GS in addition to FC) as prescribed in references [90] and [88] to use CPU efficiently. As shown in

Table 4.4: Results of CDF $b\bar{b}$ correlation study [88]. Run-I studies with simultaneous lifetime and impact parameter fitting to determine the fraction of the two b-quarks in $\Delta\phi < 90°$ range ($F_{forward}$) are shown.

Run-I $F_{forward}$(%) measurements		
Channel	data	PYTHIA
J/ψ+e	$18.6^{+6.3}_{-5.7}{}^{+0.5}_{-0.6} \pm 1.7$	26.4 ± 0.2
J/ψ+μ	$33.4^{+8.9}_{-7.9}{}^{+7.7}_{-3.0} \pm 2.3$	25.5 ± 0.4

Figure 4.8, the flavor creation produces $b\bar{b}$ pairs mostly back-to-back as expected while the flavor excitation and the gluon splitting have sizable events with the $b\bar{b}$ pairs close together. We then look at the opening angle distribution between b and $\bar{b}$ quark after kinematic cuts. The shape of the three sources stay more or less similar to that before kinematic cuts, as also shown in Figure 4.8.

The Monte Carlo events are then passed through full detector simulation. We analyze the Monte Carlo $b\bar{b}$ events in the same way as the data and apply all cuts including the 90 degree opening angle cut. Muon tracks from J/ψ are required to be from the expected decay chains using the information at generator level. An electron is required to come from different b and in the pseudo-rapidity range of $|\eta| < 1.0$ but not required to be identified as an electron with the calorimeter information. The electron identification efficiencies obtained from isolation-weighted methods, dE/dx cut efficiencies and CES fiducial coverage measured using $B^+ \to J/\psi K^+$ data sample are used to scale down the number of background. The Monte Carlo events are normalized using the $B^+ \to J/\psi K^+$ yields in the Monte Carlo sample and data. In doing so, the relative signal ratio, $N(B^+ \to J/\psi K^+)/N(b \to J/\psi X)$, in Monte Carlo is found to be lower than that in data by a factor of 1.15. We check the effect of muon p_T turn-on curve by re-calculating the ratio using only muons with $p_T > 2.5$ GeV/c and the difference is persistence. We thus attributes this as the decay table problem in Monte Carlo. We scale down the background contributions by 15% accordingly. The J/ψ-electron invariant mass distributions for the background are shown in Figure 4.9. The expected number of this background in $4 < M_{J/\psi e} < 6$ GeV/c^2 is 33.63 events.

As mentioned before the relative fraction of the three sources differs greatly for different PYTHIA parameter settings and between different event generators. The combined opening angle distributions between J/ψ and electron from three sources after the detector simulation and the kinematic selection are shown in Figure 4.10. The distributions with various mixtures of those sources are quite different from each other over the whole opening angle range and as a result the numbers of $b\bar{b}$ backgrounds are also very different. We take the maximum difference of 10.55 events as the uncertainty due to Monte Carlo modeling. This is the largest contribution

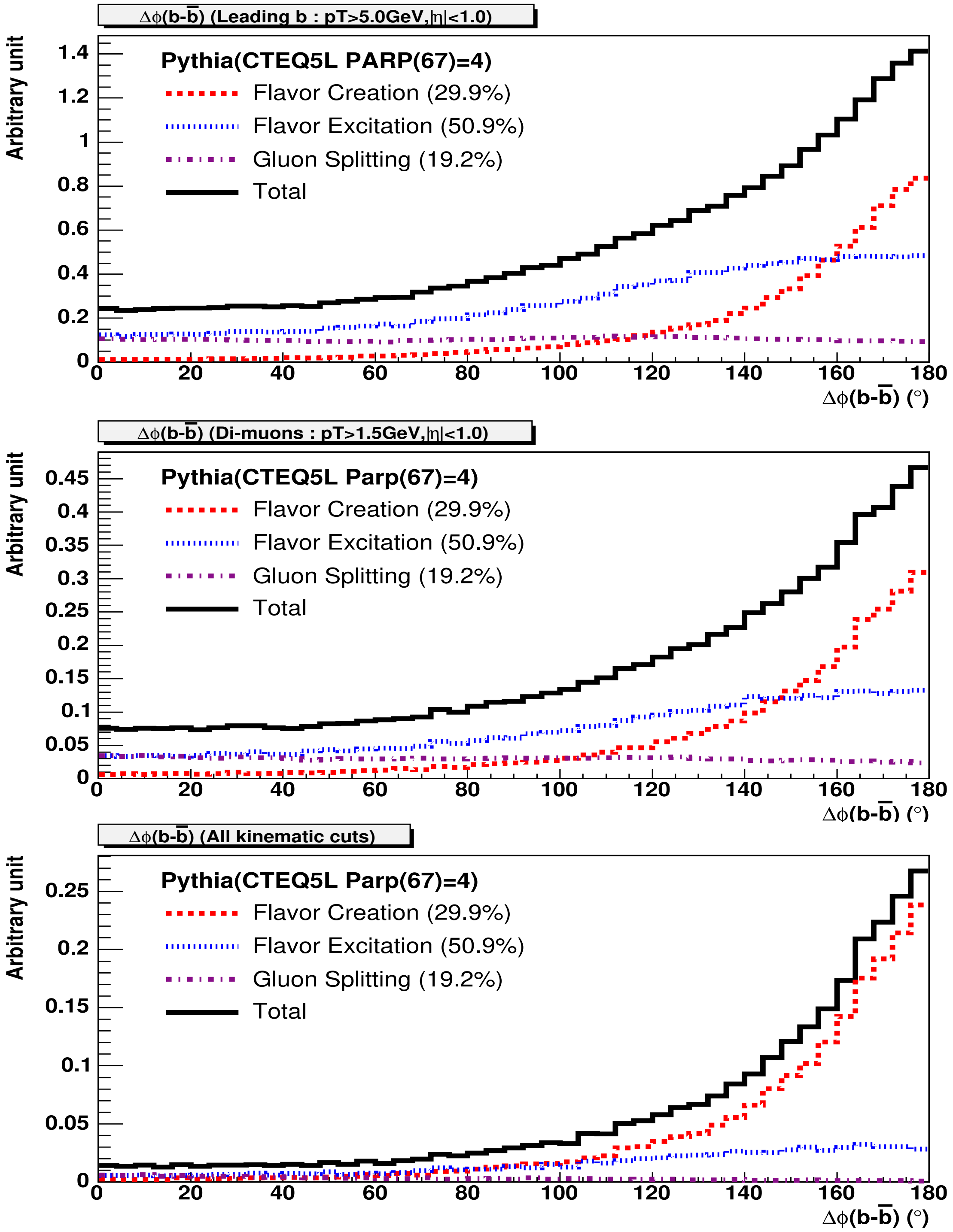

Figure 4.8: Generator level opening angle $\Delta\phi$ distributions between b and $\bar{b}$ from $b\bar{b}$ events for the three sources of flavor creation (red dashed line), flavor excitation (blue dotted line), gluon splitting (purple dot-dashed line) and total (black solid line). The normalized fractions of the three sources are 29.9%:50.9%:19.2%(FC:FE:GS). Applied cuts are p_T(leading b) > 5 GeV/c and $\mid y$(leading b) $\mid < 1$ for the top plot, $p_T(\mu) > 1.5$ GeV/c and $\mid y(\mu) \mid < 1$ for the middle plot and all kinematic cuts for the bottom plot.

to the systematic uncertainties in the $b\bar{b}$ background. Figure 4.11 shows contributions from each production process to the opening angle distribution for the default Monte Carlo setting.

The number of $B^+ \to J/\psi K^+$ events in Monte Carlo is used as a normalization for luminosity. The relative ratios of $N(B^+ \to J/\psi K^+)/N(b \to J/\psi X)$ for the three processes, FC/FE/GS in the Monte Carlo event generation, are found to be different by about 10%. We treat this difference as the systematic uncertainty related with the normalization of the Monte Carlo event generation.

The next piece of systematic uncertainty is from the uncertainty of electron identification efficiency. The uncertainty on electron identification efficiency from isolation is estimated using the differences of isolation-weighted efficiency and the one directly from $\gamma \to e^+e^-$ sample. We assign a systematic uncertainty of 2% (0.96 events). The efficiency dependence on the number of silicon hits is also checked by calculating the efficiency for conversion electron tracks with only 3 silicon hits and 4 or more silicon hits. There is no noticeable differences for the likelihood-based electron ID. We also check the sample dependences of the efficiency by using the conversion sample from electrons in the e+SVT sample instead of electrons with p_T >8 GeV/c in the inclusive electron sample. There is no difference between these two kinds of electron sample.

Finally, the statistical uncertainties from the number of $B^+ \to J/\psi K^+$ events in data sample (2.1%), from CES fiducial coverage (0.33%) and dE/dx efficiency (2.1%) are directly transferred to the uncertainty on the number of $b\bar{b}$ background.

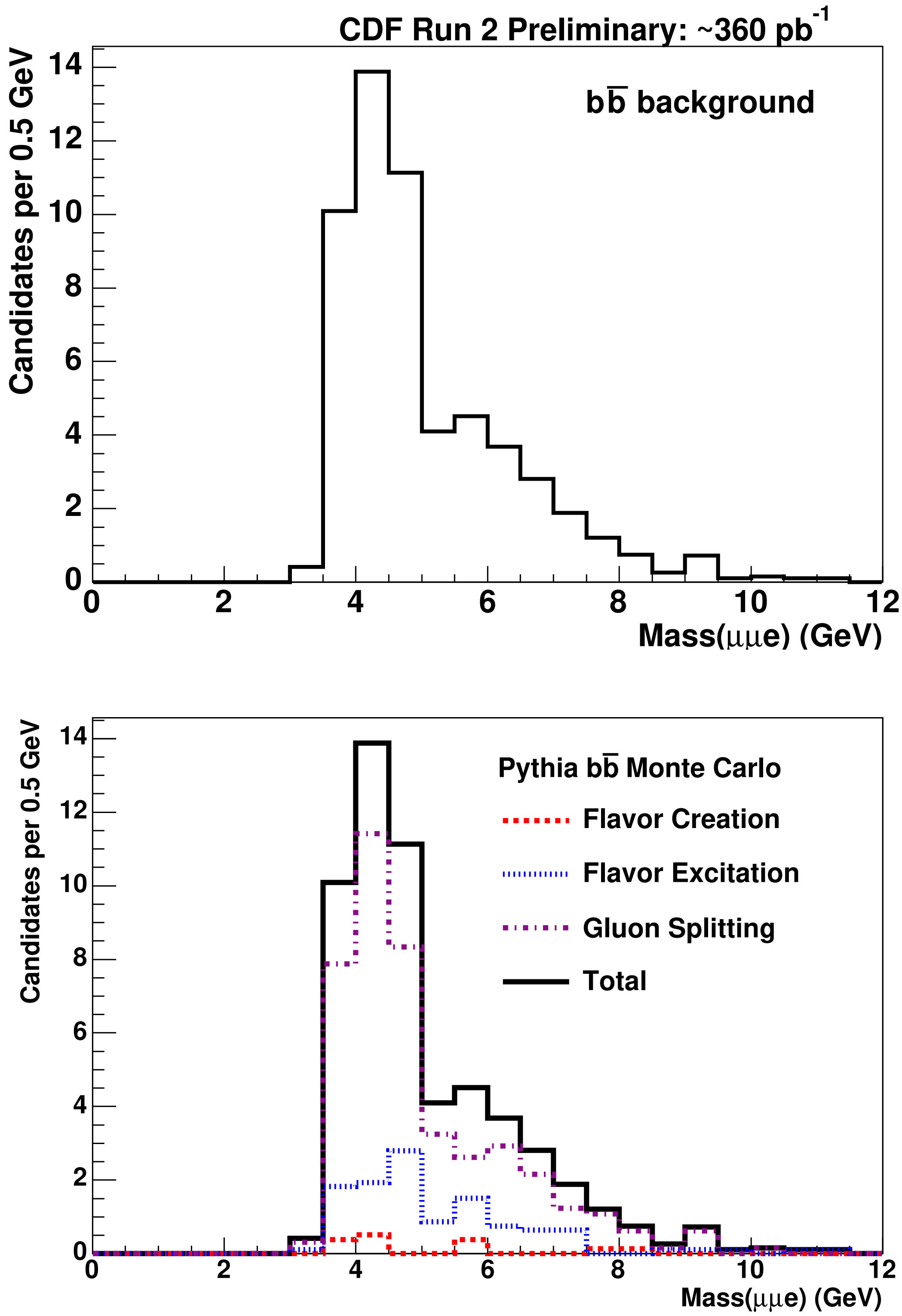

Figure 4.9: Invariant mass distribution of J/ψ-electron pair from $b\bar{b}$ background (top plot). Contributions from three production processes (FC/FE/GS) are also shown in bottom plot.

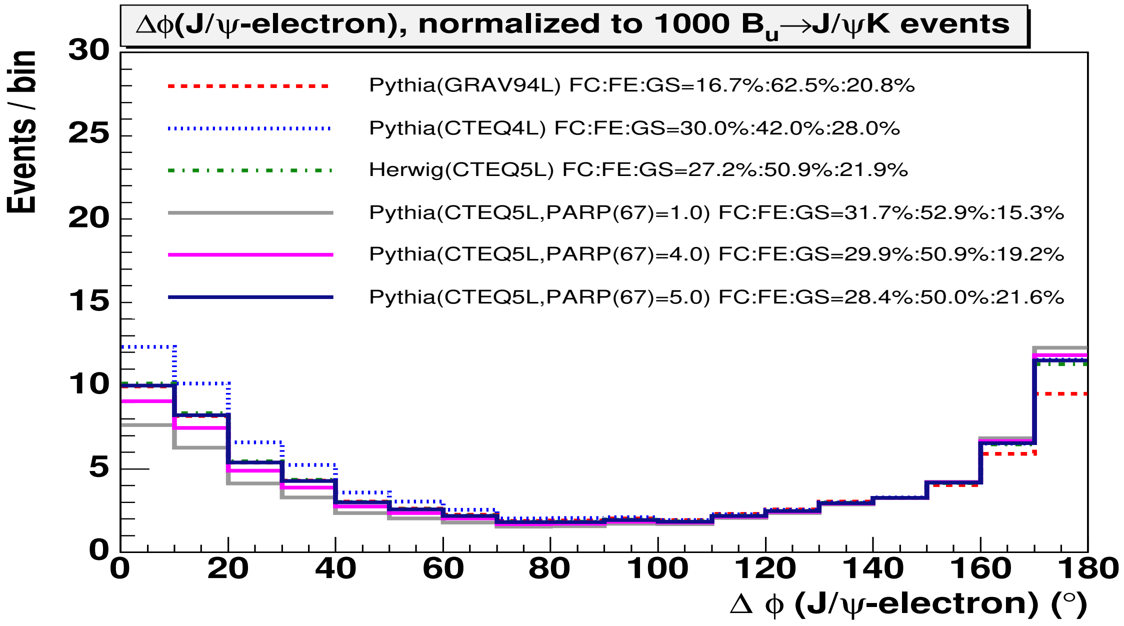

Figure 4.10: Opening angle $\Delta\phi$ distributions of J/ψ and electron with the detector simulation. Distributions from different generators with different parameter settings are shown.

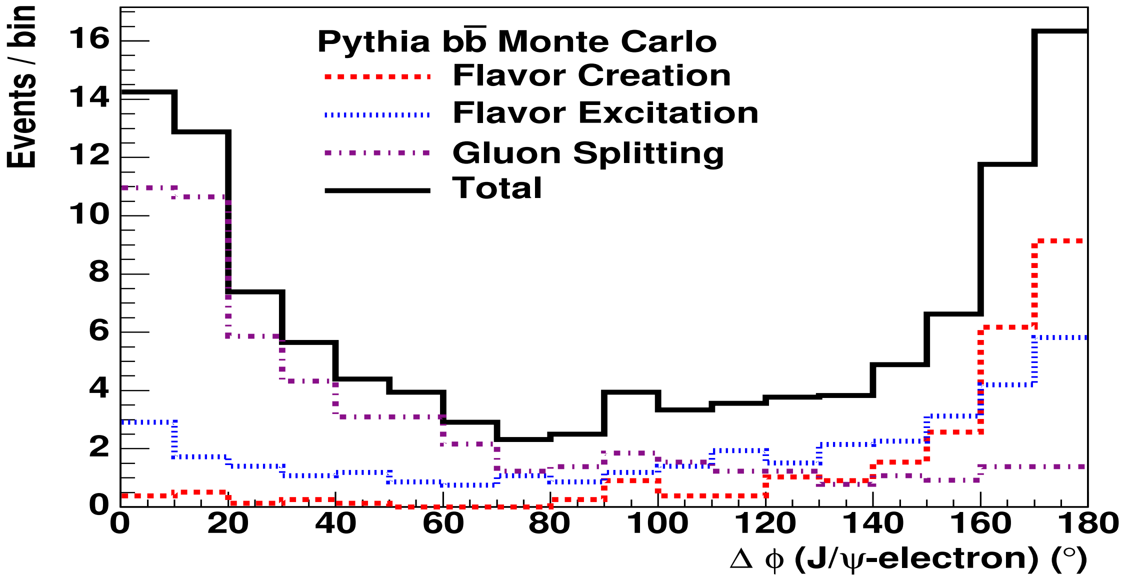

Figure 4.11: Opening angle $\Delta\phi$ distributions of J/ψ and electron predicted by Pythia Monte Carlo with the detector simulation after all kinematic cuts. Contributions from the three production processes (FC/FE/GS) are also shown. The normalized fractions of the three sources are 29.9%:50.9%:19.2%(FC:FE:GS).

Chapter 5

The B_c^+ Meson Production Cross Section

5.1 Signal counting

Finally, the J/ψ-electron candidates are counted as a function of the invariant mass using the selections discussed earlier in Table 3.3. The electrons are required to meet the identification criteria $\mathcal{P}_e < 0.7$. dE/dx requirement of $Z_e/\sigma_{Z_e} > -1.3$ is also applied. Conversion electrons are removed if they satisfy $\mid \Delta \cot \Theta \mid < 0.05$, -0.3 cm $< d_{XY} <$ 0.5 cm and p_T(partner) $>$ 400 MeV/c. In addition, J/ψ-electron pair is removed from the candidate list if the invariant mass of the pair is within 50 MeV/c^2 around the B^+ meson mass of 5.279 GeV/c^2 [9] after assigning a kaon mass to the electron. The numbers of J/ψ-electron candidates for various mass windows are listed in Table 5.1.

By counting the candidate events in the expected B_c^+ mass window of $4 < M_{J/\psi e} < 6$ GeV/c^2, the number of J/ψ-electron candidates of 178.5 ± 14.7 over an estimated background of $63.6 \pm 4.9 \pm 13.1$ is observed. The net excess of signal is 114.9 ± 15.5 events. The number of expected background events with systematic uncertainties and B_c^+ signal excess in all invariant mass windows are listed in Table 5.2. In the higher mass window, $7 < M_{J/\psi e} < 12$ GeV/c^2 where the B_c^+ signal is not expected to be present, we see an excess of 1.78 events per 1 GeV/c^2 mass window, where the excess is the difference of the number of events between the data and the expected background including both statistical and systematic uncertainties. Although the excess is still consistent with statistical fluctuation, we conservatively assign a systematic uncertainty from it by assuming a linear extrapolation to the B_c^+ signal region. The estimated total background in the $4 < M_{J/\psi e} < 6$ GeV/c^2 mass window is now $63.6 \pm 4.9 \pm 13.6$ with the signal events as $114.9 \pm 15.5 \pm 13.6$, where the first uncertainty is statistical and the second is systematical. In Figure 5.1, the expected B_c^+ signal shape is compared with the data.

By popular demand, we also calculate the significance of the signal over the background. To

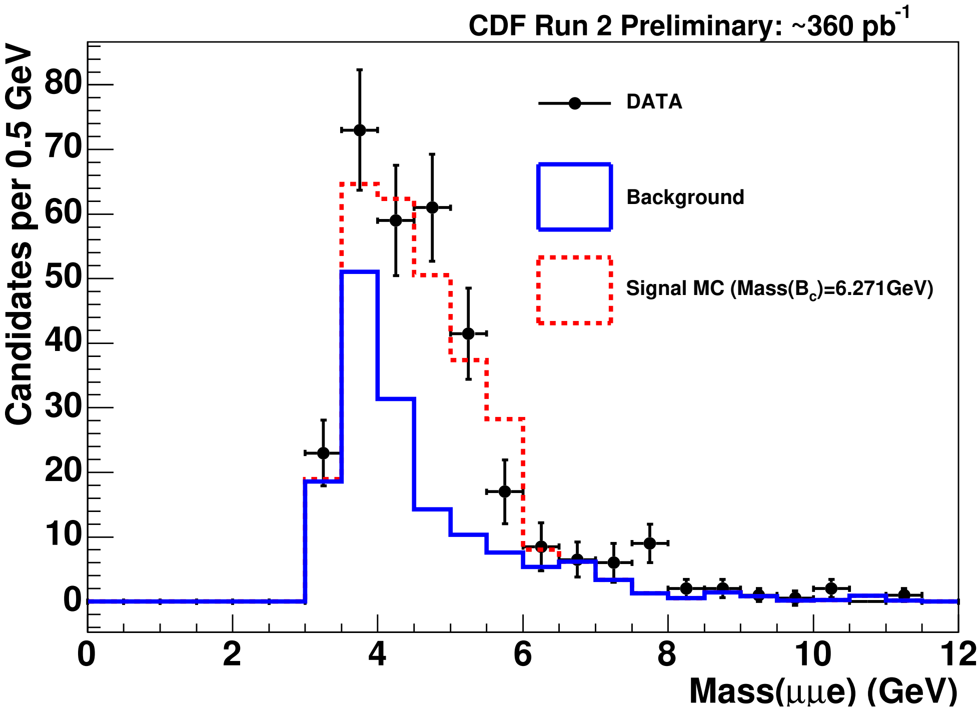

Figure 5.1: Comparison of the expected B_c^+ signal to the data for the invariant mass distribution of J/ψ-electron. Plot shows all data points with estimated background and expected signal shape. Fake J/ψ contributions are excluded with mass sideband subtractions.

do this, we add the fake J/ψ contribution back to the total number of J/ψ-electron events and also to the total background. So the significance is based on 203 signal candidate events over background described with a Gaussian distribution truncated to positive value with a mean of 88.09 and a width of 14.87. The probability for such background to fluctuate to the size of signal candidate events is 3.2×10^{-9} which corresponds to a significance of 5.9σ.

5.2 Cross section measurement

From the B_c^+ yield in Table 5.1, the B_c^+ production cross section times the $B_c^+ \to J/\psi e^+ \nu_e$ branching fraction $\sigma(B_c^+) \cdot \mathcal{B}(Bc^+ \to J/\psi e^+ \nu_e)$ is calculated. We express this physics quantity relative to that for the topologically similar decay of $B^+ \to J/\psi K^+$. The reconstructed number of events are corrected by efficiencies and acceptances to calculate the cross section ratio:

$$\begin{aligned} \frac{\sigma(B_c^+) \cdot \mathcal{B}(B_c^+ \to J/\psi e^+ \nu_e)}{\sigma(B^+) \cdot \mathcal{B}(B^+ \to J/\psi K^+)} &= \frac{N(B_c^+)/(A_{\mathrm{kin}}(B_c^+) \times \epsilon(B_c^+))}{N(B^+)/(A_{\mathrm{kin}}(B^+) \times \epsilon(B^+))} \\ = \frac{N(B_c^+)}{N(B^+)} \times \frac{A_{\mathrm{kin}}(B^+)}{A_{\mathrm{kin}}(B_c^+)} \times \frac{\epsilon(B^+)}{\epsilon(B_c^+)} &= \frac{N(B_c^+)}{N(B^+)} \times R^K \times R^\epsilon, \end{aligned}$$

Table 5.1: Background estimations and data excess in J/ψ-electron invariant mass windows. The selections for J/ψ-electron and B^+ are listed in Table 3.3 and Table 3.4. There are 2872 ± 59 $B^+ \to J/\psi K^+$ events reconstructed in the same data set.

$M_{J/\psi e}(\mathrm{GeV}/c^2)$	3-4	4-6	6-7	7-12	total
Fake e (J/ψ peak)	17.83 ± 0.32	18.73 ± 0.30	1.79 ± 0.09	1.61 ± 0.08	39.96 ± 0.45
Fake e (sideband x2)	3.27 ± 0.14	6.59 ± 0.18	0.82 ± 0.06	0.49 ± 0.04	11.17 ± 0.23
Fake Electron	$\mathbf{16.20 \pm 0.32}$	$\mathbf{15.43 \pm 0.31}$	$\mathbf{1.38 \pm 0.10}$	$\mathbf{1.37 \pm 0.09}$	$\mathbf{34.38 \pm 0.47}$
Tagged Conv. (J/ψ peak)	48.00 ± 6.93	23.00 ± 4.80	4.00 ± 2.00	3.00 ± 1.73	78.00 ± 8.83
Tag. Conv. (sidebands x2)	6.00 ± 2.45	11.00 ± 3.32	0.00 ± 0.00	2.00 ± 1.41	19.00 ± 4.36
Res. Conv. (J/ψ peak)	45.63 ± 6.59	19.52 ± 4.11	3.66 ± 1.83	2.79 ± 1.62	71.59 ± 8.14
Res.Conv. (sidebands x2)	5.44 ± 2.23	9.96 ± 3.02	0.00 ± 0.00	1.45 ± 1.03	16.84 ± 3.89
Res. Conv electron	$\mathbf{42.91 \pm 6.68}$	$\mathbf{14.54 \pm 4.38}$	$\mathbf{3.66 \pm 1.83}$	$\mathbf{2.07 \pm 1.70}$	$\mathbf{63.17 \pm 8.37}$
$b\bar{b}$	$\mathbf{10.50 \pm 1.23}$	$\mathbf{33.63 \pm 2.20}$	$\mathbf{6.49 \pm 0.97}$	$\mathbf{5.30 \pm 0.87}$	$\mathbf{55.92 \pm 2.84}$
Total background	$\mathbf{69.61 \pm 6.80}$	$\mathbf{63.59 \pm 4.91}$	$\mathbf{11.53 \pm 2.07}$	$\mathbf{8.74 \pm 1.91}$	$\mathbf{153.47 \pm 8.85}$
Data in (J/ψ peak)	107.00 ± 10.34	203.00 ± 14.25	19.00 ± 4.36	26.00 ± 5.10	355.00 ± 18.84
Data (sidebands x2)	22.00 ± 4.69	49.00 ± 7.00	8.00 ± 2.83	5.00 ± 2.24	84.00 ± 9.17
Data J/ψ +e	$\mathbf{96.00 \pm 10.61}$	$\mathbf{178.50 \pm 14.67}$	$\mathbf{15.00 \pm 4.58}$	$\mathbf{23.50 \pm 5.22}$	$\mathbf{313.00 \pm 19.39}$
Excess	$\mathbf{26.39 \pm 12.60}$	$\mathbf{114.91 \pm 15.47}$	$\mathbf{3.47 \pm 5.03}$	$\mathbf{14.76 \pm 5.56}$	$\mathbf{159.53 \pm 21.32}$

where $A_{\mathrm{kin}}(B_c^+)$ and $A_{\mathrm{kin}}(B^+)$ denote the kinematic acceptances for B_c^+ and B^+ including effects from momentum, geometry and lifetime selection cuts; $\epsilon(B_c^+)$ and $\epsilon(B^+)$ are the trigger and reconstruction efficiencies for B_c^+ and B^+; R^K is kinematic acceptance ratio between B^+ and B_c^+, $R^K = A_{\mathrm{kin}}(B^+)/A_{\mathrm{kin}}(B_c^+)$; and R^ϵ is the trigger and reconstruction efficiency ratio between B^+ and B_c^+, $R^\epsilon = \epsilon(B^+)/\epsilon(B_c^+)$. The efficiency ratio R^ϵ can be further broken down to

$$
\begin{aligned}
R^\epsilon &= \frac{\epsilon^u(\mathrm{trigger}) \times \epsilon^u(\mathrm{vertex}) \times \epsilon^u(J/\psi) \times \epsilon^u(K\mathrm{-track})}{\epsilon^c(\mathrm{trigger}) \times \epsilon^c(\mathrm{vertex}) \times \epsilon^c(J/\psi) \times \epsilon^c(e\mathrm{-track}) \times \epsilon(Cal) \times \epsilon(dE/dx)} \\
&= \frac{1}{\epsilon(Cal) \times \epsilon(dE/dx)},
\end{aligned}
$$

where $\epsilon^{u/c}(\mathrm{trigger})$ are the di-muon trigger efficiencies for $B^+ \to J/\psi K^+$ and $B_c^+ \to J/\psi e^+ \nu_e$, $\epsilon^{u/c}(\mathrm{vertex})$ the 3-prong vertex reconstruction efficiencies, $\epsilon^{u/c}(J/\psi)$ the reconstruction efficiencies for $J/\psi \to \mu^+\mu^-$ decay, $\epsilon^u(K\mathrm{-track})$ and $\epsilon^c(e\mathrm{-track})$ are the tracking efficiencies for the kaon and electron tracks, $\epsilon(Cal)$ and $\epsilon(dE/dx)$ are the electron identification efficiencies using by the calorimeter information and dE/dx information, respectively. Most of the efficiencies for B_c^+ are expected to be close to those for B^+ except for the additional $\epsilon(Cal) \times \epsilon(dE/dx)$.

The explicit cut on the combined momentum of J/ψ and electron, $p_{T_{J/\psi e}} > 5$ GeV/c imposed a limit on the $p_{T_{B_c}}$ range we are sensitive to. From Monte Carlo simulation, as shown in Figure 5.2, we are limited to the transverse momentum range of $p_{T_{B_c}} > 4$ GeV/c and the rapidity range of $\mid y_{B_c} \mid < 1$ for the B_c^+ meson. So the cross section here is defined as that for kinematic range of $p_{T_B} > 4$ GeV/c with $\mid y_B \mid < 1$. Accordingly, the definition of the kinematic

Table 5.2: Summary of systematic uncertainties.

$M_{J/\psi e}$	3-4 GeV/c^2	4-6 GeV/c^2	6-7 GeV/c^2	7-12 GeV/c^2	3-12 GeV/c^2
Isolation	2.51	2.24	0.20	0.19	5.14
# of Si hits	1.16	1.11	0.10	0.10	2.47
π/K/p fraction	0.14	0.29	0.02	0.03	0.48
Fake rate - stat.	0.11	0.14	0.04	0.04	0.19
Fake e - total	16.20 $\pm 0.32 \pm 2.77$	15.43 $\pm 0.31 \pm 2.52$	1.38 $\pm 0.10 \pm 0.23$	1.37 $\pm 0.09 \pm 0.22$	34.38 $\pm 0.47 \pm 5.72$
p_T spectra	20.84	6.36	1.75	0.84	29.79
Dalitz decay	0.87	0.15	0.05	0.07	1.14
Lifetime	0.86	0.29	0.07	0.04	1.26
ϵ_{conv}-stat.	0.61	0.55	0.13	0.00	0.84
Conversion -total	42.91 $\pm 6.68 \pm 20.88$	14.54 $\pm 4.38 \pm 6.39$	3.66 $\pm 1.83 \pm 1.76$	2.07 $\pm 1.70 \pm 0.84$	63.17 $\pm 8.37 \pm 29.85$
PDF/ISR	3.43	10.55	2.10	1.57	17.66
$\epsilon(dE/dx)$	0.10	0.32	0.06	0.05	0.53
$\epsilon(Cal)$-stat.	0.14	0.46	0.09	0.07	0.77
$\epsilon(Cal)$-isolation	0.30	0.96	0.19	0.15	1.60
$\mathcal{B}(B^+ \to J/\psi K^+)$	1.05	3.36	0.65	0.53	5.59
N_{B^+} stat. in data	0.19	0.62	0.12	0.10	1.03
N_{B^+} stat. in MC	0.20	0.64	0.12	0.10	1.06
CES coverage	0.10	0.31	0.06	0.05	0.51
$b\bar{b}$ - total	10.50 $\pm 1.23 \pm 3.61$	33.63 $\pm 2.20 \pm 11.17$	6.49 $\pm 0.97 \pm 2.22$	5.30 $\pm 0.87 \pm 1.67$	55.92 $\pm 2.84 \pm 18.68$
High mass excess	1.78	3.56	1.78	8.89	16.01
Total background	69.61 $\pm 6.83 \pm 21.45$	63.59 $\pm 4.91 \pm 13.59$	11.53 $\pm 2.07 \pm 3.35$	8.74 $\pm 1.91 \pm 9.09$	153.47 $\pm 8.85 \pm 39.10$
Data	96.00 ± 10.61	178.50 ± 14.67	15.00 ± 4.58	23.50 ± 5.22	313.00 ± 19.39
Excess	26.39 $\pm 12.60 \pm 21.45$	114.91 $\pm 15.47 \pm 13.59$	3.47 $\pm 5.03 \pm 3.35$	14.76 $\pm 5.56 \pm 9.09$	159.53 $\pm 21.32 \pm 39.10$

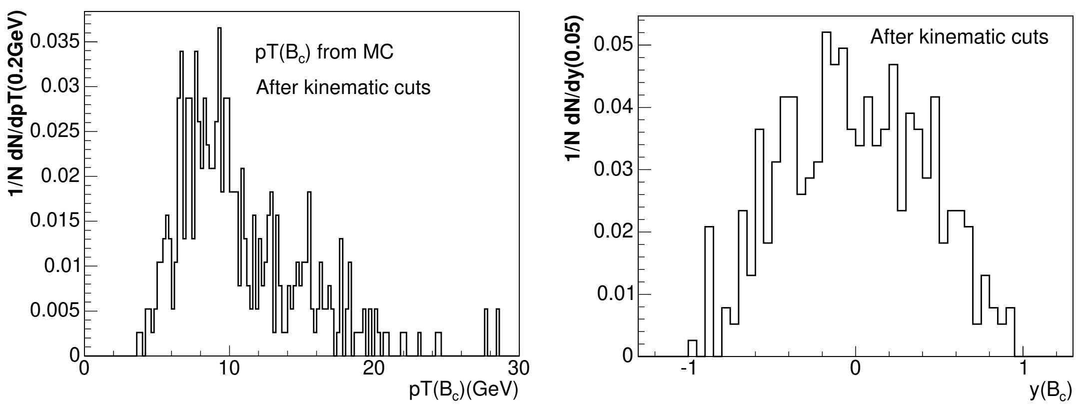

Figure 5.2: The kinematic limited range of p_T (left) and rapidity (right) for B_c^+ meson in the Monte Carlo simulation events after applying the same event selection criteria as for data. The input p_T spectrum of B_c^+ is that from reference [62].

acceptances, $A_{\rm kin}(B^+)$ and $A_{\rm kin}(B_c^+)$, are the fraction of events passing kinematic cuts (p_T, η and L_{xy}) for the B decay channels generated in the kinematic range of $p_{T_B} > 4$ GeV/c and $\mid y_B \mid < 1$

5.2.1 Acceptance estimation for B_c^+ and B^+

Monte Carlo simulated events are used to estimate the kinematic acceptance. Pure signal $B_c^+ \to J/\psi e^+ \nu_e$ and $B^+ \to J/\psi K^+$ events are generated. The events are generated with $p_T > 4$ GeV/c and $\mid y \mid < 1$ for pure signals $B_c^+ \to J/\psi e^+ \nu_e$ and $B^+ \to J/\psi K^+$ and pass through the full detector simulation. Monte Carlo events are analyzed in the same way as for data.

The input p_T spectrum for B_c^+ is from a theoretical calculation [62, 91] and the mass and lifetime of B_c^+ are chosen to be 6.271 GeV/c^2 and 0.55 ps for our central value of acceptance calculation. The inclusive B p_T spectrum measured at CDF [17] is used for the B^+ p_T spectrum. The two spectra are shown in Figure 5.3.

The input B_c^+ p_T spectrum is much softer than that of B^+. Since there is no experimental measurement for the B_c^+ p_T spectrum yet, we will vary the spectrum at the acceptance calculation as one source of systematic uncertainty.

One of the important cuts in event selection is the decay length significance of the 3-prong vertex, $L_{xy}/\sigma_{L_{xy}} > 3$, where the signed decay length is calculated from the distance between the 3-prong vertex, reconstructed using di-muon and an electron or kaon track, and the beam spot where $b-$hadron is assumed to be produced. We first check the σ_{Lxy} calculation in Monte Carlo simulation by comparing the error distribution and also by comparing the pull distributions. In general, the Monte Carlo events tend to have a larger error than the data. The width of the pull distribution tends to be close to 1 while in data the pull distribution has a width larger than 1. Our estimation is in a good agreement with the observation of other CDF measurements [92] where a pull distribution width of 1.241 ± 0.016 is extracted for $B^+ \to J/\psi K^+$. For our central value calculation for acceptance, we scale down the error on decay length for Monte Carlo events to force it to have a pull distribution width σ of 1.241. We add the differences before and after error scaling as another source of systematic uncertainties.

In Table 5.3, the acceptance ratios $R^K = A_{\rm kin}(B^+)/A_{\rm kin}(B_c^+)$ for different Monte Carlo input parameters are listed. The uncertainties on the B_c^+ p_T spectrum and lifetime are the source of two biggest systematic uncertainties on the acceptance ratio. The p_T spectrum from the theoretical prediction [62] is replaced with that measured by CDF for inclusive $H_b \to J/\psi X$ [17]. We also check the variations of the p_T spectrum in reference [62, 93] for different B_c^+ mass and different B_c^+ production processes, such as $gg \to B_c^+$, $gg \to B_c^{*+}$ and $q\bar{q} \to B_c^+$. The changes on the acceptance ratio are found to be much smaller than the one obtained using inclusive $H_b \to J/\psi X$ spectrum. The lifetime is varied from 0.4 ps to 0.7 ps [45]. The shifts from the mass variation are within statistical uncertainty and we take the largest of the two changes as symmetric uncertainty. Beside the lifetime variation, we assign symmetric uncertainty for p_T spectrum and decay length error scaling to cover any potential changes in the opposite direction.

The Monte Carlo events for the acceptance calculation are generated with the semileptonic decay $B_c^+ \to J/\psi e^+ \nu_e$. Other inclusive semileptonic decays $B_c^+ \to J/\psi e^+ \nu_e X$ where the J/ψ, electron and X are decay products from higher mass states, are expected to have a lower reconstruction efficiency since they produce a J/ψ and electron pair with softer momentum and also with a smaller invariant mass. We generate these events using branching fractions predicted in a theory calculation [45]. The acceptance ratio R^K for these decays is found to be 16.70 ± 0.48 for $p_T > 4$ GeV/c while it is 4.416 ± 0.082 for the $B_c^+ \to J/\psi e^+ \nu_e$ decays. These numbers imply that the averaged acceptance of $B_c^+ \to J/\psi e^+ \nu_e X$ is only 26% of that of $B_c^+ \to J/\psi e^+ \nu_e$. The contribution from these $B_c^+(B_c^{*+}) \to J/\psi e^+ \nu_e X$ decays to the reconstructed semileptonic decays is about 3.4% instead of 11.6% calculated from the branching fractions. So we treat this contribution as one source of systematic uncertainty for the acceptance calculation. In Table 5.3, the differences of R^K before and after including the $B_c^+ \to J/\psi e^+ \nu_e X$ decay are around 8% as expected.

We follow CDFNote 6391 [94] to estimate an uncertainty on the kaon track detection due to the detector material ambiguity in the simulation. On average, the kaon track has a probability of 4% to decay inside the CDF detector due to nuclear interactions (see Table 14 of CDFNote 6391). Taking an uncertainty of 25% on this probability, we assign a 1% systematic error on the acceptance of $B^+ \to J/\psi K^+$. We follow the $W^+ \to e^+ \nu_e$ cross section analysis [95] to assign a 1% uncertainty on the electron track detection due to the detector material ambiguity in Monte Carlo. Thus the overall uncertainty on the acceptance ratio R^K due to material ambiguity in

Monte Carlo simulation is 2%.

There is no di-muon trigger simulation implemented in the acceptance ratio calculation. We expect the di-muon trigger has similar efficiency for both B_c^+ and B^+ channels. Nevertheless, we estimate the effect by re-weighting the reconstructed events by the efficiency curves from reference [96] and re-calculate the acceptance ratio, as shown in Table 5.3. The acceptance ratio is found to be about 2.7% lower which come from the small differences in the muon p_T and opening angle distributions of the $B_c^+ \to J/\psi e^+ \nu_e$ and $B^+ \to J/\psi K^+$ decays.

After adding all variations in quadrature and then averaging the asymmetric errors as the total systematic error, the kinematic acceptance ratio is found to be

$$R^K\,(p_{T_B} > 4, \quad |\, y_B \,| < 1) \quad = \quad 4.42 \pm 1.02. \tag{5.1}$$

Table 5.3: The calculated acceptance ratio, $R^K = A_{\rm kin}(B^+)/A_{\rm kin}(B_c^+)$. The central value is calculated using with $M_{B_c} = 6.271$ GeV/c^2, $\tau_{B_c} = 0.55$ ps, p_T spectrum from reference [62] and with L_{xy} scaling down.

MC parameters	$R^K(p_{T_B} > 4, \mid y_B \mid < 1)$	ΔR^K
Central value	4.416 ± 0.082	0
$M_{B_c} = 6.291$ GeV/c^2	4.403 ± 0.082	± 0.013
$M_{B_c} = 6.251$ GeV/c^2	4.394 ± 0.082	± 0.022
$\tau_{B_c} = 0.70$ ps	4.076 ± 0.074	-0.34
$\tau_{B_c} = 0.40$ ps	5.006 ± 0.096	$+0.59$
$H_b \to J/\psi X$ p_T spectrum	3.578 ± 0.062	± 0.838
No L_{xy} error scaling	4.576 ± 0.086	± 0.16
$B_c^+ \to J/\psi e^+ \nu_e X$	4.769 ± 0.090	$+0.353$
Trigger simulation	4.299 ± 0.079	-0.117

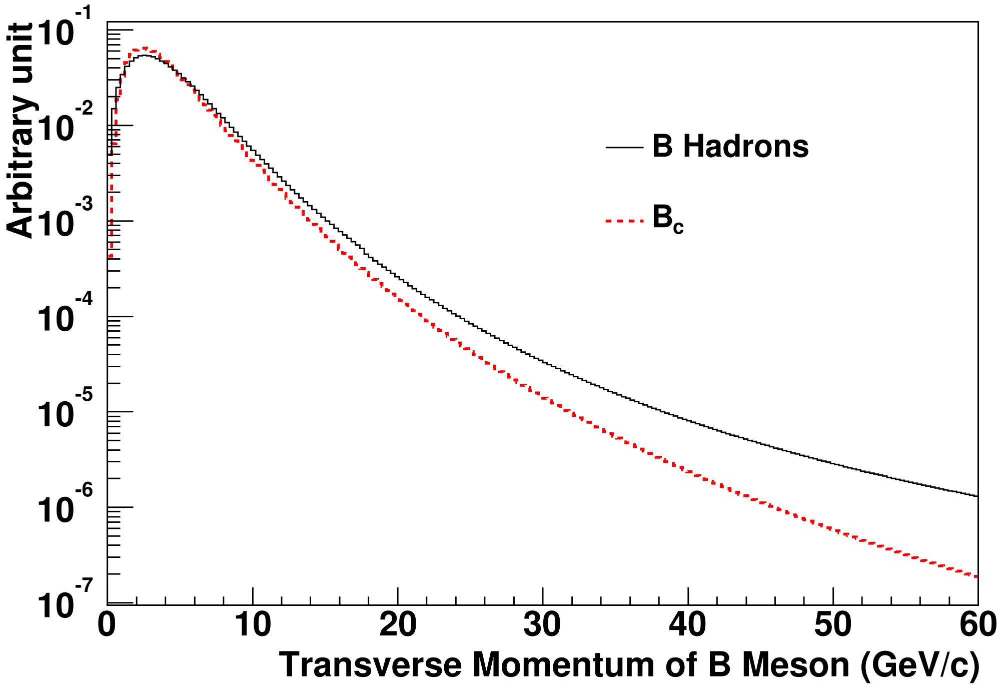

Figure 5.3: Input p_T spectra of B_c^+ and B^+ mesons in the Monte Carlo simulation. p_T spectrum used for B_c^+ mesons (red, dashed lines) is obtained from reference [62], and that for B^+ mesons (black, solid lines) is from reference [17], which is measured spectrum by RunII CDF.

5.2.2 Cross-section result

Using the acceptance ratio of 4.42 ± 1.02 calculated from the Monte Carlo simulation for B mesons with $p_T > 4$ GeV/c in rapidity range of $\mid y \mid < 1$, the electron identification efficiency of $69.35 \pm 1.69\%$ and the dE/dx cut efficiency $90.56 \pm 0.87\%$ measured using electrons from data, we correct the $B_c^+ \to J/\psi e^+ \nu_e$ and the $B^+ \to J/\psi K^+$ signal yields to 114.9 ± 15.5(stat.)± 13.6(syst.) and 2872 ± 59. The resulting cross section ratio is

$$\frac{\sigma(B_c^+) \cdot \mathcal{B}(B_c^+ \to J/\psi e^+ \nu_e)}{\sigma(B^+) \cdot \mathcal{B}(B^+ \to J/\psi K^+)} = 0.282 \pm 0.038 \pm 0.035 \pm 0.065,$$

where the first uncertainty is statistical from B_c^+ and B^+ yields, the second is systematic due to B_c^+ yield systematic uncertainty and the third is systematic from the acceptance ratio calculation.

In order to compare with CDF Run-I measurement closely, we increase the p_T cut on J/ψ-electron and B^+ from 5 GeV/c to 6.5 GeV/c to obtain the cross section ratio for $p_{T_{B_c}} > 6$ GeV/c. The number of events is 94.38 ± 13.72(stat.) $\pm$ 11.69(syst.) for B_c^+ yield and 2621 ± 55 for B^+ with an acceptance ratio of 4.217 ± 0.897. The cross section ratio is thus 0.242 ± 0.036(stat.) $\pm$ 0.031(yield) $\pm$ 0.051(acceptance). This is 0.9σ higher than the Run-I cross section result of 0.155 ± 0.046(stat.) ± 0.038(syst.) ± 0.031(lifetime) after taking out the Run-I correction factor of 0.85 for contribution of higher state decay $B_c^+ \to J/\psi e^+ \nu_e X$. Systematic uncertainty of the B_c^+ p_T spectrum is the dominant uncertainty in both measurements. The difference of the central values is partially explained by the choice of input B_c^+ p_T spectrum. The total uncertainty in Run-II is about 30%, which is comparable with Run-I total uncertainty about 40%.

Chapter 6

Measurement of the B_c^+ Meson Lifetime

We have established the B_c^+ signal with $L_{xy}/\sigma_{L_{xy}} > 3$ cut and measured the production cross section ratio. The decay length cut is to be released to measure the B_c^+ lifetime. The prompt background, which was suppressed by the decay length cut, is estimated using the decay length distribution. Negative decay lengths are included to have a convenient parameterization of the proper decay length distribution. B_c^+ candidate events with a large error ($\sigma_{L_{xy}} > 70\ \mu$m) on decay length are excluded to ensure the quality of the lifetime fitting.

783 J/ψ-electron candidates in the invariant mass window of $4 < M_{J/\psi e} < 6$ GeV/c^2 are found after all the selection cuts. Following the same procedure as in the cross section measurement, the background contributions from fake electrons, residual of conversion electrons, $b\bar{b}$ events and fake J/ψ are estimated, as shown in Table 6.1 and Figure 6.1. Additional background contribution of J/ψ-electron pair from prompt source (zero lifetime) is to be estimated from the lifetime fitting which is described in the following sections.

6.1 B_c^+ meson lifetime measurement

The decay length of the B_c^+ meson, L_{xy}, is defined as the distance in the transverse plane between its decay vertex and its production point. We assume that the B_c^+ meson is produced at the primary vertex. We then relate the decay length to the Lorentz-invariant proper decay length, ct, by a Lorentz boost $\beta\gamma$,

$$ct = \frac{L}{\beta\gamma} = L_{xy} \cdot \frac{M_{B_c}}{p_{T_{B_c}}} \tag{6.1}$$

where L is the three-dimensional decay length, M_{B_c} is the B_c^+ mass and $p_{T_{B_c}}$ is the transverse momentum of B_c^+.

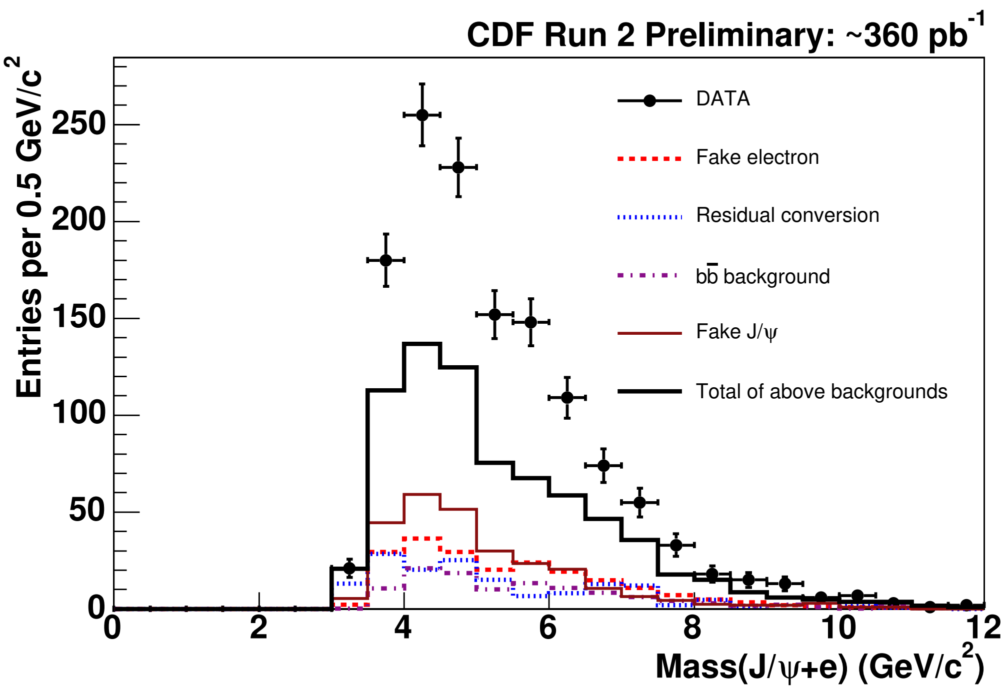

Figure 6.1: Invariant mass distribution of J/ψ-electron candidates from data (black points with error bars) and background contributions from fake electrons (red dashed lines), conversion electrons (blue dashed lines), $b\bar{b}$ (purple dot-dashed lines) and fake J/ψ (brown solid lines), the sum of these (solid black line). The sum does not include the prompt background contribution which is to be estimated using lifetime fitting.

Since we do not fully reconstruct the B_c^+ due to the undetectable neutrino in CDF, we cannot calculate the B_c^+ momentum directly. So we use the pseudo-proper decay lengh, x, instead of the proper decay length, ct. The pseudo-proper decay length is defined as

$$x \equiv L_{xy} \cdot \frac{M_{J/\psi e}}{p_{T_{J/\psi e}}} = ct/K, \tag{6.2}$$

where K is a correction factor and defined as

$$K \equiv \frac{p_{T_{J/\psi e}}}{p_{T_{B_c}}} \cdot \frac{M_{B_c}}{M_{J/\psi e}}. \tag{6.3}$$

An unbinned maximum likelihood fitting method is used to extract the B_c^+ lifetime from the data. The pseudo-proper decay length, x, and its error, σ, are the input variables. The signal function is assumed to be a pure exponential lifetime distribution, convoluted first with a Gaussian resolution function and next with the K factor distribution $H(K)$ obtained from Monte Carlo,

$$\mathcal{F}_s(x, \sigma) = \int \left[H(K) \left(\frac{K}{c\tau} \right) \theta(x) \exp\left(-\frac{xK}{c\tau} \right) \otimes G(x, s\sigma) \right] dK \tag{6.4}$$

$M_{J/\psi e}$(GeV/c^2)	3-4	4-6	6-7	7-12	total (3-12)
$J/\psi e$ data	201	783	183	153	1320
Fake J/ψ	50.0	164.0	31.0	22.5	267.5
	±5.0	±9.1	±3.9	±3.4	±11.6
Fake electron	31.7	110.2	34.1	32.1	208.1
	±0.5	±1.0	±0.5	±0.4	±1.3
	±5.5	±19.0	±5.8	±5.2	±35.5
Conversion electron	41.5	67.4	20.9	22.2	152.0
	±8.0	±10.9	±5.0	±5.1	±15.3
	±22.9	±33.0	±9.2	±10.8	±75.8
$b\bar{b}$	10.6	63.0	19.2	20.9	113.8
	±1.2	±3.0	±1.6	±1.7	±4.0
	±3.7	±18.2	±4.3	±4.7	±30.7

Table 6.1: J/ψ-electron candidates counting and partial background estimations in several $M_{J/\psi e}$ bins. Events with $4 < M_{J/\psi e} < 6$ GeV/c^2 is to be used for lifetime measurement. The contribution from prompt background is missing and to be estimated with lifetime fitting procedure.

where s is an overall error scale factor which represents the possible amount we under-estimate the error. The $\theta(x)$ is the step function defined as $\theta(x) = 1$ for $x \geq 0$ and $\theta(x) = 0$ for $x < 0$.

Figures 6.2 and 6.3 show the K-factor distributions obtained using Monte Carlo which generates only $B_c^+ \to J/\psi e^+ \nu_e$ signal events with the B_c^+ p_T spectrum from a theoretical calculation [62]. The B_c^+ meson mass and lifetime in the generator are chosen to be 6.271 GeV/c^2 and 0.55 ps, respectively. The selection cuts described earlier are applied to obtain the K distribution, $H(K)$. As one can see in Figure 6.3, the shape of the $H(K)$ depends strongly on the values of the invariant mass $M_{J/\psi e}$. We use K distributions estimated in four different $M_{J/\psi e}$ bins.

We consider the following background sources in the lifetime fitting process; fake J/ψ, fake electron, residual conversion electron, $b\bar{b}$ contamination and random combinations from QCD prompt background. The size of the QCD prompt background, assumed to have a lifetime distribution as a Gaussian resolution function, is to be determined in the lifetime fitting process. The sizes of other backgrounds are determined in the signal counting process as listed in Table 6.1 and their values and errors are used as a initial input values in the fitting procedure. The distributions of pseudo-proper decay length for these backgrounds are determined using the background samples and parameterized in a general function composed of five parts representing the zero lifetime component, two positive-sloped exponential functions (positive lifetimes) and two negative-sloped exponential functions (negative lifetimes),

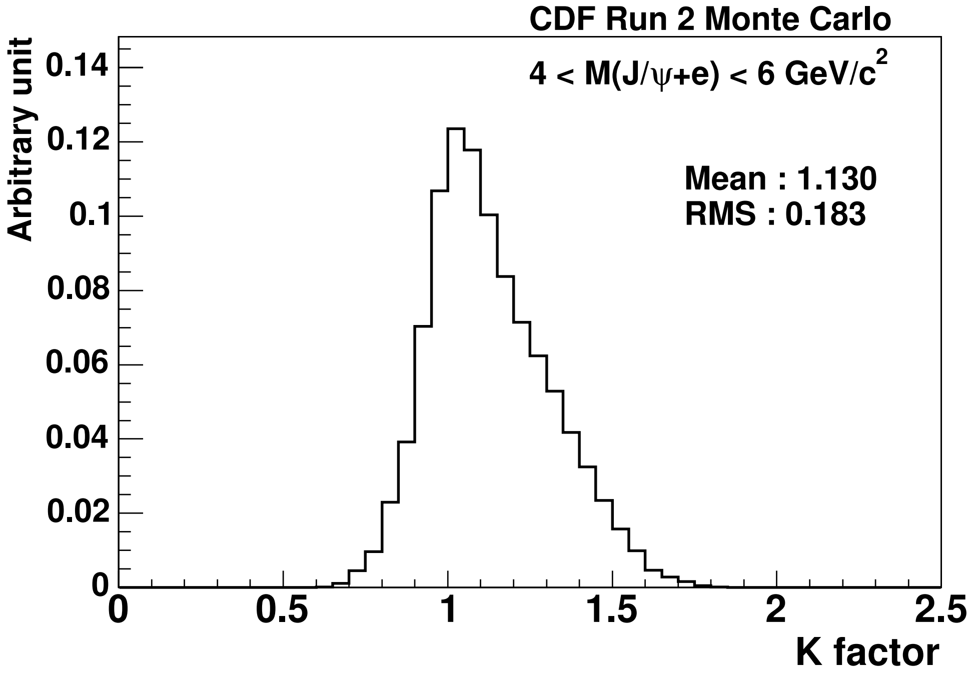

Figure 6.2: Distribution of K factor. All events in $4 < M_{J/\psi e} < 6$ GeV/c^2 are included.

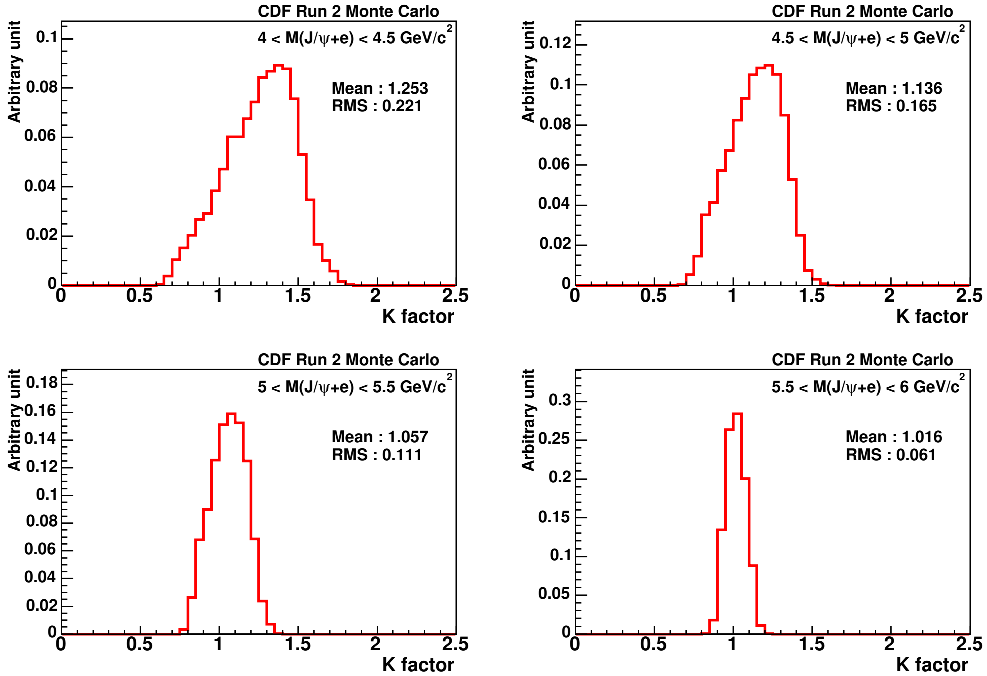

Figure 6.3: Distributions of K factor in four different $M_{J/\psi e}$ bins.

$$
\begin{aligned}
\mathcal{F}_b(x,\sigma) = \quad & (1 - f_{p1} - f_{p2} - f_{m1} - f_{m2})G(x, s\sigma) \\
& + \frac{f_{p1}}{\lambda_{p1}}\theta(x)\exp(-\frac{x}{\lambda_{p1}}) \otimes G(x, s\sigma) \\
& + \frac{f_{p2}}{\lambda_{p2}}\theta(x)\exp(-\frac{x}{\lambda_{p2}}) \otimes G(x, s\sigma) \\
& + \frac{f_{m1}}{\lambda_{m1}}\theta(-x)\exp(\frac{x}{\lambda_{m1}}) \otimes G(x, s\sigma) \\
& + \frac{f_{m2}}{\lambda_{m2}}\theta(-x)\exp(\frac{x}{\lambda_{m2}}) \otimes G(x, s\sigma). \qquad (6.5)
\end{aligned}
$$

This general form of function is tried initially for all the background samples. The fitting resulted that not all of the terms are needed, so unnecessary terms are omitted in the final background parameterizations as discussed in detail below.

6.1.1 Fake electron background

The pseudo-proper decay length distribution for fake electron with real J/ψ events is extracted using the J/ψ+track data sample. The event selection is the same as that for J/ψ-electron but there is no requirement for the track to be identified as an electron by the $\mathcal{P}_e$ cut. The J/ψ+track candidate events are multiplied by the p_T-dependent fake electron rates to obtain the pseudo-proper decay length distribution as shown in Figure 6.4. The fake J/ψ pseudo-proper decay length distribution obtained from J/ψ mass sideband events ($\mid M(\mu\mu) - 3096.87 \pm 10 \times 15$ MeV$/c^2 \mid< 50$ MeV$/c^2$), is shown in Figure 6.5. The parameterization of the pseudo-proper decay length distribution for fake electron with real J/ψ is obtained from a simultaneous fitting to both J/ψ peak ($\mid M(\mu\mu) - 3096.87$ MeV$/c^2 \mid< 50$ MeV$/c^2$) and sideband candidates using a likelihood function as:

$$
\mathcal{F} \quad = \quad f_{J/\psi}\mathcal{F}_{fake-e} + (1 - f_{J/\psi})\mathcal{F}_{fake-J/\psi} + G(f_{J/\psi} - f^{mass}_{J/\psi}, \sigma^{mass}_{f_{J/\psi}}), \qquad (6.6)
$$

where $\mathcal{F}_{fake-e}$ is probability density function for fake electron with real J/ψ events, and $\mathcal{F}_{fake-J/\psi}$ is for fake electron with fake J/ψ events, which have a form of the general background function in Equation 6.5. The fraction of real J/ψ events, $f_{J/\psi}$, is constrained to a Gaussian distribution using a value ($f^{mass}_{J/\psi}$) and its error ($\sigma^{mass}_{f_{J/\psi}}$) obtained from the J/ψ mass distribution fitting. The parameterization results are listed as input values for the final fitting in Table 6.2. We check the fit quality by calculating the fit probability from the χ^2 between the data points and the fit projection. In the χ^2 calculation, un-equal binning is used to ensure that the contents in each bin are more than 20. The fit probability is derived from χ^2, the sum of the differences between fit projections and data points, and the number of bins as the number of degrees of freedom.

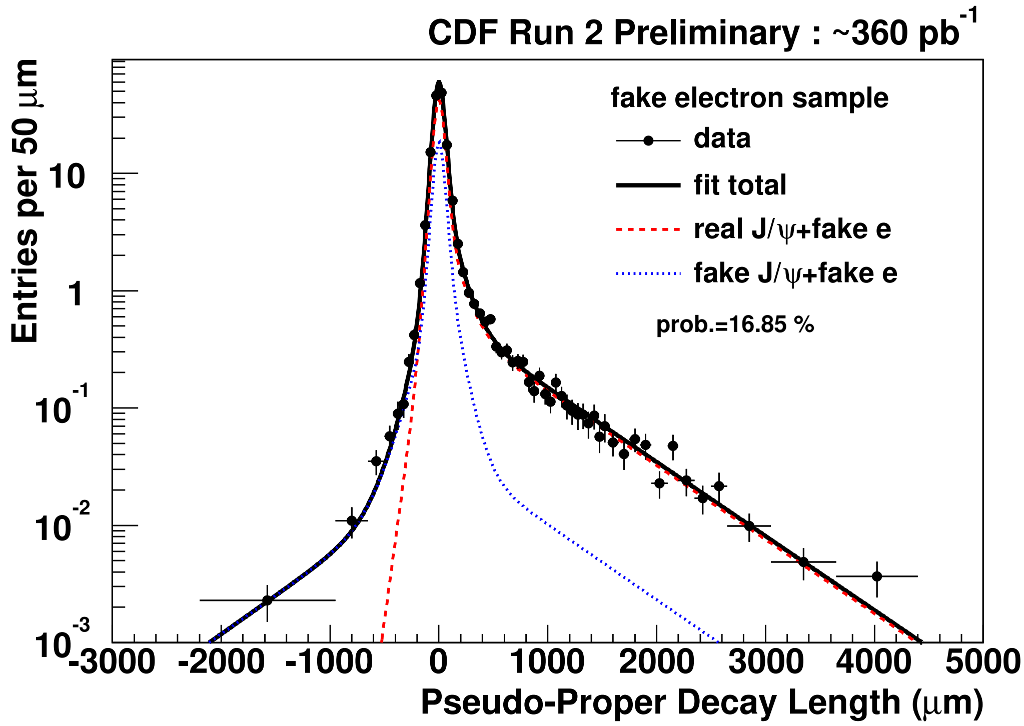

Figure 6.4: The pseudo-proper decay length distribution for J/ψ+fake-electron pairs passing the same cut as J/ψ-electron. The events are obtained using J/ψ+track pairs with J/ψ in the J/ψ mass peak window. Each pair is re-weighted according the electron fake probability which is a function of the track p_T. The black dots with error bars are from data, the blue dashed-line is the shape of fake J/ψ estimated using sideband di-muon events, and the red-dashed line is the pseudo-proper decay length shape from real J/ψ with fake electrons.

6.1.2 Fake J/ψ background

The J/ψ mass sideband events from the J/ψ+track sample and the J/ψ-electron candidate events give a consistent parameterization of the pseudo-proper decay length distribution. For the fake J/ψ background shape, we use the parameters obtained from the J/ψ+track sample for higher statistics. The results are listed in Table 6.2 and shown in Figure 6.5.

6.1.3 Residual conversion electron background

In selecting J/ψ-electron candidate events, we excluded electrons identified as those from photon conversion decay using a specific conversion finding algorithm described in section 3.4.1. The algorithm is not 100% efficient due to the limited kinematic and geometric coverage, so some conversion electrons called residual conversion electrons remain in the J/ψ-electron candidates. The size of this residual conversion electron background is estimated using the conversion finding efficiency calculated in a Monte Carlo simulation together with the tagged (excluded) conver-

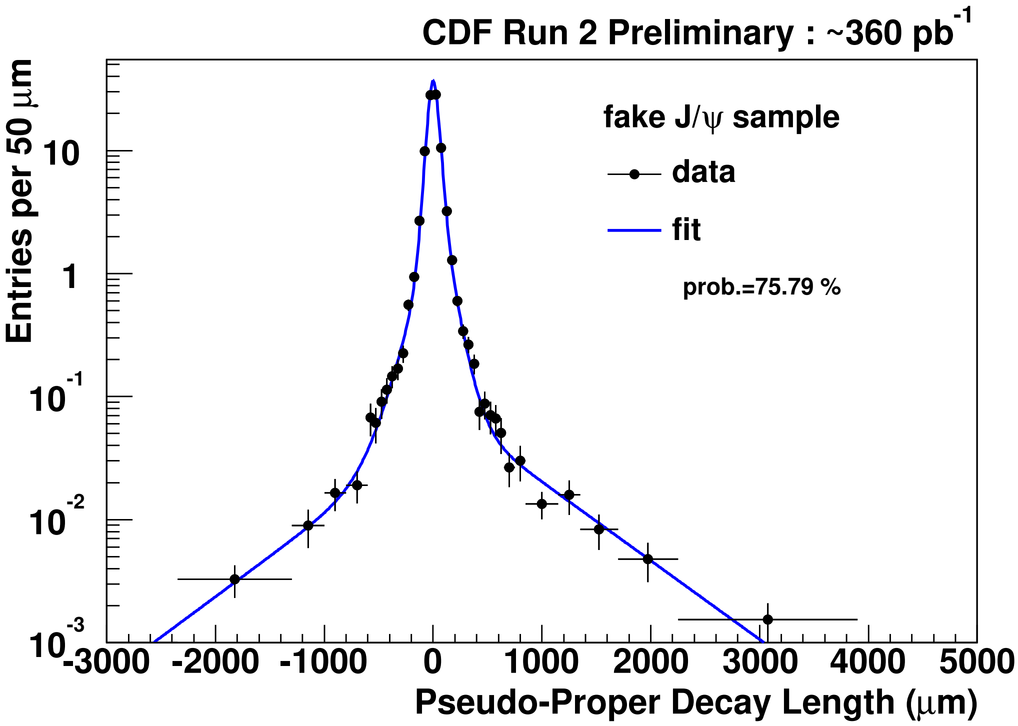

Figure 6.5: The pseudo-proper decay length distribution for fake J/ψ+track candidates. The J/ψ candidates are required to be in the J/ψ mass sideband window.

sion electrons. We assume that the pseudo-proper decay length distributions of the residual conversion electrons and the tagged conversion electrons are the same and use the tagged conversion electron events to obtain the parameterization of this background. Error scaling factor is constrained using that of the J/ψ+track sample. The fitting result is shown in Figure 6.6 and in Table 6.2. The fitting resulted that we only need a single positive lifetime function together with a prompt function to describe this background shape.

6.1.4 $b\bar{b}$ background

The pseudo-proper decay length distribution for the $b\bar{b}$ background is estimated using Pythia Monte Carlo sample [87] generated with a mix of the three dominant $b\bar{b}$ production diagrams. The relative fractions of flavor creation (FC) process, flavor excitation process (FE) and gluon splitting (GS) are taken from the default Pythia setting for Run-II [88]. The contributions from these three processes after the event reconstruction and the B_c^+ selection are found to be 3.6 ± 0.7 events (FC), 16.5 ± 1.3 events (FE) and 42.9 ± 2.6 events (GS), respectively. The normalization of these events is obtained comparing to the measured $B^+ \to J/\psi K^+$ yield in a similar method used in the B_c^+ production cross section measurement. The parameterization of these $b\bar{b}$ distribution is simply two lifetimes convoluted with a Gaussian resolution function

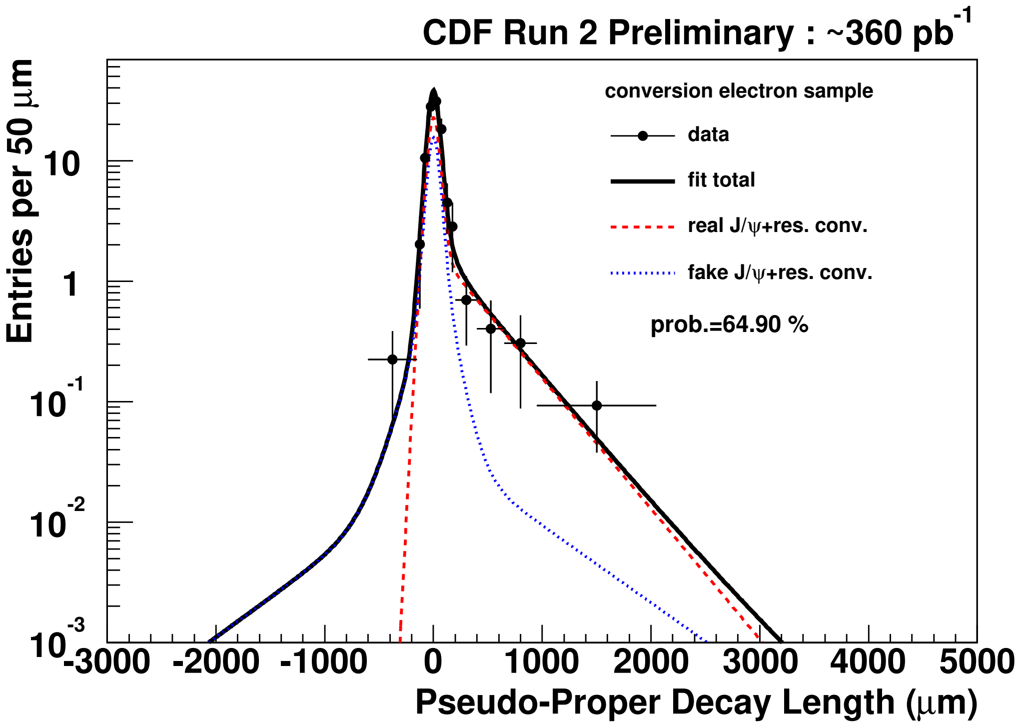

Figure 6.6: The pseudo-proper decay length distribution for J/ψ+conversion electron pairs passing the same cut as J/ψ-electron. The black dots with error bars are from data, the blue dashed-line is the shape of fake J/ψ estimated using sideband di-muon events, and the red-dashed line is the pseudo-proper decay length shape from real J/ψ with fake electrons.

with no prompt contribution. The result is shown in Figure 6.7 and Table 6.2.

6.2 Lifetime fitting result

The pseudo-proper decay length distribution of the J/ψ-electron candidates is assumed to have the following functional form,

$$\begin{aligned}
\mathcal{F} &= (1 - f_{fake-e} - f_{fake-J/\psi} - f_{conv-e} - f_{b\bar{b}} - f_{prompt}) \cdot \mathcal{F}_s \\
&+ f_{fake-e} \cdot \mathcal{F}_{fake-e} + f_{fake-J/\psi} \cdot \mathcal{F}_{fake-J/\psi} + f_{conv-e} \cdot \mathcal{F}_{conv-e} \\
&+ f_{b\bar{b}} \cdot \mathcal{F}_{b\bar{b}} + f_{prompt} \cdot G(x, s\sigma), \qquad (6.7)
\end{aligned}$$

where f_{fake-e} and $\mathcal{F}_{fake-e}$ are the background fractions and pseudo-proper decay length distributions for fake electron, $f_{fake-J/\psi}$ and $\mathcal{F}_{fake-J/\psi}$ are for fake J/ψ, f_{conv-e} and $\mathcal{F}_{conv-e}$ are for conversion electron, and $f_{b\bar{b}}$ and $\mathcal{F}_{b\bar{b}}$ are for $b\bar{b}$. They are estimated using the background samples as described before. The prompt background is assumed to have zero lifetime with a Gaussian resolution function and its fraction (f_{prompt}) is determined from the lifetime fitting of

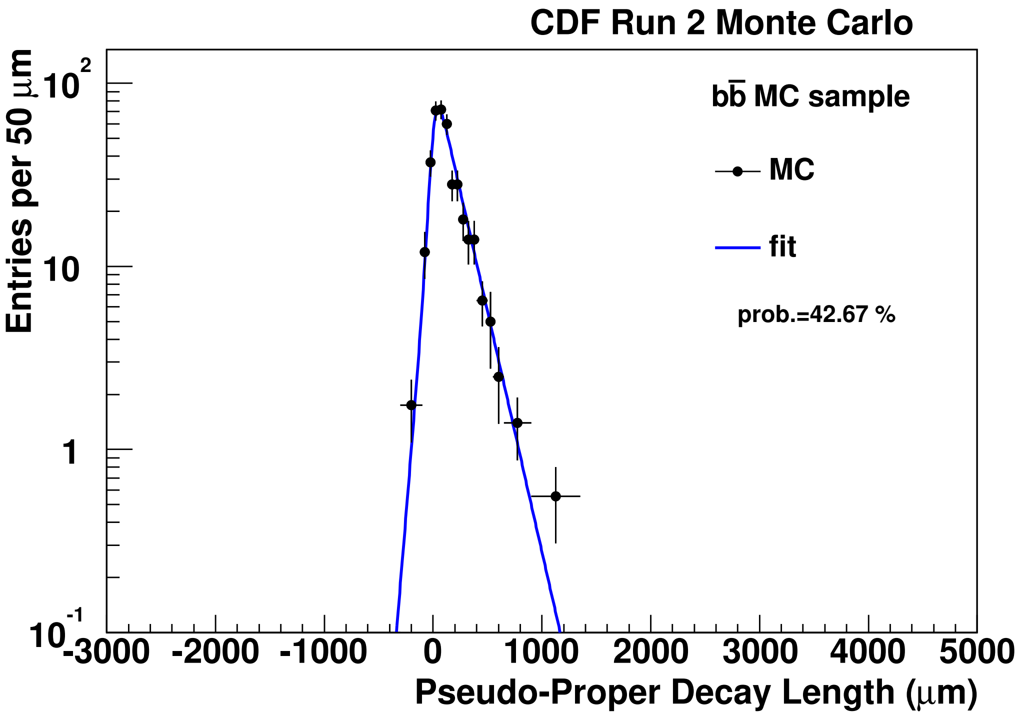

Figure 6.7: The pseudo-proper decay length distribution for the $b\bar{b}$ background.

J/ψ-electron candidates.

An unbinned maximum likelihood fitting is performed using the log-likelihood with the background fractions and the distributions constrained to the parameter values obtained from the fittings of the background samples:

$$\ell n\mathcal{L} = \sum_{i=1}^{N_{J/\psi+e}} \ell n\mathcal{F} - \sum_{j=1}^{24} \frac{1}{2}(f^j_{BG} - \langle f^j_{BG}\rangle)^2/\sigma^2_{f^j_{BG}}, \tag{6.8}$$

where the $\langle f^j_{BG}\rangle$ and $\sigma_{f^j_{BG}}$ are the input values and their Gaussian errors. Error scaling factor is also constrained using that of the J/ψ+track sample. There are total 24 Gaussian constraints in the likelihood as listed in Table 6.2.

Finally the fitting is performed on the 783 J/ψ-electron candidates and the lifetime of the B_c^+ meson is extracted to be $c\tau_{B_c} = 142.1\ ^{+21.9}_{-19.7}\ \mu$m. The fitting results are shown in Figure 6.8, 6.9, and Table 6.2.

Using the fitting result, we also estimate that the contribution of the prompt background is 127 ± 40 events. Adding all background together, we estimated 546 ± 54 background events in the 783 J/ψ-electron candidates. In Figure 6.10, the invariant mass distribution of the total background including prompt source and the expected B_c^+ signal are shown. The fractions of backgrounds are returned from the lifetime fitting. The prompt background invariant mass shape, added in Figure 6.10, is obtained using the J/ψ+track sample with very negative decay length 3σ away from zero, $L_{xy}/\sigma_{L_{xy}} < -3$.

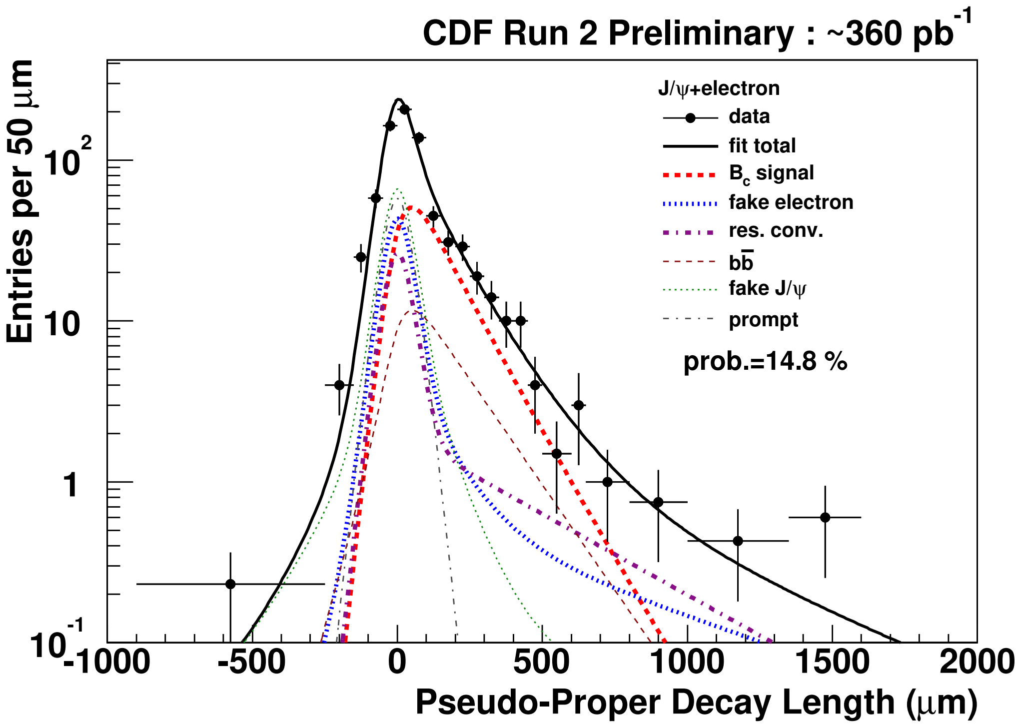

Figure 6.8: The pseudo-proper decay length distributions for J/ψ-electron candidates together with B_c^+ signal (red dashed lines) and individual background contributions.

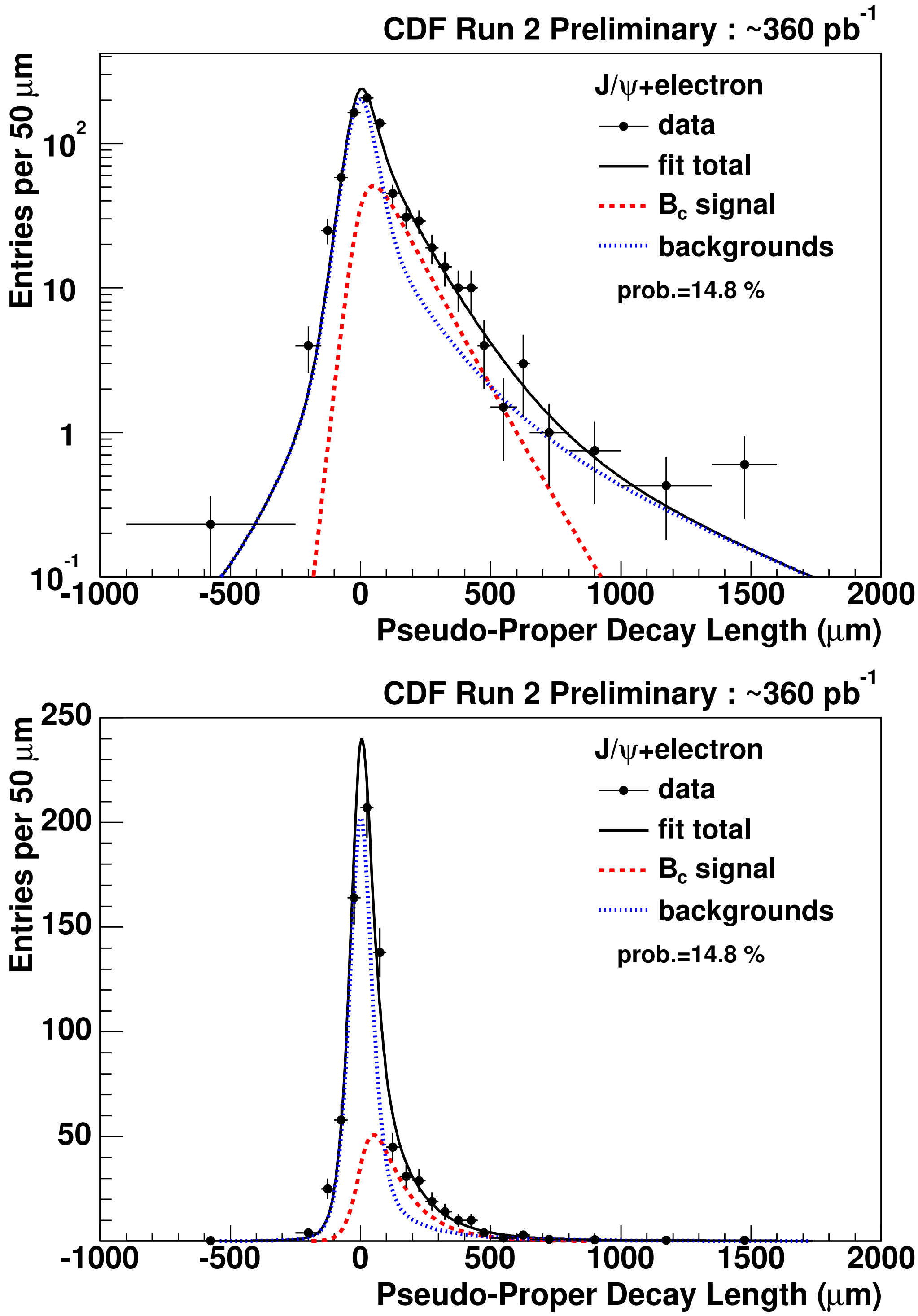

Figure 6.9: The pseudo-proper decay length distributions for J/ψ-electron candidates together with B_c^+ signal (red dashed lines) and total background (blue dotted lines) in log scale for top plot and in linear scale for bottom plot.

Table 6.2: B_c^+ Lifetime fitting result. The unit for $c\tau_{B_c}$ and λ is μm.

Variable description	Symbol	Input values	Fitting returns
B_c^+ lifetime	$c\tau_{B_c}$	-	$142.1\ ^{+21.9}_{-19.7}$
Error scale	s	$1.3450\ ^{+0.0096}_{-0.0098}$	1.3476 ± 0.0096
Prompt BKG fraction	f^{prompt}	-	$0.163\ ^{+0.051}_{-0.053}$
Fake-e BKG fraction	f^{fake-e}	0.141 ± 0.022	0.144 ± 0.022
Conv.-e BKG fraction	f^{conv-e}	0.086 ± 0.041	0.094 ± 0.038
$b\bar{b}$ BKG fraction	$f^{b\bar{b}}$	0.080 ± 0.022	0.086 ± 0.022
Fake-J/ψ BKG fraction	$f^{fake-J/\psi}$	0.209 ± 0.012	0.211 ± 0.012
Fake-e positive lifetime fraction	f_{p1}^{e}	0.100 ± 0.007	0.100 ± 0.007
Fake-e positive lifetime	λ_{p1}^{e}	$117.2\ ^{+15.2}_{-14.1}$	117.2 ± 14.6
Fake-e positive lifetime fraction	f_{p2}^{e}	0.076 ± 0.006	0.076 ± 0.006
Fake-e positive lifetime	λ_{p2}^{e}	$688.4\ ^{+35.7}_{-32.6}$	$687.3\ ^{+34.0}_{-33.9}$
Fake-e negative lifetime fraction	f_{m1}^{e}	$0.032\ ^{+0.010}_{-0.008}$	0.034 ± 0.009
Fake-e negative lifetime	λ_{m1}^{e}	$64.6\ ^{+17.4}_{-12.1}$	$66.3\ ^{+13.8}_{-13.9}$
Fake-J/ψ positive lifetime fraction	$f_{p1}^{J/\psi}$	$0.106\ ^{+0.008}_{-0.007}$	0.106 ± 0.007
Fake-J/ψ positive lifetime	λ_{p1}	$87.3\ ^{+6.9}_{-6.5}$	87.2 ± 6.7
Fake-J/ψ positive lifetime fraction	$f_{p2}^{J/\psi}$	0.013 ± 0.002	0.013 ± 0.002
Fake-J/ψ positive lifetime	$\lambda_{p2}^{J/\psi}$	$678.6\ ^{+80.0}_{-68.4}$	$677.3\ ^{+73.5}_{-73.4}$
Fake-J/ψ negative lifetime fraction	$f_{m1}^{J/\psi}$	0.007 ± 0.002	0.007 ± 0.002
Fake-J/ψ negative lifetime	$\lambda_{m1}^{J/\psi}$	$662.1\ ^{+118.9}_{-94.3}$	$657.3\ ^{+104.7}_{-104.0}$
Fake-J/ψ negative lifetime fraction	$f_{m2}^{J/\psi}$	0.059 ± 0.005	0.060 ± 0.005
Fake-J/ψ negative lifetime	$\lambda_{m2}^{J/\psi}$	$122.7\ ^{+12.9}_{-13.4}$	$122.7\ ^{+12.9}_{-12.8}$
Conv-e positive lifetime fraction	f_{p1}^{conv}	$0.225\ ^{+0.083}_{-0.069}$	0.235 ± 0.072
Conv-e positive lifetime	λ_{p1}^{conv}	$401.1\ ^{+172.1}_{-117.3}$	$431.4\ ^{+112.0}_{-108.4}$
$b\bar{b}$ positive lifetime fraction	$f_{p1}^{b\bar{b}}$	$0.936\ ^{+0.034}_{-0.035}$	0.921 ± 0.034
$b\bar{b}$ positive lifetime	$\lambda_{p1}^{b\bar{b}}$	$165.5\ ^{+11.1}_{-10.3}$	165.6 ± 10.7
$b\bar{b}$ negative lifetime	$\lambda_{m1}^{b\bar{b}}$	$59.8\ ^{+35.0}_{-15.6}$	$66.1\ ^{+18.6}_{-20.7}$

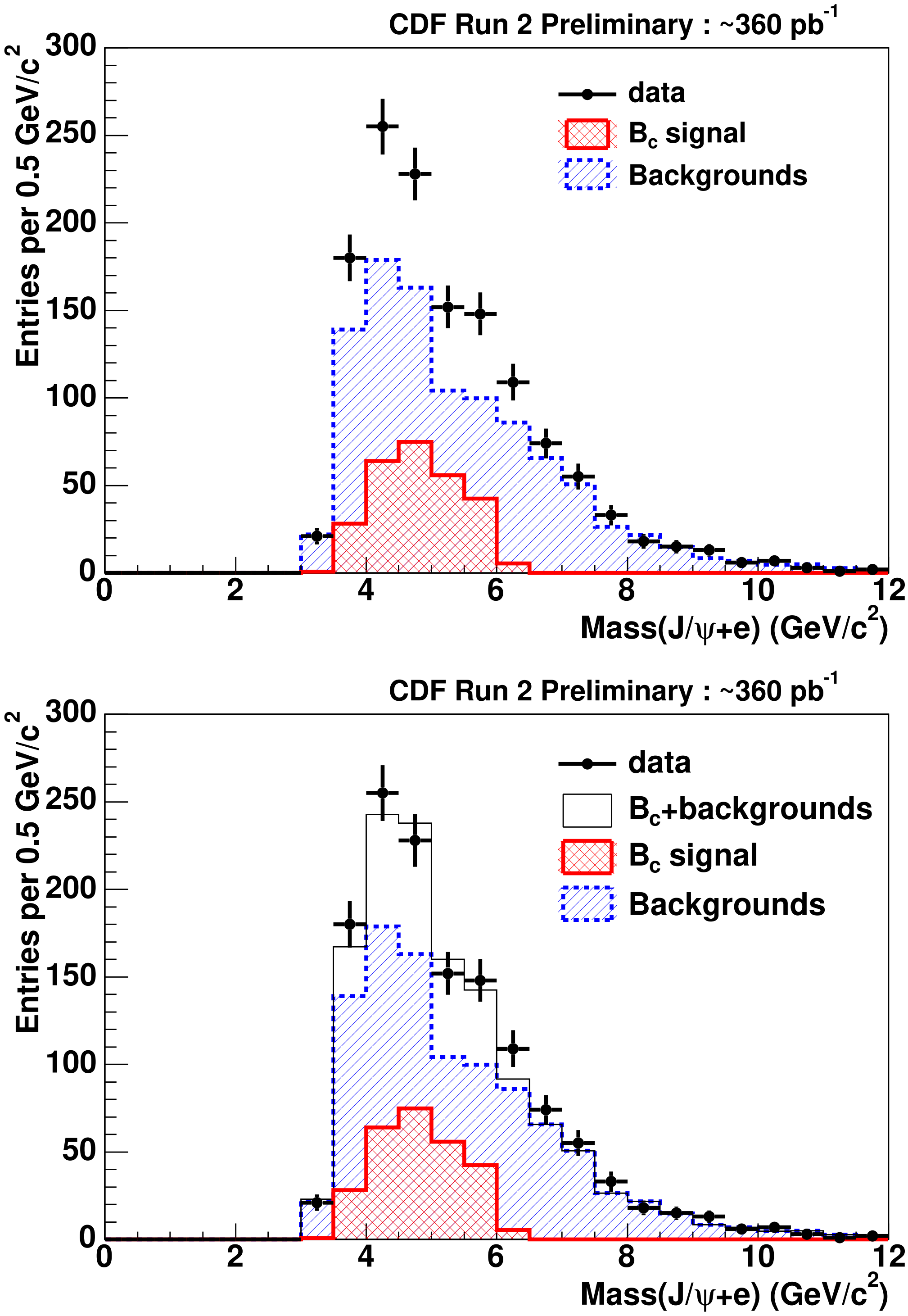

Figure 6.10: Invariant mass distribution of J/ψ-electron for data. The total background and the expected B_c^+ signal are also shown.

6.3 Systematic uncertainties

We examine three sources of the systematic uncertainties, K-factor estimation, background distributions and decay length resolution function.

6.3.1 K-factor estimation

The distribution of K-factor is obtained using a Monte Carlo simulation with the mass and lifetime of the B_c^+ meson set to be 6.271 GeV/c^2 and 0.55 ps, respectively. We vary the B_c^+ meson mass from 6.2 to 6.4 GeV/c^2 to estimate the uncertainty on the K-factor distribution. The change of the fitted B_c^+ lifetime in data is within 1.7 μm using the various K-factor distributions with different B_c^+ meson masses. The Monte Carlo B_c^+ lifetime is also varied by ± 0.15 ps from 0.4 to 0.7 ps to evaluate the variation of K-factor. The change is within 0.2 μm for these K-factor distributions. We also vary the assumed B_c^+ p_T spectrum by using the B cross section result from Run-II CDF measurement [17] replacing that from a theoretical prediction [62]. The change of B_c^+ lifetime fitting result is within 1.3 μm.

The effects on K factor distribution for semileptonic B_c^+ decay channels, $B_c^+ \to J/\psi e^+ \nu_e X$ where X denotes other decay products, are estimated by generating a Monte Carlo sample with a mixture of B_c^+ semileptonic decay channels. The effective branching fraction of B_c^+ semileptonic decays with J/ψ-electron pairs in the final states other than the $B_c^+ \to J/\psi e^+ \nu_e$ channel is about 11.64 % from a theoretical prediction [45]. To estimate systematic uncertainty on K-factor, we double the amount of the non-exclusive decays in the Monte Carlo decay table. Using the new K-factor distribution in the data fitting, the change of 1.6 μm on the B_c^+ lifetime is found.

Finally, the effect of CDF di-muon trigger condition is simulated. The difference on lifetime fitting result between using the K-factor distributions with and without the trigger simulation is found to be ± 0.3 μm.

Adding all above changes in quadrature, we assign a systematic error of ± 2.7 μm from uncertainties related with K-factor estimation, as listed in Table 6.3.

6.3.2 Background shapes

The systematic uncertainties from background shapes are estimated using background function parameters obtained with alternative methods. A new set of parameters of fake electron distribution is obtained by fitting the J/ψ+track sample directly without applying the p_T-dependent fake electron rate. The pseudo-proper decay length distribution for the J/ψ+track sample is very similar to that for the J/ψ+fake-electron. So the resulting parameters of the new fake electron shape are consistent with those listed in Table 6.2 and the change of the B_c^+ lifetime is found to be -1.5 μm.

The pseudo-proper decay length distribution for the fake J/ψ events is obtained using the high statistics J/ψ+track sideband events and we use an alternative set of parameters obtained using J/ψ-electron sideband events as a check of systematic uncertainty. Using the new fake J/ψ distribution from J/ψ-electron sideband events, the change on the fitted B_c^+ lifetime is found to be -6.1 μm.

Similar to the fake electron background shape, we remove the p_T-dependent conversion-finding efficiency and use the tagged conversion-electron sample directly to obtain an alternative shape of residual conversion-electron background. The changes of the shapes are small, and the effect on the fitted B_c^+ lifetime result is -0.9 μm. Another effect on the residual-electron shape is the fake J/ψ shape assumed in the parameter fitting process. We vary this by using the J/ψ sideband events in the J/ψ+conversion-electron sample and the effect on B_c^+ lifetime is found to be $+2.7$ μm.

The relative fractions of $b\bar{b}$ background from the three diagrams in the default Run-II PYTHIA setting (CTEQ5L and initial state radiation parameter PARP(67)=4) are 19.2%/50.9%/29.9% (GS/FE/FC). After event selection cuts for B_c^+ semileptonic decays, the remaining background fractions from the three sources are 70%/25%/5% (GS/FE/FC), as shown in Figure 6.11. These are the fractions to mix the pseudo-proper decay length distributions in our default fitting. We examine the variations from different PYTHIA setting and from a data-MC comparison study done in Run-I B-$\bar{B}$ correlation study [88], The maximum variation was found to be from 90%/0%/10% to 25%/73%/2% (GS/FE/FC), after taking into account our event selection efficiency. Taking this variation in consideration, we estimate the uncertainties on the background shape by dramatically changing the default fractions. At the re-fitting, we fix all other background shapes and normalizations. The change of the fitted B_c^+ lifetime is $+8.1$ μm if all $b\bar{b}$ background is assumed to be from 100% flavor-excitation source and -3.8 μm if 100% gluon-splitting source.

We also force the error scaling factor from the Monte Carlo sample with our default settings to be unity to estimate the systematic effect from this source. The difference on the fitted B_c^+ lifetime is -1.2 μm using the $b\bar{b}$ shape obtained using unity error scaling factor.

Adding all above changes in quadrature, we assign $(+8.5, -7.5)$ μm to systematic uncertainties related with the background pseudo-proper decay length distributions, as listed in Table 6.3.

6.3.3 Decay length resolution

We use several alternative functional forms to estimate the systematic uncertainties related with the assumed single Gaussian resolution function. The variations include adding the second Gaussian with same mean as the first Gaussian but with a larger width, and two extra symmetric exponential tails to the resolution function. The new parameters of the resolution functions are obtained in the higher statistics J/ψ+track sample, and are fixed in the B_c^+ lifetime fitting procedure. The difference on the fitted B_c^+ lifetime value is found to be -5.6 μm using these new resolution functions.

We also look at the so-called “Punzi effect” [97] by adding extra probability density functions

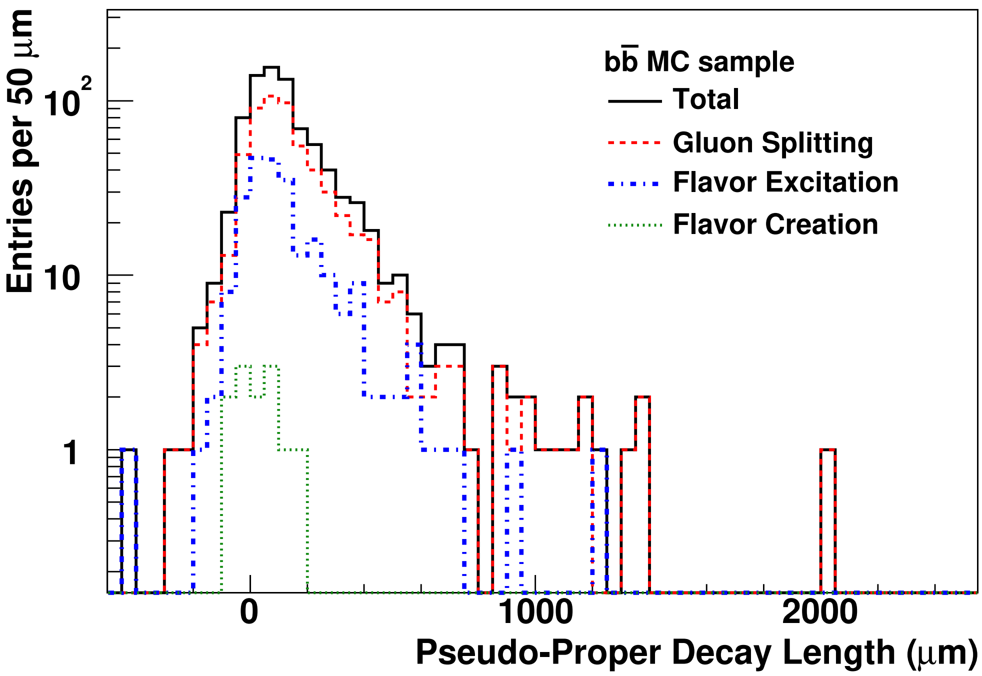

Figure 6.11: The pseudo-proper decay length distributions for the $b\bar{b}$ background from gluon splitting (red dashed lines), flavor excitation (blue dot-dashed lines) and flavor creation (green dotted lines). The black lines are the sum of the three using a predicted ratio of 70/25/5.

Table 6.3: Systematic uncertainty effect on B_c^+ lifetime fitting

Catalog	Description	Fitted $c\tau$ (μm)	$\Delta c\tau$ (μm)
K-factor	$M_{B_c} = 6.4,\ 6.2$ GeV/c^2	$140.4\ ^{+21.7}_{-19.5}$, $143.0\ ^{+22.0}_{-19.8}$	± 1.7
K-factor	$\tau_{B_c} = 0.4,\ 0.7$ ps	$141.9\ ^{+21.9}_{-19.6}$	± 0.2
K-factor	$H_b \to J/\psi X$ spectrum	$140.8\ ^{+21.7}_{-19.5}$	± 1.3
K-factor	$B_c^+ \to J/\psi e^+ \nu_e X$	$140.5\ ^{+21.7}_{-19.5}$	± 1.6
K-factor	Trigger simulation	$142.4\ ^{+21.9}_{-19.7}$	± 0.3
			K-factor sub-total $\Delta c\tau = \pm 2.7$
$\mathcal{F}_{fake-e}$	Use J/ψ+trk shape directly	$140.6\ ^{+21.5}_{-19.4}$	-1.5
$\mathcal{F}_{fake-J/\psi}$	Use $J/\psi + e$ sideband	$136.0\ ^{+24.8}_{-22.6}$	-6.1
$\mathcal{F}_{conv-e}$	Use tagged conv-e shape directly	$141.2\ ^{+21.7}_{-19.5}$	-0.9
$\mathcal{F}_{conv-e}$	Use J/ψ+conv-e sideband	$144.8\ ^{+21.5}_{-19.3}$	$+2.7$
$\mathcal{F}_{b\bar{b}}$	Use FE only	$150.2\ ^{+17.5}_{-15.9}$	$+8.1$
$\mathcal{F}_{b\bar{b}}$	Use GS only	$138.3\ ^{+16.6}_{-15.0}$	-3.8
$\mathcal{F}_{b\bar{b}}$	No error scaling in MC	$140.9\ ^{+21.6}_{-19.5}$	-1.2
			Background shapes sub-total $\Delta c\tau = (+8.5, -7.5)$
L_{xy} resolution	Extra Gaussian/Symmetric exponential	$137.0\ ^{+21.9}_{-19.8}$, $136.5\ ^{+21.9}_{-19.8}$	-5.6
L_{xy} resolution	Punzi effect	$137.3\ ^{+22.1}_{-19.4}$	-4.8
L_{xy} resolution	Silicon alignment		± 1
			L_{xy} resolution sub-total $\Delta c\tau = (+1.0, -7.4)$
			Total systematic error $\Delta c\tau = (+9.0, -10.9)$

of pseudo-proper decay length error distributions for the fake J/ψ, fake electron, conversion electrons and remaining signals. The change of the B_c^+ lifetime after adding the extra probability density functions is found to be -4.8 μm. We also assign a systematic uncertainty of ± 1 μm for possible SVX mis-alignment following other CDF lifetime measurements.

In total, we assign a systematic uncertainty of $(+1.0, -7.4)$ μm on the fitted B_c^+ lifetime due to uncertainties related with the decay length resolution and its modeling, as listed in Table 6.3.

The total systematic uncertainty is found to be $(+9.0, -10.9)$ μm after adding all the systematic errors listed in Table 6.3. We quote a symmetric uncertainty of ± 10 μm by taking an average of the two uncertainties.

In summary, the extracted B_c^+ lifetime is $142\ ^{+22}_{-20} \pm 10$ μm or $0.474\ ^{+0.073}_{-0.066} \pm 0.033$ ps, where the first uncertainty is statistical and the second is systematic.

Chapter 7

Conclusion

We measured the B_c^+ meson lifetime in $B_c^+ \to J/\psi e^+ \nu_e$ channel using 360 pb^{-1} of data collected between February 2002 and August 2004 with the CDF II detector. The B_c^+ signal candidates were reconstructed from J/ψ-electron pairs with a displaced vertex. The J/ψ candidates were reconstructed from data sample of $J/\psi \to \mu^+\mu^-$ trigger. Electrons were reconstructed using a track-based reconstruction algorithm to increase the efficiency in low p_T region. Electron identification used both specific ionization energy deposit and calorimeter shower information. We chose a broad invariant mass range, $4 < M_{J/\psi e} < 6$ GeV/c^2, as our search window due to missing neutrino, where $M_{J/\psi e}$ is the invariant mass of the J/ψ and electron pair.

Before measuring the B_c^+ lifetime, we first examined the excess of B_c^+ signal over the background events. The prompt J/ψ background was removed by $L_{xy}/\sigma_{L_{xy}} > 3$ cut. Then a signal excess of 115 was observed above the background events of 63±4.9±13.4, where the first uncertainty is statistical and the second one is systematic. The probability of such background to fluctuate to the size of signal candidate events is 3.2×10^{-9} which corresponds to a significance of 5.9σ. We calculated the B_c^+ production cross section times branching fraction for $B_c^+ \to J/\psi e^+ \nu_e$ decay relative to that of the $B^+ \to J/\psi K^+$ channel in the kinematic range of $p_{T_B} > 4$ GeV/c and the rapidity $\mid y_B \mid < 1$,

$$\frac{\sigma(B_c^+) \cdot \mathcal{B}(B_c^+ \to J/\psi e^+ \nu_e)}{\sigma(B^+) \cdot \mathcal{B}(B^+ \to J/\psi K^+)} = 0.282 \pm 0.038 \pm 0.035 \pm 0.065, \tag{7.1}$$

where the first uncertainty is statistical from B_c^+ and B^+ yields, the second is due to B_c^+ yield systematic uncertainty and the third is systematic in the acceptance ratio calculation. This result is consistent with Run-I result and its uncertainty is comparable with Run-I.

Having established a clear B_c^+ signal in J/ψ-electron combinations, we measured the B_c^+ lifetime in a larger sample of 783 J/ψ-electron events where the decay length cut was removed. An unbinned maximum likelihood fit was performed to extract the B_c^+ lifetime. Background shapes were determined from each control sample and the number of each background was estimated. Prompt background shape was assumed to be a Gaussian resolution function and the number of this background was floated in the J/ψ-electron data fitting. As a result of the J/ψ-electron data fitting, we found 237 signal events over a background level of 546±54, and extracted the B_c^+ lifetime to be

$$\tau_{B_c} = 0.474\ ^{+0.073}_{-0.066} \pm 0.033 \text{ ps}, \tag{7.2}$$

where the first uncertainty is statistical and the second one is systematic. This result is consistent with Run-I result and its uncertainty is about 40% of Run-I uncertainty.

Bibliography

[1] M. E. Peskin and D. V. Schroeder,
"An Introduction to Quantum Field Theory", (Perseus Books, 1995).

[2] C. Quigg,
"Gauge Theories of the Strong, Weak, and Electromagnetic Interactions", (Addison-Wesley, 1997).

[3] R. P. Feynman,
"Quantum Electrodynamics", (Benjamin, New York, 1962).

[4] S. Willenbrock,
"The Standard Model and the Top Quark", hep-ph/0211067.

[5] S. L. Glashow,
Nucl. Phys. **22**, 579 (1961),
S. Weinberg,
Phys. Rev. Lett. **19**, 1264 (1967),
A. Salam,
"Elementary Particle Theory: Relativistic Groups ad Analyticity" (Nobel Symposium No. 8), edited by W. Svartholm (Almqvist and Wiksell, Stockholm 1968), 367.

[6] P. W. Higgs,
Phys. Rev. Lett. **12**, 132 (1964), Phys. Rev. **145**, 1156 (1966),
G. 'tHooft,
Nucl. Phys. B **33**, 167 (1971), Nucl. Phys. B **35**, 167 (1971).

[7] M. Kobayashi and K. Maskawa,
Progr. Theor. Phys. **49**, 652 (1973).

[8] W. J. Marciano,
Nucl. Phys. Proc. Suppl. B **59**, 339 (1997).

[9] Particle Data Group, S. Eidelman et al.,
Phys. Lett. B **592**, 1 (2004).

[10] H. Fritzsch, M. Gell-Mann, and H. Leutwyler,
Phys. Lett. B **47**, 365 (1973).

[11] V. W. Hughes and T. Kinoshita,
Rev. Mod. Phys. **71**, S133 (1999).

[12] K. Wilson,
Phys. Rev. D **10**, 2445 (1974),
M. Creutz,
Quarks, Gluons, and Lattices, (Cambridge University Press, Cambridge, 1983).

[13] C. Peterson *et al.*,
Phys. Rev. D **27**, 105 (1983).

[14] G. Abbiendi *et al.*
hep-ex/0210031 submitted to Eur. Phys. J. C..

[15] M. Cacciari and P. Nason,
Phys. Rev. Lett. **89**, 12203 (2002).

[16] R. D. Field,
Phys. Rev. D **65**, 094006 (2002).

[17] D. Acosta *et al.*
Phys. Rev. D **71**, 032001 (2005).

[18] M. Cacciari, S. Frixone, M. L. Mangano, P. Nason and G. Ridolfi,
JHEP 0407:0332004.

[19] Eichten E *et al.*,
Phys. Rev. D **17**, 3090 (1979), Phys. Rev. D **21**, 203 (1980).

[20] Shifman M A, Vainshtein A I, Zakharov V I,
Nucl. Phys. B **147**, 345, 448 (1979),
Reinders L J, Rubinshtein H, Yazaki S,
Phys. Rep. **127**, 1 (1985),
Narison S,
Phys. Lett. B **198**, 104 (1987),
Dominguez C A, Paver N,
Phys. Lett. B **197**, 423 (1987), Phys. Lett. B **199**, 596 (1987).

[21] Nussinov S, Wentzel W,
Phys. Rev. D **36**, 130 (1987),

Voloshin M B, Shifman M A, Sov. J.
Nucl. Phys. **45**, 292 (1987), Nucl. Phys. **47**, 511 (1988),
Lepage G P, Thacker B A,
Nucl. Phys. B(Proc. Suppl.) **4**, 199 (1988),
Eichten E,
Nucl. Phys. B(Proc. Suppl.) **4**, 170 (1988).

[22] F. Abe *et al.*[CDF Collaboration],
Phys. Rev. Lett. **81**, 2432 (1998), Phys. Rev. D **58**, 112004 (1998).

[23] Gottfried K,
Phys. Rev. Lett. **40**, 598 (1978),
Voloshin M B,
Nucl. Phys. B **154**, 365 (1979),
Peskin M,
Nucl. Phys. B **156**, 365 (1079).

[24] Yan T-M,
Phys. Rev. D **22**, 1652 (1980),
Kuang Y-P, Yan T-M,
Phys. Rev. D **24**, 2874 (1981), Phys. Rev. D **41**, 155 (1990),
Kuang Y-P, Tuan S F, Yan T-M,
Phys. Rev. D **37**, 1210 (1988).

[25] S. Godfrey,
Phys. Rev. D **70**, 054017 (2004).

[26] D. Gromes,
Z. Phys. C **26**, 401 (1984),
D. Gromes, in *Proceedings of the Yukon Advanced Study Institute, 1984*, edited by N. Isgur, G. Karl, P. J. O'Donnell, (World Scientific, Singapore, 1985) p. 1.

[27] V. B. Berestetskij, E. M. Lifschitz, and L. P. Pitaevskij,
Relativistic Quantum Theory, (Oxford, New York, 1971) p. 280.

[28] S. Godfrey nad N. Isgur, Phys. Rev. D **32**, 189 (1985).

[29] T. Barnes, N. Black, and P. R. Page,
Phys. Rev. D **68**, 054014 (2003).

[30] E. J. Eichten and C. Quigg,
Phys. Rev. D **49**, 5845 (1994).

[31] D. Ebert, R. N. Faustov and V. O. Galkin,
Phys. Rev. D **67**, 014027 (2003).

[32] L. P. Fulcher,
Phys. Rev. D **60**, 074006 (1999).

[33] S. S. Gershtein, V. V. Kiselev, A. K. Likhoded, and A V. Tkabladze,
Phys. Rev. D **51**, 3613 (1995).

[34] S. N. Gupta and J. M. Johnson,
Phys. Rev. D **53**, 321 (1996).

[35] J. Zeng, J. W. Van Orden, and W. Roberts,
Phys. Rev. D **52**, 5229 (1995).

[36] C. T. H. Davies, K. Hornbostel, G. P. Lepage, A. J. Lidsey, J. Shigemitsu, and J. H. Sloan,
Phys. Lett. B **382**, 131 (1996).

[37] M. Neubert,
Phys. Rept. **245**, 259 (1994).

[38] G. T. Bodwin, E. Braaten, G. P. Lepage, Phys. Rev. D **51**, 1125 (1995), T. Mannel, G. A. Schuler, Z. Phys. C **67**, 159 (1995).

[39] A.Pineda and J. Soto,
Nucl. Phys. Proc. Suppl. **64**, 428 (1998),
N. Brambilla, A. Pineda, J. Soto and A. Vairo,
Phys. Rev. D **60**, 091502 (1999),
N. Brambilla, A. Pineda, J. Soto and A. Vairo,
Nucl. Phys. B **566**, 275 (2000).

[40] M. E. Luke, A. V. Manohar and I. Z. Rothstein,
Phys. Rev. D **61**, 074025 (2000),
A. V. Manohar and I. W. Stewart,
Phys. Rev. D **63**, 054004 (2001),
A. H. Hoang, A. V. MManohar and I. W. Stewart,
Phys. Rev. D **64**, 014033 (2001).

[41] A. I. Onishchenko,
hep-ph/9912424,
Ch.-H. Chang, Sh.-L. Chen, T.-F. Feng, X.-Q. Li,
Commun. Theor. Phys. **35**, 51 (2001), Phys. Rev. D **64**, 014003 (2001).

[42] V. V. Kiselev,
Mod. Phys. Lett. A **10**, 1049 (1995),
V. V. Kiselev,
Int. J. Mod. Phys. A **9**, 4987 (1994).

[43] M. Lusignoli and M. Msetti,
Z. Phys. C **51**, 549 (1991).

[44] V. V. Kiselev,
Phys. Lett. B **362**, 173 (1995).

[45] V.V.Kiselev,
"*Decays of the B_c meson*", arXiv:hep-ph/0308214, (21 Aug 2003).

[46] N. Brambilla and A. Vairo,
Phys. Rev. D **62**, 094019 (2000).

[47] M. Beneke and G. Buchalla,
Phys. Rev. D **53**, 4991 (1996).

[48] V. V. Kiselev, A. E. Kovalsky, A. K. Likhoded,
Nucl. Phys. B **585**, 353 (2000).

[49] A. El-Hady, M. Lodhi, and J. Vary,
Phys. Rev. D **59**, 094001 (1999).

[50] A. Yu. Anisimov, I. M. Narodetskii, C. Semay, and B. Silvestre-Brac,
Phys. Lett. B **452**, 129 (1999).

[51] A. Yu. Anisimov, P. Yu. Kulikov, I. M. Narodetskii, K. A. Ter-Martirosyan,
Phys. Atom. Nucl. **62**, 1739 (1999), Yad. Fiz. **62**, 1868 (1999).

[52] V. V. Kiselev,
Phys. Lett. B **372**, 326 (1996).

[53] Chao-Hsi Chang and Yu-Qi Chen,
Phys. Rev. D **46**, 3845 (1992).

[54] N. Brambilla *et al.*,
hep-ph/0412158.

[55] E. Braaten, K. Cheung and T. C. Yuan,
Phys. Rev. D **48**, 4230 (1993), Phys. Rev. D **48**, 5049 (1993),
K. Cheung,
Phys. Lett. B **472**, 408 (2000).

[56] Chao-Hsi Chang and Yu-i Chen,
Phys. Rev. D **48**, 4086 (1993),
Chao-Hsi Chang, Yu-Qi Chen, Guo-Ping Han and Hung-Tao Jiang,
Phys. Lett. B **364**, 78 (1995),
Chao-Hsi Chang, Yu-Qi Chen and R. J. Oakes,
Phys. Rev. D **54**, 4344 (1996),
K. Kolodziej, A. Leike and R. Rückl,
Phys. Lett. B **355**, 337 (1995),
A. v. Berezhnoy, V. V. Kiselev, A. K. Likhoded,
Z. Phys. A **356**, 79 (1996),
S. P. Baranov,
Phys. Rev. D **56**, 3046 (1997).

[57] Chao-Hsi Chang and Xing-Gang Wu,
Eur. Pys. J. C. **38**, 267 (2004).

[58] Chao-Hsi Chang, Jian-Xong Wang and Xing-Gang Wu,
Phys. Rev. D **70**, 114019 (2004),
Chao-Hsi Chang, Cong-Feng Qiao, Jian-Xiong Wang and Xing-Gang Wu,
Phys. Rev. D **71**, 074012 (2005).

[59] H. L. Lai, *et al.*,
hep-ph/0201195.

[60] Geoffrey T. Bodwin, Eric Braaten and G. Peter Lepage,
Erratum Phys. Rev. D **55**, 5853 (1997).

[61] Yu-Qi Chen and Yu-Ping Kuang,
Phys. Rev. D **46**, 1165 (1992),
E. Eichten, C. Quigg,
Phys. Rev D **52**, 1726 (1995).

[62] C-H Chang *et el.*,
arXiv,hep-ph/0309120 and hep-ph/0309121.

[63] G. Aubrecht et al.,
A Teachers Guide to the Nuclear Science Wall Chart,
Contemporary Physics Education Project, 2003,
`http://www.lbl.gov/abc/wallchart/teachersguide/pdf/Chap11.pdf`.

[64] C. W. Schmidt,
The Fermilab 400-MeV Linac upgrade,
FERMILAB-CONF-93-111 (1993).

[65] Fermilab Beams Division,
Run-II Handbook,
http://www-bd.fnal.gov/runII/index.html.

[66] J. Marriner,
Stochastic Cooling Overview,
FERMILAB-CONF-03-158 (2003).

[67] R. Blair et al.,
The CDF-II detector: Technical Design Report,
FERMILAB-PUB-96/390-E (1996).

[68] F. Abe et al.,
Nucl. Inst. and Meth. Phys. Res, **271**, 387 (1988),
FERMILAB-PUB-94/024-E (1994).

[69] T. K. Nelson et al.,
FERMILAB-CONF-01/357-E.

[70] A. Sill et al.,
Nucl. Instrum. Methods A **447**, 1 (2000).

[71] T. Affolder et al.,
Nucl. Instrum. Methods A **485**, 6 (2002).

[72] K. T. Pitts et al.,
FERMILAB-CONF-96-443-E.

[73] http://penn01.fnal.gov/~cot/

[74] R. Brun, K. Hakelberg, M. Hansroul, and J.C. Lasalle,
CERN-DD-78-2,
CERN-DD-78-2-REV.

[75] A. Korn,
Measurement of the B Hadron Masses in Exclusive J/ψ Decay Channels,
CDF Public Note 6963.

[76] D. Acosta et al. [CDF Collaboration],
A Time-of-Flight detector in CDF-II,
Nucl. Instrum. Methods A **518**, 605 (2004).

[77] http://huhepl.harvard.edu/~cmx/cdfnotes/

[78] E. J. Thomson et al.,
IEEE Trans. Nucl. Sci. **49**, 1063 (2002).

[79] `http://web.hep.uiuc.edu/Engin/CDF/XTRP/`

[80] W. Ashmanskas et al.,
FERMILAB-CONF-02/035-E;
A. Bardi et al.,
Nucl. Instrum. Methods Phys. Res. A **485**, 6 (2002).

[81] D. Acosta et al.,
Nucl. Instrum. Methods A **494**, 57 (2002).

[82] "http://www-cdf.fnal.gov/internal/physics/bottom/bpak/" under "B Analysis Basics".

[83] J. Marriner,
CDF internal note /CDF/DOC/SEC_VTX/PUBLIC/1996.

[84] T. Moulik *et el.*,
CDF internal note /CDF/ANAL/BOTTOM/CDFR/6793.

[85] C. Campagnari *et el.*,
CDF internal note /CDF/ANAL/TOP/CDFR/2161.

[86] S. Eidelman *et al.*,
Physics Letters B592, 1 (2004)

[87] T. Sjostrand and M. Bengtsson,
Comput. Phys. Comm. **43**, 367 (1987).

[88] K. Lannon *et al.*,
CDF Note 7253 (PRD paper)

[89] R. Field,
CDF/ANAL/BOTTOM/PUBLIC/5813, UFIFT-HEP-01-25.

[90] K. Lannon and K. Pitts,
CDF internal note CDF/PHYS/BOTTOM/CDFR/6253.

[91] S. D'Auria *et el.*,
CDF internal note /CDF/ANAL/BOTTOM/CDFR/7018.

[92] CDF B_s working group,
CDF internal note CDF/PHYS/BOTTOM/CDFR/7500.

[93] p_T spectra for different B_c mass assumption and different process $gg \to B_c$, $gg \to B_c^*$ and $q\bar{q} \to B_c$ were provided by Vaia Papadimitriou.

[94] S. D'Auria *et el.*,
CDF internal note CDF/PHYS/BOTTOM/CDFR/6391.

[95] D. Amidei *et el.*,
CDF internal note CDF/DOC/ELECTROWEAK/CDFR/6681,
M. Coca *et el.*,
CDF internal note CDF/DOC/ELECTROWEAK/CDFR/6300.

[96] D.Glenzinski *et el.*,
CDF internal note CDF/DOC/BOTTOM/CDFR/7314.

[97] Giovanni Punzi,
"Comments on Likelihood fits with variable resolution", in proceeding of PhyStat2003 conference, physics/0401045.